NASA Technical Memorandum 100657

THE PROS AND CONS OF CODE VALIDATION

Percy J. Bobbitt

July 1988

National Aeronautics and
Space Administration

Langley Research Center
Hampton, Virginia 23665-5225

THE PROS AND CONS OF CODE VALIDATION

Percy J. Bobbitt
NASA Langley Research Center
Hampton, Virginia

ABSTRACT

The correlation of theory with experimental data has been going on as long as we have had theoretical methods and experimental facilities. Up until the 1970's the primary objective of this activity in the aeronautical sciences was to determine if the theoretical methods were valid. Approximations and assumptions made to reduce the governing equations and boundary conditions to a solvable form insured that the experimental results would be more accurate. Today, however, with our ability to solve the most complicated, nonlinear fluid-flow equations with high precision, the accuracy of computed results may, in some situations, exceed that obtained in the wind tunnel. Consequently, to determine which of the two results are the most reliable one must assess in detail the cumulative result of the various error sources in each. The purpose of the present paper is to examine a number of these error sources and quantify them with the aid of specific calculations or experimental data. In many cases suggestions and examples will be given to indicate how the error source can be minimized.

INTRODUCTION

There is a somewhat apocryphal law of research which states that, "Nobody believes analytical results except the man who programmed it. Everybody believes wind tunnel results except the man who tested it." If there is any truth in this statement it is that more researchers are apt to take experimental data at face value than computational results. This attitude, I think, is partly inherited from a past where most measurements were steady state and linear methods were state-of-the-art. Experimental data, in most situations, was clearly more accurate than theroretical results.

In today's climate, where computational techniques have been successfully applied to the most complicated governing equations and aircraft geometries, there is no reason to expect experimental data to be more accurate than theoretical calculations without a detailed examination of both results. There are approximately 10 error sources in wind tunnel testing that come to mind that in any given test can lead to inaccuracies that are larger than the suspected error in a "highly accurate" analytical result. Of course analytical results have their own error sources. Indeed one can readily identify 10 or 12 of them, although all will not be present in a single calculation. Therefore we are in a situation where, in an ever increasing number of cases, when the experimental and analytical data do not agree, we cannot be sure which is the most accurate. Instead of "validating a code" we are comparing or correlating the results from a code application with experimental data and both may receive some validation. Nevertheless, the value of theory/experiment comparisons is undiminished. As the two types of data become more competitive, one would expect that more attention will be paid to the various error sources so that they will be evaluated more frequently and/or reduced.

The purpose of the present paper will be to identify and discuss some of the major error sources or "cons" in computational and experimental results. It will also be evident from the discussion that the recognition and treatment of error sources is one of the most important "pros" of code validation. Where possible the error sources will be quantified with the aid of other calculations or experimental data. In some cases it is only possible to demonstratate a problem. Some of the error sources are well known and commonly assessed, or accounted for, while others are more obscure or of recent origin and the evaluation of their effects is still underway.

In the ensuing discussion wind tunnel error sources will be discussed first followed by those found in computational work. Finally, some summary observations will be made.

NOMENCLATURE

A	amplitude of boundary layer disturbance
AR	aspect ratio
A_o	amplitude of boundary layer disturbance at netural stability
B	wing span
BP	back pressure ratio = p_b/p_∞
C_{D_o}	minimum drag coefficient
C_d	section drag coefficient
C_L	lift coefficient
C_N	normal force coefficient
C_ℓ	rolling moment coefficient
C_m	pitching moment
C_n	section normal force coefficient
C_{n_r}	yawing moment coefficient
C_p	pressure coefficient
C_p^*	sonic pressure coefficient

c	airfoil chord
c_R	root chord
c_f	skin friction coefficient
c_ℓ	section lift coefficient
$\bar{c}$	mean aerodynamic chord
d	diameter of body
E	mean voltage across hot film
e	fluctuating voltage
f	frequency
h	height of airfoil test section
i_t	tail incidence angle
k	reduced frequency, $\frac{\omega c}{U_\infty}$
k_a	admissible roughness
L	length of cone or equal to 1 foot in nondimensional time parameter $t\ U_\infty/L$
M	Mach number
M_T	test section Mach number determined by tunnel instrumentation
m	mass flow
n	logarithmic exponent of T-S wave growth rates, $n = \ln (A/A_0)$
p	pressure
p_b	downstream static pressure
q_∞	free-stream dynamic pressure
Re	Reynolds number per foot, 1/ft
Re_c	Reynolds number based on chord
$Re_{\bar{c}}$	Reynolds number based on mean aerodynamic chord
Re_{c_R}	Reynolds number based on the wing root chord
Re_T	Reynolds number at the end of transition
Re_t	Reynolds number at the beginning of transition
Re_{δ^*}	Reynolds number based on δ^*
Re_θ	Reynolds number based on momentum thickness
SiO_2	Silicon Dioxide
S_{T_t}	$(\frac{\partial \log E}{\partial \log T_t})_{u,\ \rho,\ T_w}$ or $(\frac{\partial \log E}{\partial \log T_t})_{m,\ T_w}$
S_u	$(\frac{\partial \log E}{\partial \log u})_{\rho,\ T_t,\ T_w}$
S_ρ	$(\frac{\partial \log E}{\partial \log \rho})_{u,\ T_t,\ T_w}$
s	local span
T	mean temperature
T_∞	free stream static temperature
t	time
U_∞	free stream velocity
u	velocity in flow direction
v	velocity in vertical direction
w	velocity in horizontal direction
x	chordwise distance from leading edge of airfoil
x_T	location of the end of transition
x_t	location of the beginning of transition
y	distance along spanwise direction
z	distance normal to wing surface
α	angle of attack, degrees
α_T	angle of attack determined by tunnel instrumentation
α_0	angle of attack at $t = 0$
α_1	amplitude of angle of attack oscillation
β	sideslip angle, degrees
γ	ratio of specific heats
δ^*	boundary layer displacement thickness
$\zeta = \frac{2y}{B}$	
θ	angle measured from cone surface, degrees
θ_c	cone semi angle, degrees
ρ	density
ω	frequency

Abbreviations:

Å	angstrom (10^{-10} meters)
FDS	Flux difference splitting

FVS	Free vortex sheet or flux vector splitting
Hz	Hertz, cycles/sec
LDV	Laser doppler velocimeter
LTPT	Low-Turbulence Pressure Tunnel
NLF	natural laminar flow
NTF	National Transonic Facility
°R	degrees Rankine
TCT	Transonic Cryogenic Tunnel
T-S	Tollmien-Schlichting
WIAC	Wall Interference Assessment and Correction

Superscripts:

~	root-mean square value
-	mean value
'	instantaneous value

Subscripts:

corr	corrected
max	maximum value
ref	reference
t	total condition
tr	value at transition
w	wall
∞	free stream conditions

VALIDATED CODES

In this paper the word validation is used in its broadest sence. A substantial comparison of a series of theoretical calculations with data from a number of experimental investigations for a broad range of conditions that results in good agreement is said to yield a validated code. There is the added requirement, however, that both experimental and computational errors be assessed or reduced in each situation to the lowest possible level. No single comparison can yield a validated code. Just as a new aircraft has to prove itself at all points of its operational envelop, a computer code must prove accurate for the full range of physical parameters and free-stream conditions consistent with its math model and geometry package. For example, a computer code may yield good correlations at low Reynolds numbers and low Mach numbers but fail at high Mach numbers and/or Reynolds numbers. Good agreement may be obtained for a wing of high aspect ratio and only fair agreement for one of low aspect ratio. Each succeeding application of a code and favorable comparison with more accurate experimental data will expand the validation space of that code.

A single tunnel or a single model will usually not be sufficient to validate a code. For some codes both surface and flow field measurements are required and a variety of quantities must be measured in each region. Those codes that apply to both the subsonic and supersonic speed regiemes must be checked in both places. Calculations that include the viscous terms or a boundary-layer/inviscid-flow interaction require measurements such as boundary layer profiles, transition, separation, and reattachment and perhaps Reynolds stresses. Separated flows are generally unsteady and some means of measuring that unsteadiness is required.

The validation process just described is depicted in figure 1. The key point that this sketch highlights is that there are many questions one must ask himself after receiving a "not adequate" verdict from a correlation. It should be noted in this connection that one does not expect the same accuracy from a linear-equation code with a strip boundary-layer as from one which solves the Navier-Stokes equations. Since the aircraft designer requires a hiearchy of codes then there must be a sliding scale for measuring satisfactory correlations. Clearly, much more stringent criteria should be applied to the codes based on higher-order-equation sets than to those based on the potential equations.

If one has a CFD code that has just been formulated, and he desires to validate it, he must first make sure, for the solution algorithm and grid scheme chosen, that there are not other avoidable or reducable errors in the computation. A list of possible error sources that can exist in a computational result is given in figure 2, including those that can come from the solution algorithm itself and the grid scheme.

Simlarly when the wind tunnel and model are chosen for an experiment care should be taken to assess the error sources and eliminate, or correct, them where possible. Figure 3 gives a list of a number of potential wind-tunnel error sources. Many of these error sources can not be avoided; however, some like wall-interference and aeroelasticity effects can be evaluated and/or corrected and others can be minimized.

In the subsequent sections a discussion will be given of most of the computational and wind tunnel error sources listed in figures 2 and 3, respectively, starting with the latter.

WIND TUNNEL ERROR SOURCES

Since the invention of the wind tunnel researchers using them have had to contend with a variety of error sources. Ten are listed in figure 3. Work to reduce or eliminate these adverse effects probably started with the second wind tunnel and continues until today. Most of the effort has been concentrated on the first

four since they were perceived to have the most impact on data accuracy. Nevertheless, significant progress has been made in the "treatment" of all ten. In subsequent sections a discussion will be given of each item including, in most cases, specific examples of the error sources and, in some instances, means to reduce or eliminate it.

Wind Tunnel Wall Interference

The use of wind tunnels to obtain aerodynamic data on aircraft and aircraft components dates back to 1871 when Frank H. Wenham carried out his first experiments. In Wenham's words[1], it "had a trunk 12-feet long and 18-inches square, to direct the current horizontally, and in parallel course." Since then we have had a variety of wind-tunnel concepts including open-throat test sections with closed returns, closed-test sections with open returns, and closed-test section with closed returns. Through the years it became clear that neither the open or closed throat test sections provided data equivalent to a "free-air" result but that something in between was required. In the late forties and early fifties slotted and perforated test sections were invented and for the first time data was obtained at high subsonic speeds that was near that of free-air. Correction methodology based on linear theory was developed to correct the residual error. These methods relied on ideal, homogenous slotted- and perforated-wall boundary conditions which, in turn, depended on an effective orifice coefficient. A number of analytical and parametric-experimental studies have produced values for the effective orifice coefficient.

In 1976 Kemp[2] devised an entirely new approach to 2-D wall corrections that utilized wall and model pressures to assess whether a particular data point was correctable and provided the free-stream Mach number and angle of attack that would yield the best approximation to the measured pressures (see figure 4). In the original formulation measured pressures were used in a highly accurate airfoil design code to determine the equivalent inviscid shape and the free-air Mach number and alpha that match the measured airfoil and wall pressures. This technique has become known as the wind tunnel interference assessment and correction or WIAC procedure.

WIAC procedures were first applied to two-dimensional airfoil tests.[3-12] Noteworthy here is the work of Newman and Gumbert[7-10] utilizing data obtained in the slotted wall test section of the Langley 0.3-M TCT and the Grumfoil airfoil code. The method also accounts for the effects of the side wall boundary layer using the analyses of Barnwell, Barnwell-Sewall, or Murthy.[5,6,10,11]

An illustration of the effectiveness of WIAC procedures is given in figures 5 and 6 which give variations of corrected and uncorrected lift and drag with angle of attack on a NACA 0012 airfoil. Also shown is a free-air Navier Stokes calculation which serves as a target since it is clearly more accurate than the uncorrected experimental data. Data from both slotted-wall and adaptive wall test sections in the 0.3-M TCT are plotted. As expected the adaptive wall test section provided data that is near interference free and only small differences from the free-air curve are evident (see figures 5 and 6). When the WIAC alpha and Mach corrections are applied both sets of data collapse on each other and agree very well with the free-air Navier Stokes curves.

Three-dimensional linear and nonlinear WIAC codes have been developed[13-16] and applied to calculate the corrections attendent to a transport model test in the NTF.[17,18] These codes utilize nine rows of pressure taps on the tunnel wall as a boundary condition as depicted in figure 7. The location of the rows is shown in the sketch on the left; pressue distribution along three of the rows is plotted on the right for the Pathfinder I transport model at an uncorrected Mach number of 0.8 and angle of attack of 2.2 degrees. The linear code has a highly sophisticated math model of the walls, slats, model, sting, and re-entry flap region. A detailed discussion of this method is given in references 17 and 18. Preliminary results for the Pathfinder I transport model in the NTF are given in these references; an example of the wall induced Mach number corrections is given in figure 8 for a tunnel Mach number of 0.8 and C_L = 0.514. In the vicinity of the model the Mach correction varies from -0.001 to -0.0002; the angle of attack corrections are on the order of 0.1 degrees or less. At higher Mach numbers and lift coefficients the corrections will be larger.

An example of wall corrections determined from the nonlinear WIAC code TUNCOR[13-16,18] is given in figure 9. Corrected and uncorrected C_L results for the Pathfinder I transport model for two uncorrected Mach numbers are plotted. The difference between the corrected and uncorrected points are the α corrections which are on the order of a tenth of a degree.

Some idea of the effect of ΔM and $\Delta\alpha$ corrections, with magnitudes similar to those seen at transonic speeds, can be obtained from figure 10.[19] Plotted in this figure are pressure distributions at two spanwise locations for two free-stream conditions. The angle of attack and Mach number is 0.054 degrees and 0.0013, respectively, higher in one case than the other. The differences in the pressure distributions are clearly not trivial.

Over the years pressure data similar to that of figure 10 have been used without any corrections to the measured free-stream conditions. Differences between the calculated and experimental pressures have been attributed solely to deficiencies in the theory. There have also been cases of near perfect agreement between theory and experiment where, had the experimental data been corrected, the agreement would have been less spectacular.

Another type of wind tunnel test where experimentalists frequently fail to correct for wall interference effects is that at high angles of attack and subsonic speeds. Indeed there are many reports with delta and modified-delta wing data where wall effects are never discussed. When corrections are applied they are usually based on a math model which bears little resemblance to the real flow.

A program was recently undertaken at the Langley Research Center to fully explore the pressure distribution and flow field of a 65-degree delta wing at subsonic and transonic speeds. A number of leading edges with different leading edge radii are available to investigate their effect. These models will be tested in the NASA Langley Low Turbulence Pressure Tunnel (LTPT), Basic Aerodynamic Research Tunnel (BART), and the National Transonic Facility (NTF). Since the comparison of these data with the best potential, Euler and Navier Stokes codes is one of the most important objectives of this program, it is important to reduce experimental error to a minimum. With this in mind the Langley/Boeing Leading Edge Vortex (LEV) Program was modified to determine the magnitude of the wall interference effects.[20] A sample result from this activity is shown in figure 11 along with the panel model of the LTPT Tunnel, wing and attached leading-edge vortices. Plotted in the figure are the core circulations and vortex-sheet shapes for both free-air and wind-tunnel-wall boundary conditions for 15- and 30-degrees angle of attack. The alpha corrections in this figure have been applied to the free-air data for comparison of the corrected result with the wind-tunnel calculation. They could also have been used to correct the wind-tunnel data to obtain a free-air result. At 15-degrees angle of attack the correction is ~ 0.8 degrees and at 30-degrees angle of attack it is ~ 2.0 degrees. It is clear that when the free-air data is corrected, it is in near perfect agreement with calculation that includes the wind-tunnel walls.

The lesson to be learned from the wall-interference effects illustrated in this section is that anytime the objective of a wind-tunnel test is to validate a code then a wall intereference assessment must be made.

Sting Effects

Except for tunnels which are equipped with a magnetic suspension system, some type of sting is necessary to hold an aircraft model in a fixed position in the test section. Stings attached to the bottom of the fuselage of a model are generally referred to as "blades". Stings are also attached to the top of the fuselage, the tip of the vertical tail, and the tips of the wing. The most common attachment area is in the rear of the fuselage. In all cases the flow over the model in the vicinity of the attachment is distorted, resulting in a change in the surface pressure and an error in the measured forces and moments. Frequently the geometry of the model itself has to be distorted to accommodate the sting, resulting in an additional anomaly in the measurement.

Figure 12 from reference 21 depicts some of the problems and errors that can result from a rear-fuselage-mounted sting. The sketch and plot in the upper left shows the consequences of a fuselage-geometry modification required to accommodate the sting and balance system. An error in C_{D_0} at low supersonic speeds of 18 percent is incurred for the single jet model and there were sizable errors in pitching moment as well. A slightly different sting installation is shown in the upper right sketch but the effects are the same. Flow distortion at the rear of the model causes a significant change in the tail incidence angle required to trim the model. Errors in drag and moment are also incurred.

The sketch at the bottom of figure 12 shows how the aft fuselage modifications and sting affect the dynamic yawing moment coefficient, C_{n_r}. Similar effects might be expected on the dynamic pitching moment coefficient C_{m_q}. Generally the moment coefficients, both static and dynamic, are the most affected by rear mounted stings due to the fact that even small pressure changes in that area are magnified by the long moment arm.

Another slant on the errors due to the sting installation can be obtained by the sketches and data on figure 13. Tests of a 70-degree arrow wing model were carried out in several low speed wind tunnels over ranges of angle of attack and sideslip.[22] As seen in figure 13(a) each test has a different sting or sting/strut arrangement. The effect of these arrangements and, perhaps, the test-section geometries have on the lift and rolling moment coefficients as a function of sideslip is seen in figure 13(b). The angle of attack is fixed at 35 degrees where the upper surface flow and wake are dominated by leading edge vortices. With this in mind one would expect the full-scale tunnel and arrangement A to yield the most accurate data. Only the full-scale tunnel curve has the asymmetric characteristics close to that expected. None of the tests provide a zero rolling moment at $\beta = 0$ indicating that there must be a small asymmetry in the model geometry or surface finish and/or the onset tunnel flow. The former is the most likely since not all the tunnels are likely to have the same flow characteristics. The variation of lift coefficient with sideslip angle is similar for all four tunnels. Given the data scatter in figure 13(b) it would not be difficult to convince someone that a reasonably accurate CFD code would yield a more accurate result.

Models tested at high angles of attack may be supported in a number of ways.[23] Two are depicted in figure 14 along with the associated C_N vs α curves. The two support systems give approximately the same C_N values at $\alpha = 65^0$ for the missile-body model but they quickly diverge so that at 85 degrees the sting supported model gives a 50 percent higher C_N than the strut supported one. Near 90° angle of attack, where

the flow is nearly two dimensional, one would expect the sting supported model data to be the more accurate. This is a situation where a test in a magnetic suspension tunnel would be invaluable.

The examples of sting effects just presented shows that a real problem exists for those who would compare theoretical calculations with data from a sting supported model. This is particularly true if those predictions involve the region of sting attachment or high angles of attack. The need to include the sting in the math model where comparisons with sting mounted models are contemplated is clear. We have seen in the previous section that there are many situations where the tunnel walls should be modeled as well.

Reynolds Number Effects

Efforts to match flight Reynolds numbers in ground facilities are well known to most. Up until the early 80's two approaches dominated high Reynolds number wind tunnel design. One utilized pressure to increase density and thus Reynolds number, and the other was simply to build large wind tunnels and test very large models - sometimes actual aircraft. An example of the former is the Variable Density Tunnel (VDT) designed by Max Munk (see figure 15). It could be pressurized to 20 atmospheres and model spans on the order of 2 feet could be accommodated. At the time this tunnel was constructed a 2-foot span model was roughly 1/20 scale; therefore, when tests were carried out at 20 atmospheres pressure, full-scale results were obtained. The VDT still exists but is no longer operative; it has been declared a National Historical Landmark.

Another, and more recent, example of a pressure tunnel is the Langley Low-Turbulence Pressure Tunnel (LTPT) which not only can be pressurized to obtain high Reynolds numbers (see figure 16) but can be "pumped down" to obtain low Reynolds numbers. It was first placed in operation in 1941. The Ames 12-Foot Pressure Tunnel (PT), though larger than the LTPT, was built with the same circuit design and flow treatment and commenced operation in 1946. The LTPT can be pressurized to 10 atmospheres and the Ames 12-Ft. PT to 6. Both tunnels have been valuable in investigating the aerodynamic characteristics of high-lift systems. The LTPT has a special balance yoke, depicted in figure 16, and wall treatment that permits high-lift tests while maintaining two dimensional flow. Because of the large size of the Ames 12-Ft. PT, three dimensional high-lift tests are possible.

An example of how Reynolds number can effect the aerodynamic characteristics of high-lift systems is given in figure 17. Shown here is the lift coefficient versus angle of attack for a four-element system for Reynolds numbers of 2.8×10^6 and 20.9×10^6. The expected increase in maximum lift is obtained but the loss in lift at lower C_l is unexpected. Wind tunnels that can only operate at Reynolds numbers of 5 or 6 million normally use Reynolds number scaling to obtain a result for higher Reynolds number. This procedure works reasonably well at cruise C_l's and attached flow conditions but fail at conditions where high-lift systems operate.

A fact often overlooked is that airfoils and high-lift systems at high lift not only are sensitive to Reynolds number but to Mach number as well. Even at low speeds compressibility effects are present and distinct from Reynolds number effects. Mach number increases cannot be used as a substitute for an increase in Reynolds when measurements near $C_{l_{max}}$ are being made. This incorrect procedure is one frequently used by researchers with low-speed atmospheric wind tunnels and, consequently, no capability to vary Reynolds number separately from Mach number. Figure 18(a) showing the variations of $C_{l_{max}}$ with Mach number for a range of Reynolds numbers for a NASA 0012 clearly indicates that an increase in Mach number has the opposite effect to an increase in Reynolds number. The same data is plotted in figure 18(b) to show how $C_{l_{max}}$ varies with Reynolds number for various Mach numbers.

The development of cryogenic wind tunnels over the past decade has provided a new empetus to high Reynolds number testing. At Langley there are two cryogenic facilities, the 0.3-m TCT and the NTF. The test envelop of the latter compared to other wind tunnels is shown in figure 19. Roughly a factor of 5 increase in Reynolds number is provided by nitrogen at cryogenic temperatures over air at ambient temperature.[24] Even more significant is the fact that the factor of 5 is achieved with no increase in load. This enables the minimization of unwanted aeroelastic effects and of the size of the sting for a given Reynolds number.

An example of the application of NTF's Reynolds number capability is given in figure 20.[19] Typical pressure distributions for a transport aircraft at Reynolds numbers of 5, 30, and 40 million and with free transition are plotted. A fixed transition curve for $Re_{\bar{c}} = 5 \times 10^6$ is also given for the comparison with the $Re_{\bar{c}}$ 5 x 10^6 free transition curve. It is clear

that there is a very large difference between the fixed and free transition curve for a Reynolds number of 5.0×10^6. One would hope that the fixed transition result would approximate the 30 or 40 million curves but it does not. It illustrates the error potential of fixing transition at low Reynolds numbers to approximate a high Reynolds number result. The free transition results have the correct behavior as Reynolds number is increased but the absolute values may still contain some error due to the unknown effects of the unit Reynolds number, surface finish, or flow quality on transition.

The NTF can be operated as a conventional air pressure wind tunnel and (like other pressure tunnels) its maximum Reynolds number capability is at a Mach number lower than the maximum obtainable due to power limitations. Figure 21 shows the NTF air-mode opearting envelope and indicates that the maximum Reynolds number is obtained at approximately M = 0.4. A constant q_∞ line is plotted on the figure to indicate that a model designed for that dynamic pressure can be tested at unit Reynolds number of up to 8.8×10^6 depending on the Mach number.

An air test of the Navy EA-6B aircraft with a variety of wing and tail modifications was carried out in the NTF in 1986. One of the purposes of this test was to evaluate various leading and trailing-edge modifications aimed at increasing the maximum lift coefficient of the aircraft.[25] Figure 22 shows the results of one of the tests at a Mach number of 0.3 and at two Reynolds number, 1.4×10^6 and 5.4×10^6. At a Reynolds number of 1.4×10^6 the modification to the flap gave the desired increase in C_L but the slat modification showed no effect. However, at $Re_{\bar{c}} = 5.4 \times 10^6$ the slat modification provided a significant increase in C_L in the 16 to 20 degree alpha range. It is also important to note the large increase in the $C_{L_{max}}$ levels in going from $Re_{\bar{c}} = 1.4 \times 10^6$ to $Re_{\bar{c}} = 5.4 \times 10^6$.

The major concern with Reynolds number is its effect on drag, especially at cruise Mach numbers. While most CFD practicioners continue to look primarily at pressure distributions, lift and, sometimes, moment, a quantity of equal concern to the aircraft designer is drag. Experimental researchers often shy away from making definitive drag measurements because the process of determining the tares is time consuming and sometimes imprecise. As more code validation research is carried out both theoreticians and experimentalists will have to pay more attention to drag.

A number of examples of the effect of Reynolds number on drag could be chosen; the result presented here is from the Advanced Transonic Airfoil Technology or ATAT Program carried out at Langley in the late 70's and early 80's.[26] Drag coefficient versus Mach number for three airfoils tested in that program are plotted in figure 23. In each case results are shown for three Reynolds numbers, one in the 6 to 7 million range which is typical of atmospheric wind-tunnel capabilities. As expected, there are significant differences in the drag levels for various Reynolds numbers as well as in the character of the curves at drag rise. There also appears to be more drag creep for the two supercritical airfoils than for the NACA 0012 but then they have a higher drag-rise Mach number.

The few examples that we have shown of Reynolds number effects are just the "tip of the iceberg." There is only a small percentage of our wind tunnel research and development carried out at flight Reynolds numbers. Tests at low to moderate Reynolds numbers are generally done with the full understanding of the limitations and some confidence that the trends or relative results can be extrapolated to flight values. Most of the work done at both low Reynolds number and Mach number has limited practical value and, worse still, the deficiencies relative to flight levels are often ignored or rationalized.

Flow Quality and Transition

Flow quality in wind tunnels has been a long-time concern and a number of tunnels with outstanding flow quality have been constructed over the years. Most have been low-speed special purpose facilities. Within NASA there are a number of small atmospheric facilities with good flow quality; and only a few large ones. The Langley LTPT and the Ames 12-Ft. PT discussed earlier are both equipped with a large number of screens and, at low speeds, have very low values of $\tilde{u}$. Figure 24 shows the variation of $\tilde{u}/U_\infty$ with Re/ft for a range of Mach numbers in the LTPT.[27] At an Re/ft of 10^6, $\tilde{u}/U_\infty$ values range from 0.025 to 0.06 percent. Similar levels are found in the Ames 12-Ft. PT at low speed.

A comparison of the flow quality in a large number of wind tunnels and a comparison of wind tunnel flow quality to that of the flight environment has been undertaken by Dougherty[28] and Dougherty and Fisher.[29] The measurements used to make the comparison are flucuating pressure and the start and end of transition. They were obtained on the surface of a 5° semiangle cone whose features can be seen in figure 25. It is 3-feet long and equipped with 5 thin-film and 3 unsteady pressure gages for detection of transition and free-stream pressure

disturbances, respectively. Figure 26 shows a photograph of the 5° cone mounted on the nose of a F-15 aircraft. Also seen in the photograph is the translating surface probe used for a redundant transition measurement.

A plot of the RMS pressures measured on the cone installed in a number of wind tunnels and on the F-15 up to a Mach number of approximately 1.8 is given in figure 27(a). The large differences between the flight and wind tunnel data is clear. Only at Mach numbers of 1.6 and 1.8 do the wind tunnel measurements approach those of flight. A prediction due to Lawson[30] of test-section wall pressures is also plotted; only fair agreement with measurements is achieved. This same data plotted to an expanded Mach number scale is given in figure 27(b). Also plotted are additional points from measurements made in the 8-Ft. TPT with the slots closed and with choke plates installed.[31] Both are effective at reducing the noise levels in the tunnel but the choke is much more effective than the slot covers. Indeed, the choke-plate data point at a Mach number of 0.8 is on the boundary of data obtained in flight.

Transition data corresponding to the pressure data of figure 27 is plotted in figures 28 and 29. Figure 28 shows how the start and end of transition vary with Mach number for a unit Reynolds number of approximately 3×10^6. Again wind tunnel and flight data are shown. It is evident that once the wind tunnel test sections choke ($M_\infty \approx 0.9$) and diffuser noise no longer propogates upstream, that the start and end of transition measured in the wind tunnel agree fairly well with flight data. As tunnel Mach number increases beyond 1.4 transition moves forward indicating a drop in flow quality. At a Mach number around 0.8 there is a large difference in wind tunnel and flight transition due to the differences in the wind tunnel and flight environments.

A plot of the Reynolds number at the start of transition (see figure 29(a)) shows a slightly different behavior from the transition-location data in figure 28 in that the flight values at low supersonic speeds are substantially higher than wind tunnel values. In this comparison the LRC 16-Ft TDT and the ARC 9 x 7-Foot SWT "show-up" the best. Only at low subsonic Mach numbers do flight and wind tunnel data agree.

The end of transition data plotted in figure 29(b) shows that the data from a number of wind tunnels agree quite well with flight. This would indicate that the tunnel environment has the effect of causing transition to start earlier than in flight but the completion of the process is much less affected. Beyond a Mach number of 1.4 wind tunnel and flight data diverge rapidly.

The large differences in tunnel environment and their effect on transition indicate a significant problem with data accuracy. The start and end of transition on a wind-tunel model will be different than in flight at the same unit and local Reynolds numbers due to the inferior flow quality. This in turn means the aerodynamics coefficients will be different, particularly drag. Transition fixing may help but not cure the problem. It is often assumed that transition will occur near the leading edge of a wing at high Reynolds numbers and a transition strip put in the location which will yield the correct answer. Unfortunately the boundary layer growth nor the profiles are matched and large errors still can occur. Putting the transition strip at a location so that the boundary layer thickness at the trailing edge is matched to that expected at the flight Reynolds number[32] has been found to be effective, at transonic speeds, in providing better lift and moment coefficients but drag is only marginally improved.

Wind tunnel testing of models with free transition also has problems. The first is determining where the start and finish of transition is located. If this is done then one must determine what are the corresponding flight conditions. For this one must rely on stability theory and measured or calculated pressures.

The need for improved flow quality in our wind tunnels has received increased attention over the past decade. A number of tunnels such as the 8-Ft TPT and 14- by 22-Foot Subsonic Tunnel at Langley have been modified with flow-treatments that provide an order of magnitude improvement in the levels of the fluctuating velocities and pressure in the test section. New facilities as well as other innovative concepts are being proposed to take advantage of the technology to provide a still higher level of flow quality.

At supersonic speeds a low noise throat and nozzle concept has been proven, in a pilot facility, to yield disturbance levels comparable to those in flight.[33,34]. The facility utilizes a bleed ahead of the throat (see figure 30) to "initialize" a laminar boundary layer going into the throat. A highly polished nozzle surface downstream of the throat allows the laminar flow to persist far enough that a significant quiet flow region is maintained in the center of the nozzle for model tests. Once the flow becomes turbulent on the wall then the radiated noise along Mach lines causes the flow in the center of the nozzle to become turbulent as well. Wind tunnel and flight data for start-of-transition Reynolds numbers on sharp cones are plotted figure 31 to show the capabilities of the

facility. Dramatic increases in Re_t are observed using the quiet tunnel relative to those obtained in conventional tunnels.

It has been demonstrated that good flow quality is indispensable to getting the start and end of transition to agree with flight. Consequently, experiments with models that should have long runs of laminar flow are particularly susceptable to the adverse effects of the test section environment. Both vorticity and noise can contribute to a premature transition. But it is not just the presence of vorticity and noise, it is vorticity and noise in the frequency range that the boundary layer disturbances are sensitive to. Most tunnel noise and vorticity is broad band except for peaks that stem from the fans of the drive system and unsteady separation in the high speed diffuser or off the inside corners. Increased power and test section velocities will generally raise the vorticity and noise levels across the frequency range. The increase in sound pressure level generated by the drive system when the tunnel pressure level is raised will usually have an adverse effect on transition. This effect has frequently, in the past, been erroneously identified as a unit Reynolds number effect.

Instrumentation

The types of instrumentation that we depend on to make the measurements used in the validation of computer codes are listed in figure 32. Some are used to determine the free-stream conditions, some the geometry of the model under load, and others the state variables on the model surface or in the flow field. There are a few that sense the shear or heat transfer at the model surface and provide skin friction, transition, and flow separation data. Most are used to make single point steady state measurements, a few are capable of single point dynamic measurements. Most of the advances in recent years have come in the latter category.

Figure 33 depicts the evolution of instrumentation of the past 3 or 4 decades showing the trend toward multisensor arrays and probes as well as more nonintrusive instrumentation. It also shows the progression from scanivalves to ESP units, from single wire to multiwire anemometers, from single hot-film sensors to multi-hot-film sensors and from one and two component laser velocimeters to three component LDV's and 3-D laser holography systems. The capability to "probe" in real time large areas of the surface of models and the surrounding flow fields has given "new life" to those who would like to see more activity in the validation of CFD codes. New and improved instrumentation allows us to measure things that have, heretofore, been unmeasurable or to measure them with greater accuracy. New instruments lead to new discoveries.[35]

Just as there are many types of measurements that one can make there is also a full spectrum of requirements. A few are listed on the left of figure 33. Requirements always exceed capability so as soon as a new or improved instrument appears it is immediately put to good use. Currently there is a pressing need to measure the time varying velocities and state variables on a line, in a plane, or in a volume. With one or more of these types of measurements we can start to validate Navier-Stokes predictions of time-varying flows in a meaningful way. In evaluating unsteady, separated-flow calculations today, more confidence can usually be obtained from a good flow visualization experiment than from single-point, flow-field measurements. The three-dimensional laser holovelocimeter developed by Weinstein and reported in references 36 and 37 is an attempt to overcome this deficiency. Laser induced fluoresence is another technique which may help in obtaining better unsteady measurements.

All of the instruments listed on figure 32 provide measurements that are slightly in error. Some of the errors are small, even negligible, others are large enough that they must be considered when comparison with calculations are made. In the next few sections a discussion will be given of the errors and/or limitations associated with the first six.

Strain Gage Balances

Strain gage balances are the primary instruments for measuring forces and moments on aircraft models and aircraft-component models. There are several designs available but their accuracies are comparable. The force balance designs used at the NASA Langley Reserch Center are gaged with transducer-quality modulus-compensated strain gages and temperature compensated to operate in the temperature range 60 to 180 degrees farenheit (except in the NTF). The zero shift in this temperature range is compensated to be within +/-0.5 percent of full scale output while the sensitivity shift is approximately -0.1 percent. The calibration of the force balance include loading each of the six components about the three orthogonal axes in combinations of one, two, and in some cases three axes at a time so the sensitivity and the first and second order interactions can be determined. This calibration sequence includes 81 loading combinations in one-quarter of full-scale increments both increasing and decreasing (observing any problems with zero shifts). The final step in the calibration procedure consists of proof loading the balance to verify the accuracy of the derived interactions. The proof

loading consists of approximatley 100 different combinations of full and half loads which are applied to the balance in a predetermined manner. Using the derived calibration constants, the forces and moments are then calculated from the gage output and compared with the applied proof loads. The accuracy of the balance is then quoted as being +/-0.5 percent of design load if all the errors calculated during the proof loads fall within that band. Clearly, the calibration of a strain-gage balance is a very time consuming and complex task.

A balance is usually chosen for a test so that the load capability on any axis does not exceed the maximum expected load by more than 10 or 15 percent. In this way low load levels will not be overwhelmed by the error which, as we have noted, is proportional to the maximum design load. Experience has shown that most balances are more accurate than the quoted values. This is most apparent where incremental rather than absolute measurements are being made. Also, additional accuracy can be achieved by doing a number of careful repeat runs.

Electronically Scanned Pressure Systems

A photograph of a 32-channel ESP is shown in figure 34. Its major components are : the 32-chanel ESP module, the data acquisition and control unit (DACU), and the pressure calibration unit (PCU). The ESP module consists of 32 solid state piezoresistive pressure sensors, a 32-channel analog multiplexer, an instrumentation amplifier, and a two-position pneumatic switch.[38] The two-position pressure switch is a slide plate with drilled holes that allows the calibration pressures to be routed to each of the pressure sensors through a common manifold in one position or to allow the individual pressure lines connected to the pressure-post plate to be applied directly to the pressure sensors in the other position.

ESP systems in use at LaRC cover full-scale ranges from 1 to 100 psi differential and 5 to 100 psi absolute. ESP modules are used in thermally controlled environments ranging from 40F to 150F. In general, the measurement uncertainty for the ESP system is 0.15 percent of the sensor full scale range where the calibration standard in the pressure calibration unit has the same range as the sensor module. However, LaRC has a few ESP systems where this is not true. For example, the 1 psid system at the 14- by 22-Foot Subsonic Tunnel and LFC airfoil in the 8-Ft. TPT uses a 6 psid standard to calibrate the 1 psid modules and the measurement uncertainty is no better 0.002 psi or approximately 0.2 percent of the 1 psi full range.

The NTF system which requires 200 psia calibration standards in the pressure calibration unit has a basic uncertainty of 0.04 psi from the standard itself. When the other factors are considered such as the sensor nonrepeatability, thermal control, module reference pressure measurement, the error can be as much as 0.5 percent of full scale for 5 psi modules down to a base system accuracy of about 0.25 percent of full scale for ranges up to 45 psi. As in the case of strain gage balances, the accuracy of a measurement deteriorates when it is made at the low end of the pressure range of the instrument.

Hot Film Gages

There are a number of types of hot-film gages in use and they have a variety of functions including the measurement of heat transfer, skin friction, transition, separation, and reattachment. All of these quantities are related to the shear stress at the wall and this is what the hot films are sensitive to. Hot-films can be calibrated where qualitative data is required by the use of boundary layer profiles, calorimeters, or a direct measuring flush-surface, skin-fricition sensor. However, hot-film sensors are most often used to make qualitative measurements.[35,39,40] The signal output from hot-film gages can be analyzed to determine the start and end of transition as well as the most amplified distrubance frequency leading to transition. It was also demonstrated in reference 39 that an analysis of the gage outputs below 10 Hz can yield the points of separation and reattachment.

Hot-film gages are fabricated in many different ways and come as single gages or in arrays. Single-sensor patch gages have been used for a number of years and are available from several commercial vendors. Figure 35 shows the installation of a number of patch gages on a laminar flow airfoil in the LTPT. Since these gages are bonded to the surface they protrude into the boundary layer and cause transition. When several gages are used at different chordwise locations, they must be displaced laterally from each other so that the turbulent wake from one gage will not wash over another. A typical wave form and spectrum from a patch, hot-film gage are plotted in figure 36. Also shown are the results of a stability calculation which shows that the most amplified frequencies are in agreement with the spectral data. These results are similar to those obtained from other types of thin film gages.

Plug-type hot-film gages have been used as both transition and skin friction gages. They have the advantage of beiny flush with the surface and, consequently, do not cause the flow to transition. The laminar flow control (LFC) experiment uses a large number of plug gages to determine the regions of laminar and turbulent flow.

Several hot-film-array concepts have been invented and applied successfully during the past few years. One concept deposits the leads and sensors directly on an insulative coating which has previously been deposited on the surface of the model.[40] Figure 37 gives the details of such a system recently developed at Langley. The leads are made of aluminum and the sensor of nickle and chrome; the insulative substrate is made of paroline "C". The whole system is less than 0.00035-in thick. A photograph of an array of these hot-film gages deposited on a metallic insert is shown in figure 38. This insert was fitted to the upper surface of a NACA 0012 airfoil and tested in a low-speed calibration wind tunnel. A photograph of the RMS voltage outputs and time traces from a number of gages along the chord of the airfoil are given in figure 39. The different character of the time traces in the laminar, transitional, and turbulent regions of the flow is quite evident. Note also in figure 39 that the transition process takes place over 15 percent of the chord. The successful prediction of the drag for this geometry and flow situation would have to model, with some accuracy, this flow phenomena; few codes even attempt it. On the experimental side we have seen in figures 29 and 31 that the wind-tunnel environment has a strong effect on the start and end of transition. There are experiments[28,29] which address this problem but more should be carried out in super-flow-quality facilities and in flight with high-resolution instrumentation.

Another hot-film array that deserves attention is one where the sensors are deposited on a polyimide film. Figure 40 shows the sensor array that was deposited on film for use in several recent airfoil tests. Gages are spaced about every one-tenth of an inch and the leaos extend out to the tunnel wall where they are connected to the anemometer leads. With this kind of resolution most of the important flow features can be resolved. Recently it was discovered[39] that if the output signal was filtered to 10Hz a signal reversal at separation and reattachment became evident. Figure 41 shows this phase-reversal character of the filtered output signals from gages installed on a laminar flow airfoil, LRN(1)-1010.

Separation bubbles will usually have some unsteadiness associated with their locations. The larger the bubble the more unsteady the flow will become. Separation without reattachment will lead to unsteady vortex shedding and considerable movement of the separation point. Calculations of this type of flow will benefit from having real time data from hot-film arrays such as those just described.

Hot Wire Anemometers

Hot-wire anemometers have been used for decades to measure the flow quality in wind tunnels and to probe boundary layers of various aircraft components, flat plates, and bodies of various descriptions. Most of the time single-wire probles were used to measure mass fluctuations and with various assumptions, or an unsteady pressure measurement, derive velocity flucuations.[41] In 1980 Stainback developed a data reduction technique to go with a 3-wire hot-wire probe that eliminated the need for the most damaging assumptions. Photographs of a 3-wire probe and of the 3-wire head are shown in figure 42. The idea behind the 3-wire probe is to calibrate the 3 wires for density, velocity, and temperature sensitivities. With the sensitivities known for each wire a 3- by 3-matrix can be solved at each instant of time using the classical equation.

$$\frac{e'}{E} = S_u \left(\frac{u'}{u}\right) + S_\rho \left(\frac{\rho'}{\rho}\right) + S_{T_t} \left(\frac{T_t'}{T_t}\right) \qquad (1)$$

Once the instantaneous ρ, u, and T_t are known the values of instantaneous p on m can be calculated. An example of the sensitivity coefficients obtianed in the calibration process is given in figure 43. Curves like those in figure 43 must be fitted for each wire using curve fit routines for substitution in equation 1. Clearly the precision with which this is done affects the accuracy of the instantaneous values of u, ρ, and T_t derived.

For single wire techniques, the log of the wire voltage output is calibrated against the log of the mass flux. When this is done at low speed the points tend to plot on a single line giving rise to an accurate sensitivity of voltage to mass flux. At high speeds the points cannot be correlated as seen in figure 44.[35] A single straight line fairing of the data shown on the figure as Method I, is only a fair approximation. Of course this approach does not account for the effects of temperture flucuations.

Once the fluctuating mass flux is obtained the RMS fluctuating longitudinal velocity may be obtained from

$$\frac{\tilde{u}}{u} = \frac{\sqrt{(m'/m)^2 + (p'/p)^2}}{\left[1 + (\gamma - 1) M^2\right]} \qquad (2)$$

and a companion unsteady pressure measurement.

Another single wire approach is the use of the data at the pressure of the test to determine the mass flux sensitivity coefficient. This approach is labeled Method II on figure 44. Obviously this only applies over a limited Mach number range.

Figure 45 shows the variation of the normalized fluctuating velocity with Mach number for the two single wire (plus unsteady pressure sensor) methods and the 3-wire techniques. Neither single wire approach agrees very well with the 3-wire result even at a Mach number of 0.4. Mass fluctuations obtained by the three techniques are in similar disagreement.

There is another experiment that has been conducted which adds support for the 3-wire techniques.[35] Recently a 3-D orthogonal LDV system was installed in the Langley Basic Aerodynamis Research Facility (BARF) and measurements of the longitudinal velocity fluctuations were made. A 3-wire hot wire was used to "probe" the same flow. The latter measurements were also used to derive single-wire u/u values based on Method I. Preliminary results from these experiments are plotted in figure 46. It can be seen from this figure that the levels of u/u from the 3-wire probe and the laser LDV are about the same and that the single wire data is much lower.

What the above results mean is that there is a lot of erroneous data in the literature. Judgements of the relative flow quality of one wind tunnel facility versus another based on single-wire data may be in error. Wind tunnel surveys carried out years ago need to be redone. Finally all of our thinking about what constitutes good flow quality at subsonic and transonic speeds will have to be overhauled.

While we have just looked at RMS velocity fluctuations, it does not mean that the spectral content of the u fluctuations (or the other quantities) are not important. Boundary layer instabilities occur at special frequencies and it is the energy of the disturbed onset flow in the vicinity of these frequencies that have the most effect on transition. Therefore, the spectra obtained by 3-wire-probe measurements in wind tunnels have to be examined as well.

Laser Velocimeters

Lasers are used for many purposes in experimental research including point measurements of mean velocity, unsteady velocity, Reynolds stresses and transition. In addition, they are used for vapor-screen flow visualization and laser induced fluorescence techniques. Lasers provide the light sources for both doppler velocimeters and transit anemometers; the former use forward or back scattered radiation and come, primarily, in two and three component systems.

The errors associated with dual beam fringe type LV systems can generally be grouped into three catagories:

1. Optical
   - o Seeding
   - o Fringe Bias
   - o Velocity gradient
   - o Spatial resolution
2. Electronic
   - o Signal to Noise ratio
   - o Total period resolution
   - o Threshold settings
   - o Filter settings
3. Computer interfacing and software
   - o Digitization
   - o Velocity bias
   - o Random sampling

This is not an exhaustive list of error sources, but is intended to give an idea of the difficulty of making accurate measurements. Many of these error sources have been resolved and are adequately addressed in the literature, reference 42-47. The dominate errors are usually found in the optical category and are related to seeding problems. The state of the art in error analysis due to seeding are probably the least understood of the aforementioned errors, particularly at high speeds.

There is a basic conflict in the concept of seeding. That is the LV system would like a large particle which would be easy to detect, however, the large particle may not "track" or follow the streamlines due to it's inability to respond to rapid velocity changes in the flow field. Intuitively it can be seen that seeding selection influences the electronic setup (i.e., threshold settings and filter settings), which effect signal to noise ratios and sampling rates. For incompressible flow fields particles on the order of 1 micron generally meet both the visibility and fluid dynamic criteria mentioned above. Using a solid particulate is usually more desirable than evaporating liquid particulate due to the ability to fix size and mass of the measured particle. The disadvantage of solid particulate is that it fouls the wind tunnel anti-turbulence screens.

Generally the errors in turbulence measurements are functions of the errors in the mean measurement, as the Reynolds stresses are functions of the turbulence measurements. Conventional hot-wire turbulence measurements can usually subtract the mean from the total measurement via a high pass filter, then amplify the fluctuations. This results in a high signal

to noise ratio. On the other hand, LV systems must utilize individual mean measurements therefore subtracting two large values.

Another potential error source is the beam arrangement in three-component velocity measurements. Where optical access does not permit an orthogonal beam arrangement and a single axis system must be used, errors in the "on axis" component can be large. Reference 48 describes the problem and shows why the orthogonal system is the most accurate. A photograph of the orthogonal system now installed in the Basic Aerodynamic Research Facility (BARF) is shown in figure 47. The key feature, of course, is that the beam used to measure the crosswise, or lateral, velocity component comes down from the top and thus is orthogonal to the component it is helping to measure.

Geometry Definition and Accuracy

The geometry of a model can be measured with good accuracy and used in the calculations that are going to be compared the experimental data. Therefore, there is no need to rely solely on the model drawings, as is often done, for the geometry input into our codes. At transonic speeds there is a well known sensitivity of the wing pressures to small changes (just a few thousands) in the surface coordinates. Drag is extremely sensitive to the accuracy with which the leading edge is constructed and the thickness of the trailing edge.

If the model has features that are not represented in the code such as flap-actuator fairings, nose booms, cockpit/canopy details, juncture fairings, and flow-thru nacelles, then additional "errors" will be seen in the computation that must be rationalized. As everyone knows the geometry used for a validation model must be well defined and capable of replication in the code to be validated. What may not be so clear is that it is not just sufficient to know the geometry of a model as manufactured but we must know it under load. The next section deals with this problem.

Aeroelasticity

A factor that can have a significant effect on the correlation between 3-D calculations and experimental data (particularly at transonic speeds) is the static aeroelastic deflection on the wing. For a typical aft-swept transport wing, the upward bending of the wing increases the twist (washout), thus reducing the lift over the outboard portion of the wing. Additional washout from torsional bending is produced by the negative pitching moment associated with aft-loaded airfoils. This compounds the effect on supercritical airfoils, which are especially sensitive to changes in angle of attack.

The effects of static aeroelastic defections are generally more pronounced in flight data than in wind tunnel results; however, tunnels that utilize an increase in pressure to obtain higher Reynolds numbers may produce loadings that can significantly deflect even a solid metal wing. These aeroelastic effects for swept wings are generally opposite to Reynolds number effects and can be large enough to completely mask the effects of the increased Reynolds number.[49]

An example of static aeroelastic effects is shown in figure 48. The F-111/Tact supercritical-wing research aircraft was analyzed using the TAPS aeroelastic code [49] for both a rigid and flexible wing. The aerodynamic module used for these calculations was the TAWFIVE full-potential code.[50] The wing structual characteristics were modeled using the flexibility influence coefficient matrix for the flight vehicle with the wing in the 26° sweep position. The calculations were made at a Mach number of 0.85, an angle of attack of 6.29°, and a dynamic pressure of 728 psf. The resulting pressure distributions at a semispan station of 0.92 show the effects of the increased wing twist (washout) for the flexible wing case. The sonic plateau and the moderate shock near 30-percent chord present in the rigid wing results, has been completely eliminated, and the section lift has been reduced to less than half of the rigid wing value.

Few tests are carried out where the shape of the model under load is determined. Even laboratory tests to determine the structural characteristics of the model under load for post-test corrections are seldom done. Yet when tests are carried out at flight Reynolds number most are done at high-dynamic pressure and, consequently, some model deflection. Since flight Reynolds numbers is where we want to validate most codes, this is clearly a "first-order" problem.

Flow Uniformity

Flow uniformity should be a concern in every tunnel but it is ignored in many small facilities because the error incurred is not considered important for the kind of work they do. Some ignore it because they do not have the instrumentation to measure it or the resources to solve the problem if they did. Personnel assigned to large production tunnels, or research tunnels that are particularly concerned with flow physics, usually spend some time trying to make the flow uniform and documenting the non-uniformity that remains.

Pressure pipes, wall pressure orficies, and rakes containing pressure and flow angularity probes are the tools usually used to measure

longitudinal and lateral flow uniformity in the wind tunnel test section. In recent times temperature has also be measured since thermal gradients may cause premature or nonuniform transition and anomalies in pressure distributions as well.

Ventilated tunnel walls have their own special problems with flow uniformity since the plenum surrounding the test section allows a fore and aft and top to bottom communication that is difficult to account for. WIAC procedures, described earlier, are a great aid in reducing the adverse effects of a nonuniform flow but a large number of measurements must be made to employ them.

Surface Finish

Surface finish is a problem for models where thin boundary layers associated with high-Reynolds number tests are involved and where significant runs of laminar flow are expected. Critical roughnesss height criteria must be followed in model fabrication so that excessive drag and/or premature transition are not induced. Figure 49 shows a plot of surface roughness and how it should improve with Reynolds number.[51] Also shown on the figure is the level of finish currently specified for most of our transonic models. Clearly if the Reynolds number of a test approaches 50 to 60 million surface roughness will become a factor. It should be noted that as the requirements go up for better model finishes so does the cost. Many tests are carried out with models with inadequate finishes simply because the adverse effects are not known or the resources are not available to do better.

The measurement of surface finish can be done in several ways. Stylus profilometers and laser devices are available with the former being the most prevalent. Stylus profilometers require that the ball or point of the stylus be moved across the surface. Unfortunately, when this is done it can cause damage to the surface depending on the grain of the material and direction of the machining. Figure 50 shows an electron microscope photograph of a surface that has been measured with a profilometer.[52] The large grooves or furrows that run from the top left to bottom right were made by the stylus, those in the orthogonal direction result from the machined finish. It does appear possible that a contact profilometer can cause its own roughness.

On pressure models the pressure orifices can be another source of roughness. They are known to cause transition[53] and are sometimes large enough with respect to the local boundary layer thickness to cause erroneous pressure readings[54] as well as unwanted crud drag. One cure that has been successful is the use of flush porous plugs in the orifices.[54] Another is to use 0.010-inch diameter orifices instead of the 0.040-inch standard.

COMPUTATIONAL ERRORS

There are hundreds of codes which provide the solutions to dozens of fluid-flow-equation sets from linear potential to the full Navier Stokes. The gemoetries range from a complete aircraft with nacelles and flaps to a simple body of revolution. Some codes have existed long enough and have had sufficient utility that their validation space is quite large; others however, have only been compared by the originator to a few classical test cases. In a few instances, codes have become obsolete before the first results are published due to the rapid growth and improvement in CFD methods and main-frame scientific computers. Overall the trend is toward more accurate, efficient solutions for more complex geometries.

There has never been a computer code for the prediction of the fluid flow past an aircraft or any of its major components that is error free. There are any number of examples, however, where the computational error is small enough that the differences between it and a high quality experimental result are of no consequence. There are also many more where the differences are not trivial nor are they easily explained. It is no great revelation that the number of potential pitfalls, or "error sources," in developing and applying a CFD code are large - a few of the most "prominent" ones are listed in figure 2. In the following sections we will show some examples of most of the "error sources" on the list and, in several cases, how the errors can be minimized.

Math Model/Equation Set

Most fluid-flow-equation sets can be cast either in a conservative or nonconservtive form. The full potential equations are no exception. Throughout the 70's there was considerable disagreement over whether the conservative or nonconservative formulations yielded the most accurate solution. One of the first papers to draw attention to the large differences in the solutions that could be obtained from the two formulations was by Newman and South.[55] They solved for the flow about a simple biconvex airfoil at Mach numbers of 0.8 and 0.95. At the lower Mach number figure 51 shows that the nonconservative and conservative schemes give approximately the same pressure distribution with the "conservative" shock slightly downstream of the "nonconservative" one. However, for the higher Mach number, and even more supercritical flow, the two formu-

lations give quite different results. The nonconservative solution gives a strong shock at the trailing edge while the conservative scheme yields a weak oblique shock at the trailing edge followed by a normal shock located about a half chord downstream of the trailing edge.

Computed streamlines for the same two Mach numbers as for the pressure distributions are shown in figure 52. Normally one expects in an inviscid calculation for the streamlines to come back to the same vertical location far downstream as they had far upstream. The displacement of the downstream streamlines from their far upstream ordinate, ($\Delta y/c$), has been labeled. Note that the ordinates of the streamlines themselves have been amplified by a factor of 20. Streamlines for the conservative based solutions for both the low and high Mach number cases come back to their original ordinate ($\frac{\Delta y}{c} = 0.000$) . The nonconservative streamlines do not return to their far upstream values at either Mach number and the displacements at a Mach number of 0.95 are quite large.

The reason for the displacement of the nonconservative streamlines is that the nonconservative differencing across the shock gives rise to an effective source term. The stronger the shock the more displacement one sees of the streamline.

The problem of conservative versus nonconservative formulations was also very much in the forefront in a workshop held in Braunschweig, Germany in 1981.[56] Its purpose was to compare the results from a number of codes for several previously specified test cases. Summary plots of the calculated lift and drag coefficients for one of the test airfoils, the NACA 0012 airfoil, are given in figure 53. Shown in this figure are the bounds of the many predictions from nonconservative and conservative potential formulations as well as those based on the Euler equations. The free-stream conditions for the calculation are listed on the abscissa and indicate Mach numbers from 0.63 to 0.95 and angles of attack from 0 to 2 degrees.

The results in figure 53 concerning the relative merit of the conservative and nonconservative schemes are mixed. The drag coefficients for the NCPOT and FCPOT methods agree quite well with the Euler solutions at the lower Mach numbers but at the higher Mach numbers the FCPOT results were in better agreement with the Euler calculations than those of the NCPOT. In contrast, the Mach number 0.85, $\alpha = 1^0$ and 0.80, $\alpha = 1.25^0$ results for the lift coefficient show the NCPOT calculation to give the best agreement with the Euler calculation. Aside from the relative merits of the different methods it is important to notice the tremendous scatter of the results for both potential-equation formulations.

The calculated results presented in figure 53 stem from the application of inviscid methods. Most of the differences stem from the ability of the various solution techniques to predict the shock pressure jump and the associated wave drag and lift changes. However, if one desires to make a proper drag prediction then he must include a boundary layer in his computation; lift predictions are generally less sensitive to the displacement and shear effects of the boundary layer except at transonic speeds. One of the first interactive boundary-layer/inviscid wing-flow calculations using a nonlinear potential code was carried out by Caughey et al. in 1978.[57] In this calculation FLO-22 was "matched" to the two-dimensional Nash-McDonald integral boundary-layer method in streamwise strips. The wing had an aspect ratio of 10.3, a sweep of 27 degrees at the quarter-chord line, and a thickness ratio ranging from 14.9 percent at the root to 10.6 percent at the tip. The free-stream Mach number of the test was 0.79 but the codes were run at a 0.01 higher Mach number to account, in an approximate way, for the effect of the fuselage. The experiment was conducted in the Langley 8-Foot TPT at a chord Reynolds number of 2.4×10^6.

Figure 54 shows the wing pressure distribution resulting from an inviscid/viscous calculation, along with a purely inviscid calculation, at the 45 percent wing semi-span location. It is evident from the figure that the boundary layer has a significant effect on the pressure distribution, particularly on the top surface. The suction peak, shock location, and shock jump are all better predicted by the viscous calculation. It should be noted that both calculations were run at the same lift coefficient. Most of us have seen similar calculations for both 2-D and 3-D flows and the picture is qualitatively the same. However, different boundary layer methods and turbulence models can have a noticable effect on the results.

The effects of the boundary layer on wing pressures can be looked at from a slightly "higher perch" than those just discussed. At present there are a number of Euler and Thin Layer Navier-Stokes (TLNS) codes, some with the ability to handle quite complex geometries. Several of the TLNS codes have been programmed so that the viscous terms can be turned off and they can be run as Euler codes. There are also a few Euler codes which include an interactive boundary-layer routine. Consequently there are many opportunities to evaluate, on a theoretical basis, how much error is incurred when we apply an Euler code without a boundary layer.

Vatsa in reference 58 presented pressure distributions for the ONERA M6 wing at M = 0.84 and $\alpha = 6.06^0$ for both the Euler and TLNS equation sets. An example result is shown in figure 55 for the 65-percent span station. The grids for these two calculations are essentially the same except additional grid is added near the surface in the one for the TLNS equations to resolve the boudary layer. The surface mesh is identical in both calculations.

The results shown for the 65-percent span station are typical of those at other locations. It can be seen that the Euler calculation provides a shock that is as much as 20 percent downstream of the experimental location. There is also a large overshoot of the pressure at the foot of the shock. The TLNS result shows a more upstream shock location and the overshoot at the foot is reduced from that of the Euler equations. The smearing, or plateauing, of the pressure downstream of the shock is indicative of flow separation and even the TLNS does not predict it very well. Still the results are encouraging when one realizes that an equilibrium, algebraic turbulence model has been used. These models are known to be deficient in the calculation of separated flows and empirical fixes are sometimes employed to improve their performance.

A math model "error" of a slightly different character concerns the specification of the state of the boundary layer. Most delta wing calculations using Navier-Stokes equations are made with the laminar flow form of the viscous terms. Hartwich and Hsu in reference 59 modified their thin TLNS code to run in the fully turbulent mode, or with transition specified at some desired chordwise location.

The utility of the transition "modification" is demonstrated in a comparison of computed flow-field results with experimental data for a sharp-edged delta wing (AR = 1) at $\alpha = 20.5^0$ and a root chord Reynolds number of 0.9 million. Figure 56 shows spanwise pressure distributions at the root chord stations x/c = 0.5 and 0.9 for this case. In one computation, the flow is assumed to be fully laminar, whereas in the other calculation, transitional flow is simulated by assuming laminar flow along the windward wing surface, and by fixing the laminar/turbulent transition on the leeward side at x/c = 0.6. At x/c = 0.5, the computations differ only marginally and predict quite well the strength and position of the primary and secondary vortices. The effect of transition is clearly seen for x/c = 0.9; the fully laminar computation considerably overpredicts the strength of the secondary vortex while the calculation with transition modeling brings the pressure distribution into much closer agreement with the experimental data.

The possibilities for drawing comparisons between results derived from different equation sets are unlimited. Generally the more complete the fluid flow equation or math model the smaller the errors become, except where viscous effects, shock jumps, boundary conditions, or the solution algorithm are mishandled or ill chosen. The next section takes a look at the last of these--solution algorithm.

Solution Algorithm

Several years ago when Euler-equation solution methods were in the forefront of CFD developments, the realization that vorticity induced by shocks in the flow field could lead to "realistic" flow separation caused quite a stir. M. Salas explored this phenomena for the flow about a cylinder. His results caused others to "take a crack" at the calculation and a comparison of their results for the pressure distribution and separated flow regions was made.[60] Figure 57 shows the separation "bubbles" for a free-stream Mach number of 0.5 determined from four separate codes all were based on the Euler equations except that of Hafez. The large differences shown in figure 57 indicate a high sensitivity of the separation point to the solution technique employed.

Another example of how the solution technique for a given set of equations can have a profound effect on the calculated results is documented in reference 61. This paper gives a comparison of half-a-dozen numerical flux formulas for the convection terms in the Euler and Navier-Stokes equations. The authors utilized several of the formulas in a Navier-Stokes code due to Newsome[62] and subsequently applied it to the flow over a cone at a Mach number of 7.95. Figure 58 shows in a graphical way the relative merit of the flux vector splitting formula of Van Leer[63] to the flux difference scheme of Roe.[64] It shows that the normalized temperature distribution across the boundary layer, flow field and shock is essentially independent of the cell size for the Roe scheme and quite sensitive and somewhat inaccurate for that of Van Leer. The correct surface temperature ratio of 11.7 is never reached by the flux-vector splitting formula (FVS) of Van Leer. The analysis of reference 61 indicates that for an accurate representation of both the shock and boundary layers "the flux formula must include information about all the different characteristic waves by which neighboring cells interact, as in Roe's flux-difference splitting". Only a few have this quality.

A further test of the "efficiency" of FDS relative to FVS schemes has been made by Rumsey and Anderson[65] in studying the time varying flow over a NACA 0015 airfoil. Reduced frequencies of 0.2 and 0.6 were used which yields pitch rates of

250°/sec. and 750°/sec. for a 10-foot chord airfoil at M = 0.2 (see figure 59). The airfoil was started initially at 0° angle of attack at the previously stated rates and stopped at an angle of attack of 60°. A C-grid was used as illustrated in figure 60 for the calculation with 257 grid points normal to the airfoil and wake and 97 grid points wrapped around it.

Velocity vectors and vorticity contours for $\alpha = 30^0$ and k = 0.2 are given in figures 61 and 62 resulting from the FDS and the FVS calculations, respectively. Three plots are shown on each figure for successive grid refinements to demonstrate, as in the cone calculation, the sensitivity of the results to the flux splitting scheme. It is clear from these figures and others in reference 65 that flux difference splitting is again superior to flux vector splitting.

Other flux-splitting techniques examined in reference 61, except for that of Harten-Lax and Osher, were found to be deficient leading, in some cases, to the need for added dissipation to quiet oscillations near discontinuities or contact surfaces. Certainly the flux formulas that yield the most accuracy for the minimum grid are the ones most likely to give less error in a "black-box" application.

The use of higher order differences to increase accuracy and/or use fewer grid points for a given level of accuracy has always been a CFD "judgement call". However, if one is going "all out" for accuracy, as one might do in a validation excerise, then both fine grids and higher-order differences schemes might be employed. Hartwich in reference 66 shows the improvement possible in going from a first order to a third order upwind calculation of the flow about an AR = 1, flat delta wing. The full incompressible, laminar Navier-Stokes equations are solved on the O-H grid depicted in figure 63 where 51, 101, and 66 points are used in the radial, spanwise, and longitudinal directions, respectively.

Figure 64 shows the first order calculation on the left and the third order on the right for a Re_{c_R} = 0.9 milion. It is immediately apparent that the first order calculation badly underestimates the experimental pressure levels in the outboard region of the wing and fails to generate the secondary vortex near the leading edge seen in both the third-order calculation and experiment. Bottom side pressures are uneffected by going from first-order to third-order differences. These calculations demonstrate quite well the virtue of the higher order schemes for flows with large gradients and a specified grid.

Higher order differences schemes can also be used to advantage in unsteady-flow calculations. Bayliss et.al[67] have developed a compressible Navier-Stokes boundary-layer simulation code which is second order in time and second or fourth order in space. Unsteady mass fluctuations are introduced at the upstream boundary as perturbations to a steady boundary-layer profile and Mach = 0.4, Re = 3 x 10^5 mean flow. At the upstream (inflow) boundary, Re_δ^* = 998 and the computational domain is chosen so that at the outflow boundary Re_δ^* = 1730.

The time warying behavior of ρu at two downstream locations Re_δ^* = 1263, y = 0.0034 ft, and Re_δ^* = 1481, y = 0.0011 ft and for both second and fourth special differences are given in figure 65. Results for Re_δ^* = 1481, the left hand figure, indicates significant amplitude and phase differences. The ρu amplitude differences between second-and fourth-order calculations for Re_δ^* = 1481 (right hand plot) are even more dramatic. In addition, the fourth order results shows some nonlinear effects not in evidence in the second-order calculations.

Artificial Viscosity/Dissipation

This error source could easily have been included in the discussion of flux-splitting schemes since flux-splitting formulas inherently give rise to dissipation. If the "effective" damping of a numerical scheme is deficient then artificial dissipation may be required for a stable calculation. Furthermore, when dissipation terms are added their functional form must be carefully selected. It was noted in reference 68 that the basic dissipation model, used so successfully by Jameson[69] and co-workers for Euler solutions, encounters difficulty when used in the TLNS equation. Part of the reason seems to lie in the fact that extremely fine mesh spacing is required near solid-wall boundaries in the body-normal direction resulting in very high aspect ratio cells.[68]

Reference 70 has compared the dissipation terms in Jameson's Runge-Kutta scheme to those of Roe[64] and found that the former should be scaled with a linear function of velocity in order to be comparable with those inherent in Roe's upwind scheme. Since Roe's flux-splitting formula provides the minimum dissipation required for stability then one would expect the modified dissipation terms in the TLNS code to yield a more accurate calculation. The ratio of local to free-stream Mach number has been chosen as the scaling function and TLNS calculations have been made with and without this factor on the Runge-Kutta dissipation terms.

An untapered, 20° swept semi-span wing mounted on a wind-tunnel wall was chosen so that comparisons could be made with the data of Lockman and Seegmiller.[71] A sample result is given in figure 66 at the wing mid-span location for a Mach number of 0.826, $Re_{\bar{c}} = 8 \times 10^6$ and an angle of attack of 2°. It is quite evident from this figure that the modified dissipation model gives a much better prediction of the shock location and jump on the upper surface, and of the peak suction pressures on both the top and bottom surfaces.

An understanding of the effects of natural or artificial dissipation is crucial to the assessment of the accuracy of the Navier-Stokes calculations. Artificial viscosity and the smearing, or additional shear, it provides must be small compared to that which stems from "real" viscosity. More numerical experiments aimed at this issue are needed.

Boundary Conditions

As everyone knows boundary conditions play a very important role in any calculation an if mishandled can have disastrous consequences. More often than not when CFD researchers apply boundary conditions that are not exact, or at the right place, they do it with a full knowledge of the possible error. The use of small disturbance equations and planar boundary conditions is the source of one of the most common boundary condition errors. However, these equations have great utility and the errors can be limited by the right choice of geometries and, to a degree, free-stream conditions. In some cases the detailes of the flow at the front of a blunt body or on a wing leading edge may be degraded relative to that provided by "large-disturbance" equations and exact boundary conditions but the overall characteristics are usually well predicted. Drag and transition predictions may suffer.

The far-field boundary conditions are frequently misapplied. They may not be placed far enough away from the configuration to represent the far field or they may reflect waves back into the solution domain when, if formulated correctly, they will be nonreflective. Frequently at the downstream boundary a linear extropolation of flow variables is made that may not be warranted at the location they are applied.

In a recent TLNS calculation of the flow about a semispan wing mounted on the wind tunnel sidewall, Vatsa[68] could not achieve simultaneous agreement with the experimental inflow and downstream conditions. Calculations were then carried out for two values of the back pressure ratio (p_b / p_∞) which bracketed the experimental in flow conditions. The results of these calculations and how they effect the pressure distribution on the wing are shown in figure 67. The higher value of back pressure ratio seems to do a much better job than the lower one particularly on the lower surface.

There is a large sensitivity of the inflow condition to back pressure ratio at the Mach number of these tests, 0.826. Wall boundary layers, not represented in the calculations shown in figure 67, will slightly alter this relationship. An examination of the wing and tunnel-wall (not shown) pressures for the lower value of back pressure results in an inflow Mach number that is somewhat higher than the data whereas the higher back pressure results in an inflow Mach number which, as noted, yields much better agreement with the data. Clearly in the transonic regieme the specification of the downstream boundary conditions is important.

While most of us are aware of the need for "proper" far-field boundary conditions it is instructive to look at the magnitude of the problem that we avoid when they are correctly specified. We can do this in an approximate way by examining the TLNS results given in reference 68 for free-air and solid-wall tunnel boundaries. The wing is the same semi span one used in the previous calculations (also see discussion of figure 66) and the Mach number is still 0.826. Figure 68 shows that the calculated free-air pressure distribution is quite different from the in-tunnel one due primarily to the more forward shock location on both the top and bottom surfaces. This indicates, as most would expect, a lower Mach number over the wing in free air than in the tunnel. A point made in the Wind Tunnel Wall Interference section and reinforced by figure 68 is the large effect wind-tunel walls can have on the accuracy of our data. The use of a free-air code to correlate with this data is clearly inappropriate.

Uniqueness

Mathematicians worry about the uniqueness of solutions, more or less, as a necessary part of doing business. But for most CFD practitioners there is only one uniqueness test, and that is, "is it consistent with his expectations based on data, other codes, intution, etc?" Only when one gets a bad answer does one dare think of uniqueness. Consequently, when a paper was published in 1981 indicating that a much used airfoil code could produce spurious results, there was considerable concern.

In reference 72 it was shown that within a certain range of angle of attack and free-stream Mach number, numerical solutions of the full-potential equation (solved in the conservative form) for flow past an airfoil are not unique.

The thrust of reference 72 was that the anomaly is inherent to the partial differential equation. Results were presented for two alternative solutions of the flow past an 11.8-percent thick symmetric Joukowski airfoil at a Mach number of 0.837 and zero angle of attack. The pressure distributions derived are plotted in figure 69. The solution plotted on the left of this figure is symmetric while that on the right is clearly unsymmetric. Many checks were made to certify the accuracy of the computations.

Salas, Gumbert, and Turkel[73] did an in depth study of this nonuniqueness problem and found that the phenomenon was associated with a "breakdown in potential approximation" rather than a real-flow anomaly. They also showed that the solution to the full potential equation was continuous and multivalued. Figure 70 shows this behavior for an NACA 0012 airfoil at a Mach number of 0.83 along with calculations from an Euler code and the Prandtl-Glauret thin airfoil approximation.

$$c_l = 2\pi\alpha \sqrt{1 - M^2}$$

The Euler results clearly have no anomalous behavior.

Double valued c_l curves are only obtained for the NACA 0012 airfoil over a small Mach number range, roughly 0.82 to 0.86, but even outside this band the potential results do not agree very well with those of the Euler equations.

Calculations made subsequent to those of reference 73 have shown that the double valued c_l problem is only obtained when the conservative form of the potential equation is used. It has also been demonstrated that the problem not only exists for airfoil calculations but for wings as well.[74]

Grid Resolution

The selection of a grid for a given equation set and geometry is of equal importance to the selection of the solution technique. If the grid selected does not naturally refine in regions of rapid flow changes then some embedded or adaptive grid scheme may be in order. An excellent source of information on three dimensional grid generation for complex equations is a recent AGARDagraph by Thompson, Steger, Yoshihara[75] and many other contributors. For a wing, Erickson[76] has found from comparing different mesh topologies for use with the Euler equation that the O-O topology gives the best resolution for the fewest number of points. However, for the Navier Stokes equations, it is preferable to use a C grid in the chordwise directions in order to permit the accurate resolution of the wake downstream of the trailing edge as well as the boundary layer on the wing. With this in mid Vatsa[58] chose a C-O grid to construct a TLNS code for wings. A sample grid used in the analysis of the ONERA M6 wing is shown in figure 71. It is evident from this figure that the required clustering of the grid points close to the wing surface and in the wake is achieved.

A grid refinement study was carried out by Vatsa[58] starting first with a subcritical case ($M = 0.699$, $\alpha = 3.06$) and focusing on the effect of streamwise gridpoint density. The initial calculations were for a grid of 97 x 49 x 17 (streamwise, normal, spanwise) node points; a second calculation was performed with twice as many streamwise points yielding a 193 x 49 x 17 grid. Comparisons of the pressure distributions produced by the previously described grids with experimental data were made a three spanwise locations in reference 58, only the one at $\zeta = 0.65$ will be shown here (see figure 72). The agreement between the predictions and the data is good everywhere except in the region of the suction peak where the 97 x 49 x 17 grid result does rather poorly.

Reference 58 also shows pressure calculations, for the same two grids used in the subcritical case, at a supercritical Mach number, $M = 0.84$, and an angle of attack of 3.06°. The sensitivity of the pressure distributions to the streamwise grid refinement in this case can be seen in figure 73. As in the subcritical case the coarser grid, 97 x 49 x 17, does not resolve the suction peak very well. Also, the predicted shocks are badly smeared. Even the shock resolution of the 193 x 49 x 71 grid is not satisfactory. This was thought to be more of a spanwise resolution problem than a streamwise one, partly due to a merging of the double inboard shock into a strong λ shock in the outboard region. A further refinement of the spanwise grid was then carried out with a 193 x 49 x 33 mesh and the results (figure 74) do show some improvement in the shock jump at a x/c of 0.2. It should be remembered that while we are trying to adjust our calculations to fit the data, the data itself may have errors just as large as the ones we are seeking to reduce.

A similar exercise to that just described for a large aspect ratio wing has been carried out by Harwich[66] for a delta wing with an aspect ratio of one. His study also includes the effect of a leading-edge vortex, an important flow feature that requires accurate definition. The grid shown is of the O-H type with the O grid in the cross plane. A third order upwind differencing scheme has been used to solve the incompressible Navier-Stokes equations on grids of 51 x 51 x 60

(radial, spanwise, longitudinal) and 51 x 101 x 66. Consequently the increased resolution in going from the first grid to the second is in the spanwise direction.

Results for the coarser grid, and experimental data due to Hummel shown in figure 75, indicate that the predicted levels of pressure agree fairly well with experiment and the suction peaks that occur under the vortex are in the right place. However, the flattening of the pressures near the leading edge that is caused by the secondary vortex is not "picked up" at all. The fine grid calculation on the right of figure 75 clearly shows the evidence of a secondary vortex and, consequently, agrees better with the experimental data.

A better appreciation of the differences in the flow pattern resulting from the two grids can be obtained from the contours of total pressure plotted in figure 76. Both full-span and part-span plots (global and local) are given, the latter enabling an enlarged view of the tip flow field and much better pictures of the secondary vortex particularly the one produced by the fine-grid calculation.

Most of the grid-sensitivity studies, like the majority of the CFD codes, are done for steady-state flows. Conclusions based on these studies may not carry over to time dependent flows where there may be additional requirements. Rumsey and Anderson[77] have carried out an investigation of a number of potential error sources in airfoil calculations, both steady and unsteady. A sample result from this grid sensitivity study for an oscillating airfoil is displayed in figure 77. Plotted in this figure are the time varying c_l and c_m for three grids as a function of angle of attack which is given by

$$\alpha(t) = \alpha_0 + \alpha_1 \sin(Mkt)$$

The grid refinements used represent a factor of 4 difference in the number of grid points on each axis in going from the coarse to the fine grid.

Comparison of the calculated section lift-coefficient and pitching-moment curves with the experimental data of Landon shows that the coarsest grid does a fair job and the two finer grids do quite well. It can also be seen that results for the two finer grids are little different from each other. The agreement with pitching moment is not as good as that for lift for any of the grids.

The time varying motion of bodies and the pressure or velocity waves that they create can be effected by the ability of a grid to propagate those waves in an undistorted fashion.[78]

Recently S. R. Bland[79] investigated this phenomena in a simple yet revealing way using the wave equation. In his study the wave equation with initial conditions is solved on several finite-difference grids using an implicit method that is second order accurate in x and t with outgoing-wave (radiation) boundary conditions. The mathematical problem solved is

$$u_{xx} = u_{tt} \qquad u(x,o) = e^{-\left(\frac{3x}{4}\right)^2} \cdot \cos(\pi x)$$

$$u_t(x,o) = o$$

The finite-difference equations on a uniform grid are

$$\frac{u_{j-1}^{n+1} - 2u_j^{n+1} + u_{j+1}^{n+1}}{\Delta x^2} = \frac{2u_j^{n+1} - 5u_j^n + 4u_j^{n-1} - u_j^{n-2}}{\Delta x^2}$$

Figure 78, which gives the exact solution, shows that the initial wave pocket divides into two pieces propagating to the left and right with half the original amplitude. In subsequent figures the computational solutions are given for a uniform fine, uniform coarse and streched grid. Figure 79 shows the solution on a uniform fine mesh. There are eight x-grid points per period of the initial wave. Some error is detachable in the solution including distortion of the wave form, in both shape and propagation speed, and barely detectable boundary reflections. Overall it compares favorably with the exact solution.

The solution on a uniform coarse mesh (figure 80) has four x-grid points per period of the initial wave. Clearly, the wave is badly distorted and internal grid reflections are apparent long before reflections from the boundaries become a factor.

Finally figure 81 shows the solution on a stretched grid containing the same number of points (49) as the uniform coarse grid. The spacing near the boundaries is so large that most of the initial wave energy is trapped within the computational domain. Disturbances continue to reflect within the domain and do not die out with time. Significant reflections begin to occur when the x-grid spacing has less than four points per period of the initial wave.

In most computations the grid used in the near field is quite adequate to resolve both steady and unsteady waves but the far field grid, where stretched grids are used, can be a source of error.

Our last example of grid problems relates to types of grid used and how it can effect the

solutions. Raj in 1984 using FLO 57, Euler-equation technology examined various kinds of C-H and C-O grids in solving for the flow over an arrow wing.[80] Results due to Raj for the two types of C-H grids shown in figures 82 and 83, and for the same arrow wing are plotted in figure 84. Although the resolution of the experimental data is poor in the spanwise direction (the pressure taps in the arrow-wing model were arranged in seven chordwise rows)[81] it is still clear that the algebraic grid is superior to the parabolic one. This is due to the fact that the sparsity of points near the wing surface provided by the parabolic grid does not allow adequate resolution of the tip vortex. Both grids could be refined for improved results but the algebraic grid would still be superior. Obviously the grid system has to be chosen with one eye on the geometry and the other on the flow phenomena expected. The same point was made earlier in connection with figure 71.

Turbulence Modeling

In demonstrating the effect that the turbulence model can have on a calculation we can take advantage of the turbulence model sensitivity studies contained in papers already referenced. One[58] contains calculations over the ONERA M6 wing using the standard and a modified Baldwin-Lomax model. The modification consists of a relaxation scheme similar to that developed by Shang and Hankey.[82] The intent of the modification is to include upstream effects particularly in separated flow regions such as occur under strong shocks. Details of the modification is given in reference 58.

Computed results for the standard and relaxation turbulence models are shown in figure 85 along with ONERA M6 data. Both calculations and experiment are for a Mach number of 0.84 and an angle of attack of 6.06 degrees. The standard model appears to give a shock location that is further downstream than that of the data. Furthermore the steepness of the calculated shock jump indicates that the physics of the separated flow at the foot of the shock has not been captured. The relaxation model does move the shock forward into better agreement with the experiment but still the pressures in the separated flow region are not accurately predicted.

Another turbulence-sensitivity study was conducted by Rumsey and Anderson.[77] Their calculations were made for two airfoil sections, the NACA 0012, and the RAE 2822, and for Mach numbers providing both subcritical and supercritical flows. The two turbulence models that they examined were the Baldwin-Lomax and the Johnson-King. Overall the Johnson-King model performed better, particularly in the neighborhood of shocks. Figure 86 shows perhaps the most extreme case from reference 77 and it gives results for the NACA 0012 airfoil at a Mach number 0.799, angle of attack of 2.26 degrees, and a Reynolds number of 9×10^6. C_f and C_p distributions plotted in this figure show that a much larger separation bubble is predicted by the Johnson-King model under the shock than by the Baldwin-Lomax. This in turn gives rise to a much better prediction of the shock location and the pressures just downstream of the shock.

Reynolds Number

The last error source we will discuss is that of Reynolds number. In code application this error arises when a code is not run at the Reynolds number of the experiment; for full Navier-Stokes calculations, including transition and turbulence simulations, a large enough computer may not be available or there may not be enough computer time. Reynolds number effects are also important to the transition criteria and the turbulence model. A study just conducted by Harwich and his co-workers of an ogive of revolutions at high angles of attack looks at both of these effects.[83]

The objective of their study was to numerically assess Reynolds number effects on low-speed (M = 0.1 - 0.3) vortical flows over tangent ogive-cylinders at moderate angles of attack for Re_c = 0.2 - 0.8 million. An attempt was made to computationally simulate the two most challenging types of crossflow separation: 1) a flow with a laminar separation bubble and a subsequent transition in the separated shear layer which forms the primary vortex, and 2) fully turbulent crossflow separation. The flow-field results are steady-state solutions to the three-dimensional incompressible Navier-Stokes equations in their thin-layer approximation. An implicit upwind finite-difference method with the upwinding based on flux-difference splitting is used to obtain solutions.

Good to excellent agreement with experimental data has been achieved after a refined version of the Baldwin-Lomax turbulence model has been implemented in the code. By monitoring the solution in crossplanes, the Baldwin-Lomax turbulence model with the modifications by Dagani and Schiff is invoked only in regions of massive crossflow separation. Marching from the windward towards the leeside meridian along a circumferential grid line typically six step sizes off the body surface, the onset of massive separation is defined at the first occurrence of a negative product of two consecutive crossflow velocities. The transition from laminar to turbulent attached flow is estimated by using the

Esch factor which approximates the effects of angle of attack on the streamline length.

The computations are carried out on 65 x 73 x 40 and 97 x 91 x 40 grids for $\alpha = 20^0$ and $\alpha = 30^0$, respectively (see figure 87). The grid point counts refer to the radial, circumferential, and longitudinal coordinate direction of a C-O type grid ("C" in longitudinal direction and "O" in circumferential direction).

Figure 88 shows the computed circumferential pressure distributions for two Reynolds numbers, 0.2 and 0.8 x 10^6, and at two longitudinal locations. The curves shown are for a fully turbulent flow. Reynolds number effects are apparent in this figure particularly in the magnitude and location of the suction peaks under the separated vortex. Overall the experimental differences due to Reynolds number are smaller than those obtained by the TLNS code. Finally it is clear that the calculations made at a Reynolds number of 0.2 x 10^6 are only a fair approximation of those carried out at 0.8 x 10^6.

Concluding Remarks

A number of examples of error sources in CFD codes and wind-tunnel tests have been presented. No attempt has been made to pick the most impressive, or "best" examples nor has there been any effort to minimize any of the error sources. The main objective has been to give them credibility and, in a few cases, show how they are minimized or corrected.

Many of the examples were taken from papers that were themselves aimed at providing a better understanding of one or more error sources. They are indicative of the increased effort being expended, by both experimentalists and CFD practitioners, to reduce the error in their product. On the experimental side large sums of money have been spent in the past decade to reduce the Reynolds number gap and to improve flow quality. Efforts to provide accurate wall-interference correction procedures are now starting to pay large dividends and improved nonintrusive instrumentation is seeing increased use. There are many other signs that experimental researchers are becoming more accuracy minded and this is certainly one of the "pros" in the "pros and cons" of the code validation process.

Theoreticians are equally active on the"accuracy front." Comprehensive studies of the effects of grid type and size, of turbulence models, and of solution schemes regularly appear in the literature. The increased emphasis on Navier-Stokes codes has provided another positive element since it raises the expectations of the CFD "fraternity" and puts more pressure on the experimentalists. Interest in transition and turbulence has grown and with it the amount of research effort and money devoted to the area. No small player in all of this is the continuing improvement of our large scientific computers.

In assessing the overall status of theory versus experiment it is clear to most everyone that the former is improving faster. This is not something to either get alarmed, or "crow" about; it has been the trend for a very long time. Remember that wind-tunnel research had a big head start. Experimental research still has one tremendous advantage, it has the right turbulence model and in a "free-transition" test the transition process is more realistic. Several super-flow-quality tunnels, that will enable better transition simulations, have been proposed and hopefully will be built in the next few years.

The area where CFD codes are competitive with experiment is in the simulation of attached flows. Eddy viscosity and two equation turbulence models do a good job in most situations except in juctures and at wing tips where further improvement is needed. We have shown results from several airfoil tests where the wall interference effects were so large that the CFD result was clearly more accurate. When large runs of laminar flow and transition are critical features of the test, the wind-tunnel environment will degrade the data accuracy and CFD may yield a more accurate result in this instance as well.

In attached flow situations the need for off-surface measurements to help validate a code is greatly reduced. Theoretically the amount of work required when attached flows are expected can also be reduced. Higher-order-panel and nonlinear-potential methods when interacted with a boundary layer can provide answers nearly equivalent (sometimes better) to that of a Navier-Stokes code. Where separated flows are a concern, Navier-Stokes codes should come to the forefront but they are still plagued by the lack of accurate transition and turbulence models. In trying to validate Navier-Stokes codes at conditions that yield separated flows, there is also the problem of unsteadiness. Most separated flows are unsteady and the state-of-the-art instrumentation for flow-field diagnostics can only measure the time varying flow quantities at a single point. We need, of course, to be able to measure time varying flow variables along a line or in a plane. Until we do, the validation of Navier-Stokes codes will be limited. The value of good flow visualization techniques in this environment cannot be overstated.

In summary the error sources that the experimentalists have worked on so long are still a concern. Our knowledge of, and ability to cope with, wind tunnel wall and sting interference, Reynolds number effects, and flow quality and transition has increased greatly but the application is spotty. In addition, instrumentation for unsteady measurements and aeroelastic effects should be added to the list of primary concerns. For the theoreticians transition and turbulence are still the key modeling issues; user friendliness and solution-algorithm efficiency are still of primary importance and will remain so. Clearly there is a very long list of "cons" or error sources; nevertheless, the ongoing research provides many indications that their number and/or impact will shrink dramatically in the next decade and the list of high-order validated codes will grow in proportion - a very big "pro" indeed.

REFERENCES

1. Baals, Donald D.; and Corliss, William R.: Wind Tunnels of NASA. NASA SP-440, 1981.

2. Kemp, W. B., Jr.: "Toward the Correctable - Interference Transonic Wind Tunnel. AIAA 9th Aerodynamic Testing Conference, June 1976, pp. 31-38.

3. Kemp, W. B., Jr.: Transonic Assessment of Two-Dimensional Wind-Tunnel Wall Interference Using Measured Wall Pressure. NASA CP-2045, 1978, pp. 473-486.

4. Kemp, W. B., Jr.: TWINTAN: A Program for Transonic Wall Interference Assessment in Two-Dimensional Wind Tunnels. NASA TM-81819, 1980.

5. Kemp, W. B., Jr.; and Adcock, J. B.: Combined Four-Wall Interference Assessment in Two-Dimensional Airfoil Tests. AIAA Paper 82-0586, 1982. (AIAA J., vol. 21, no. 10, 1983, pp. 1353-1359).

6. Kemp, W. B., Jr.: TWINTN4: A Program For Transonic Four-Wall Interference Assessment in Two-Dimensional Wind Tunnels. NASA CR-3777, 1984.

7. Gumbert, C. R.; Newman, R. A.; Kemp, W. B., Jr.; and Adcock, J. B.: Adaptation of a Four-Wall Interference Assessment/Correction Procedure for Airfoil Tests in the 0.3-m TCT. NASA CP-2319, 1984, pp. 393-411.

8. Gumbert, C. R.; and Newman, P. A.: Validation of a Wall Interference Assessment/Correction Procedure for Airfoil Tests in the Langley 0.3-m Transonic Cryogenic Tunnel. AIAA Paper 84-2151, 1984.

9. Gumbert, C. R.: User Manual for 0.3-m TCT Wall-Interference Assessment/Correction Procedure: 8- by 24-Inch Airfoil Test Section. NASA TM-87582, 1985.

10. Green, L. L.; and Newman, P. A.: Transonic Wall Interference Assessment and Corrections for Airfoil Data from the 0.3-m TCT Adaptive Wall Test Section. AIAA Paper 87-1431, 1987.

11. Green, L. L.: Wall Interference Assessment and Corrections for Transonic Adaptive Wall Airfoil Data. Masters Thesis, George Washington University, April 1988.

12. Gumbert, G. R.: Wall Interference Assessment/Correction of Data from Tests of a CAST 10-2/DOA 2 Airfoil in the Langley 0.3-m Transonic Cryogenic Tunnel. Masters Thesis, Geogre Washington University, May 1988.

13. Rizk, M. H.; Hafez, M.; Murman, E. M.; and Lovell, D.: Transonic Wind Tunnel Interference Corrections for Three-Dimensional Models. AIAA Paper 82-0588.

14. Rizk, M. H; and Murman, E. M.: Wind Tunnel Wall Interference Corrections for Aircraft Models in the Transonic Regime. J. Aircraft, vol. 21, no.1, 1984, pp. 54-61.

15. Rizk, M. H.; Smithmeyer, M. G.; and Murman, E. M.: Wind Tunnel Wall Interference Corrections for Aircraft Models. NASA CP-2319, 1984, pp. 301-322.

16. Rizk, M. H.: Improvements in Code TUNCOR for Calculating Wall Interference Corrections in the Transonic Regime. AEDC-TR-86-6, 1986.

17. Kemp, W. B., Jr.: A Panel Method Procedure for Interference Assessment in Slotted-Wall Wind Tunnels. AIAA Paper 88-2537, 1988.

18. Newman, P. A.; Kemp, W. B., Jr.; Garriz, J. A.: Wall Interference Assessment and Corrections. Presented at the Transonic Symposium, NASA Langley Research Center, Hampton, Virginia, April 19-21, 1988. (To be published in NASA CP).

19. McKinney, L. W.; Bruce, W. E., Jr.; and Gloss, B. B.: National Transonic Facility Status. Presented at the Transonic Symposium, NASA Langley Research Center, Hampton, Virginia, April 19-21, 1988. (To be published in NASA CP).

20. Frink, Neal T.: Computational Study of Wind-Tunnel Wall Effects on Flow Field Around Delta Wings. AIAA Paper 87-2420, August 1987.

21. Boyden, R. P.; and Tcheng, P. Status of Magnetic Suspension Technology. NASA CP-2397, Paper No. 14, January 1986.

22. Johnson, Joseph L.; Grafton, Sue B.; and Yip, Long P.: Exploratory Investigation of Vortex Bursting on the High Angle-of-Attack Lateral-Directional Stability Characteristics of Highly-Swept Wings. Presented at the AIAA 11th Aerodynamic Testing Conference, Colorado Springs, Colorado, March 1980.

23. Dietz, W. E.; and Altstatt, M. D.: Experimental Investigation of Support Interference on an Ogive-Cylinder at High Incidence. J. Spacecraft and Rockets, vol. 16, Jan.-Feb. 1979, pp. 67-68. See also AIAA Paper 78-165, January 1978.

24. Kilgore, Robert A.; Goodyer, Michael J.; Adcock, Jerry B; and Davenport, Edwin E.: The Cryogenic Wind-Tunnel Concept for High Reynolds Number Testing. NASA TN D-7762, 1984.

25. Waggoner, E. G.; and Allison, D. O.: EA-6B High Lift Wing Modifications. AIAA Paper 87-2360, August 1987.

26. Ladson, Charles L.; and Ray, Edward J.: Status of Advanced Airfoil Tests in the Langley 0.3-Meter Transonic Cryogenic Tunnel. NASA CP-2208, September 1981.

27. Stainback, P. Calvin; and Owen F. Kevin: Dynamic Flow Quality Measurements in the Langley Low Turbulence Pressure Tunnel. AIAA Paper 84-0621.

28. Dougherty, N. S.: Influences of Wind Tunnel Noise on the Location of Boundary-Layer Transition on Slender Cone at Mach Numbers from 0.2 to 5.6, Vol. I, Experimental Methods and Summary of Results and Vol. II, Tabulated and Plotted Data. AEDC-TR-78-44, March 1980.

29. Dougherty, N. S., Jr.; and Fisher D. F.: Boundary Layer Transition on a 10-Degree Cone: Wind Tunnel/Flight Data Correlation. AIAA Paper 80-0154, January 14-16, 1980.

30. Lawson, M. V.: Prediction of Boundary Layer Pressure Flucutations. AFFD-TR-67-167, April 1968.

31. Harvey, W. D.; and Bobbitt, P. J.: Some Anomalies Between Wind Tunnel and Flight Transition Results. AIAA Paper 81-1225, June 1981.

32. Blackwell, James A., Jr.: Preliminary Study of Effects of Reynolds Number and Boundary Layer Location on Shock Induced Separation. NASA TN D-5003, 1969.

33. Beckwith, I. E.; Chen, F. -J.; and Malik, M. R.: Design and Fabrication Requirements for Low-Noise Supersonic/Hypersonic Wind Tunnels. AIAA Paper 88-0143, January 1988.

34. Chen, F. -J.; and Malik, M. R.: Comparison of Boundary Layer Transition on a Cone and Flat Plate at Mach 3.5. AIAA Paper 88-0411, January 1988.

35. Bobbitt, Percy J.: Instrumentation Advances for Transonic Testing. Presented at the Transonic Symposium, NASA Langley Research Center, Hampton, Virginia, April 19-21, 1988. (To be published in NASA CP).

36. Weinstein, L. M.; Beeler, G. B.; and Lindemann, A. M.: High-Speed Holocinematographic Velocimeter for Studying Turbulent Flow Control Physics. AIAA Paper 85-0526, March 1985.

37. Weinstein, Leonard M.; and Beeler, George B.: Flow Measurements in a Water Tunnel Using a Helocinematographic Velocimeter. AGARD-CP-413, pp. 16-1 to 16-7.

38. Mitchell, Michael: Pressure Measurement System for the National Transonic Facility. NASA CP-2122, Part II, pp. 317-327, November 1979.

39. Stack, John P.; Mangalam, Siva M.; and Kalburgi Vijay: The Phase Reversal Phenomenon at Flow Separation and Reattachment. AIAA Paper 88-0408, January 1988.

40. Johnson, Charles B.; Carraway, Debra L.; Hopson, Purnell, Jr.; and Tran, Sang Q.: Status of a Specialized Boundary Layer Transition Detection System for Use in the U.S. National Transonic Facility. Presented at the 12th International Congress on Instrumentation in Aerospace Simulation Facilities, Williamsburg, Virginia, June 22-25, 1987.

41. Stainback, P. Calvin; and Johnson, Charles B.: Appendix: A Probe and Data Reduction Technique for Obtaining Hot Wire Data at Transonic Speeds. NASA CP-2183, December 1980, pp. 113-115.

42. Drain, L. E.: Laser Doppler Measurements. John Wiley and Sons, New York, 1980.

43. Durst, F.; Melling A.; and Whitelaw, J. H.: Principles and Practice of Laser-Doppler Anemometry. Second Edition, Academic Press, New York, 1981.

44. Buchave, P.: The Measurement of Turbulence with the Burts-type Laser Doppler Anemometer - Errors and Correction Methods. TLR-106, State University of New York at Buffalo.

45. Bachalo, W. D.; Houser, M. J.; and Smith, J. N.: Behavior of Sprays Produced by Pressure Atomizers as Measured Using a Phase/Doppler Instrument. Atomization and Spray Technology 3, 1987, pp. 53-72.

46. Edwards, R. V.; and Jensen, A. S.: Particle-Sampling Statistics in Laser Anemometers: Sampled-and Hold Systems and Saturable Systems. J. Fluid Mechanics, vol. 133, 1983, pp. 397-441.

47. Yata, W. J.: Measurements of Aerosol Size Distributions with a Laser Doppler Velocimeter (LDV), AIAA Paper 73-705, July 1973.

48. Meyers, James F.: The Elusive Third Component. Proceedings of the Symposium on Laser Anamometery, ASME 1985 Winter Annual Meeting, Miami, Florida, November 1985, oo, 247-254.

49. Campbell, R. L.: Calculated Effects of Varying Reynolds Number and Dynamic Pressure on Flexible Wings at Transonic Speeds. NASA CP-2327, 1984, pp. 309-327.

50. Melson, N. D.; and Street, C. L.: TAWFIVE: A User's Guide. NASA TM-84619, September 1983.

51. Nikuradse, J.: Stromungsgesetze in Rohren. Forschungsheft 361, 1963.

52. Gloss, Blair B.: Some Aerodynamic Considerations Related to Surface Definition. NASA CP-2122, Part II, November 1979.

53. Somers, Dan M.; Stack, John P.; and Harvey, William D. Influence of Surface Static-Pressure Orifices on Boundary-Layer Transition. NASA TM-84492, July 1982.

54. Plentovich, E. B.: The Application to Airfoils of a Technique for Reducing Orific-Induced Pressure Error at High Reynolds Numbers. NASA TP-2537, January 1986.

55. Newman, Perry A.; and South, Jerry C., Jr.: Influence of Nonconservative Differencing on Transonic Streamline Shapes. AIAA Journal vol. 14, no. 8, August 1976, pp. 1148-1149.

56. Rizzi, Arthur; and Viviand Henri: Collective Comparision of the Solutions to the Workshop Problems. Notes on Numerical Fluid Mechanics, vol. 3, Numerical Methods for the Computation of Inviscid Transonic Flows with Shock Waves, Friedr. Vieweg and Sohn Verlagsgesellschaft mbH, Braunschweig, 1981.

57. Caughey, David A.; Newman, Perry A.; and Jameson, Antony: Recent Experiences with Three-Dimensional Transonic Potential Flow Calculations. NASA TM-78733, July 1978.

58. Vatsa, V. N.: Accurate Numerical Solutions for Transonic Viscous Flow Over Finite Wings. AIAA Journal, vol. 24, no. 6, June 1987, pp. 377-385.

59. Hartwich, P. M.; and Hsu, C. H.: High Resolution Upwind Schemes for the Three-Dimensional Incompressible Navier-Stokes Equations. AIAA Journal, vol. 26, no. 7, July 1988.

60. Salas, Manuel D.: Recent Developments in Transonic Euler Flow Over a Circular Cylinder. Mathematics and Computers in Simulation, vol. 25, 1983, pp. 232-236.

61. Van Leer, Bram; Thomas, James L.; Roe, Philip L.; and Newsome, Richard W.: A Comparison of Numerical Flux Formulas for the Euler and Navier-Stokes Equations. AIAA Paper 87-1104CP, June 1987.

62. Newsome, R. W.: The Comparison of Euler and Navier-Stokes Solutions for Supersonic Flow Over a Conical Delta Wing. AIAA Paper 85-0111, January 1985.

63. Van Leer, B.: Flux-Vector Splitting for the Euler Equations. Lecture Notes in Physics, vol. 170, 1982, pp. 501-512.

64. Roe, P.: Approximate Riemann Solvers, Parameter Vectors, and Difference Schemes. Journal of Computational Physics, vol. 43, 1981, pp. 357-372.

65. Rumsey, Christopher L.; and Anderson, Kyle W.: Some Numerical and Physical Aspects of Unsteady Navier-Stokes Computations Over Airfoils Using Dynamic Meshes. AIAA Paper 88-0329, January 1988.

66. Hartwich, P. -M. and Hsu, C. -H.: High Resolution Upwind Schemes for the Three-Dimensional, Incompressible Navier-Stokes Equations. AIAA Paper 87-0547, January 1987.

67. Bayliss, A., Parikh P.; Maestrello, L.; and Turkel, E.: A Fourth-Order Scheme for the Unsteady Compressible Navier-Stokes Equations. AIAA Paper 85-1694, July 1985.

68. Vatsa, V. N. and Wedan, B. W.: Navier-Stokes Solutions for Transonic Flow Over a Wing Mounted in a Tunnel. AIAA Paper 88-0102, January 1988.

69. Jameson, A.; Schmidt, W.; and Turkel, E.: Numerical Solutions of the Euler Equations by Finite Volume Methods Using Runge-Kutta Time Stepping Schemes. AIAA Paper 81-1259, 1981.

70. Vatsa, V. N.; Thomas, J. L.; and Wedan, B. W.: Navier-Stokes Computations of Prolate Spheroids at Angle of Attack. AIAA Paper 87-2627-CP, 1987.

71. Lockman, W. K.; and Seegmiller, H. L.: An Experimental Investigation of the Subcritical and Supercritical Flow About Swept Semispan Wing. NASA Technical Memorandum 84367, June 1983.

72. Steinhoff, John; and Jameson, Antony: Multiple Solutions of the Transonic Potential Flow Equation. AIAA Paper 81-1019, June 1981.

73. Salas, M. D.; Gumbert, C. R.; and Turkel, E.: Nonunique Solutions to the Transonic Potential Flow Equation. AIAA Journal, vol. 22, no. 1, July 1984, pp. 145-146.

74. Gibbons, M. D.; Whitlow, W., Jr.; and Williams, M. H.: Non-Isentropic Unsteady Three Dimensional Small Disturbance Potential Theory. AIAA Paper 86-0863, May 1986.

75. Thompson, J. R.; and Steger, J. L. (edited by Yoshihara H.): Three Dimensional Grid Generation for Complex Configurations--Recent Progress. AGARD-AG-309, March 1988.

76. Ericksson, L. E.: Transfinite Mach Generation and Computer-Aided Analysis of Mach Effects. Ph.D. Thesis, Uppsala University, Uppsala, Sweden, March 1984.

77. Rumsey, Christopher L.; and Anderson, Kyle W.: Parameteric Study of Grid Size, Time Step, and Turbulence Modeling on Navier-Stokes Computations Over Airfoils. Presented at the AGARD 62nd Meeting of the Fluid Dynamics Panel Symposium on Validation of Computational Fluid Dynamics, May 2-5, 1988, Lisbon, Portugal, Paper No. 5.

78. Vichnevetsky, Robert: Wave Propagation and Reflection in Irregular Grids for Hyperbolic Equations. Applied Numerical Mathematics 3 (1987) 133-166.

79. Bland, Samuel R.: Private communication on wave equation solution.

80. Raj, P.; and Sikora, J. S.: Free-Vortex Flows: Recent Encounters with an Euler Code. AIAA Paper 84-0135, January 1984.

81. Manro, M. E.; Manning, K. J.; Hallstaff, T. H.; and Rogers, J. T.: Transnoic Pressure Measurements and Comparison of Theory to Experiment for an Arrow-Wing Comfiguration. NACA CR-2610, August 1976.

82. Shang, J. S.; and Hankey, W. L., Jr.: Numerical Solutions for Supersonic Turbulent Flow Over a Compression Ramp. AIAA Journal Vol. 13, October 1975, pp. 1368-1374.

83. Hartwich, Peter-M.; Hsu, C.-H.; Luckring, James B.; and Liu, C. H.: Aerodynamic Applications of an Efficient Incompressible Navier-Stokes Solver. ICAS-88-5.4.1, 1988.

ACKNOWLEDGEMENTS

The author gratefully acknowledges the assistance of Larry L. Green in assembling the computational error-source material and support throughout the formulation of the paper. He would also like to recognize the following Langley colleagues for their assistance and helpful discussion: S. R. Bland, R. L. Campbell, G. S. Jones, A. T. Ferris, F. A. Kern, V. N. Vatsa, M. D. Salas, J. C. South, Jr., J. L. Thomas, C. L. Rumsey, W. K. Anderson, J. P. Stack, W. D. Harvey, P. A. Newman, P. L. Lawing, C. L. Ladson, L. W. McKinney, D. M. Bushnell, C. B. Johnson, B. B. Gloss, R. P. Boyden, L. Maestrello, W. B. Kemp, P. -M. Harwich (Vigyan Research Associates, Inc.), P. C. Stainback (Complere), and S. M. Mangalam (AS&M, Inc.).

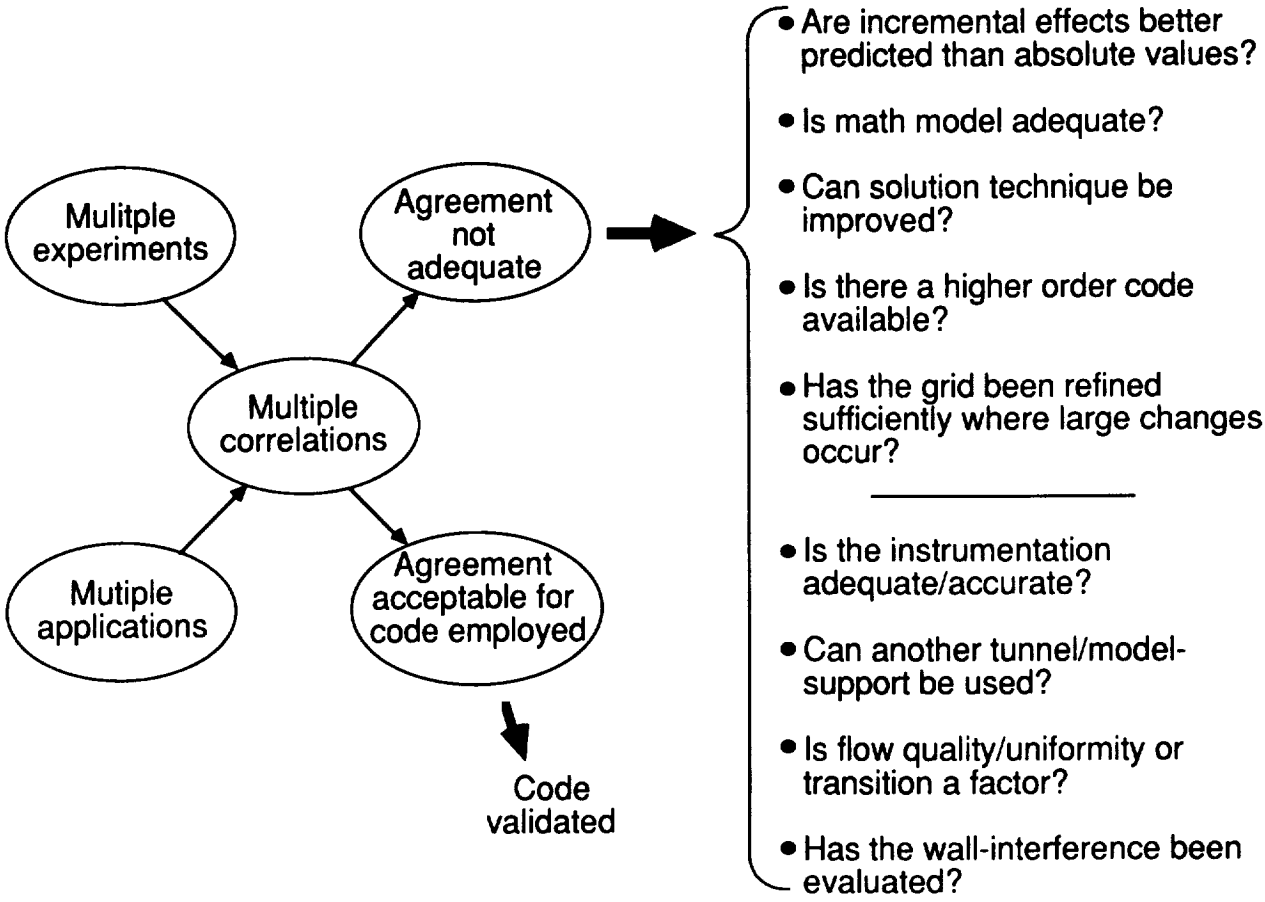

Figure 1. Code validation procedure.

- **Math model/equation set**
- **Solution algorithm**
- **Artificial viscosity/dissipation**
- **Boundary conditions**
- **Uniqueness**
- **Geometry representation**
- **Grid resolution**
- **Grid aspect ratio/grid irregularities**
- **Solution not converged**
- **Turbulence model**
- **Round off error/truncation error**
- **Reynolds number**
- **Bugs**

Figure 2. Error sources in CFD codes.

- **Sting effects**
- **Wall effects**
- **Reynolds number**
- **Flow quality/noise**
- **Transition**
- **Instrumentation**
- **Geometry definition and accuracy**
- **Aeroelasticity**
- **Flow uniformity**
- **Surface finish**

Figure 3. Error sources in wind-tunnel data.

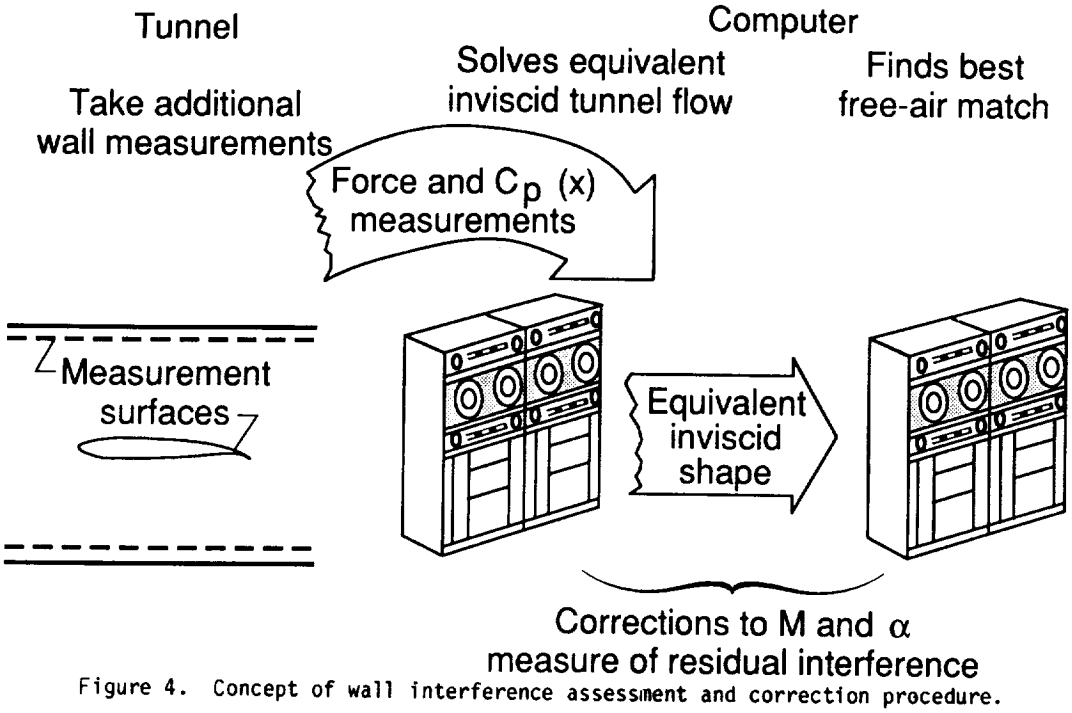

Figure 4. Concept of wall interference assessment and correction procedure.

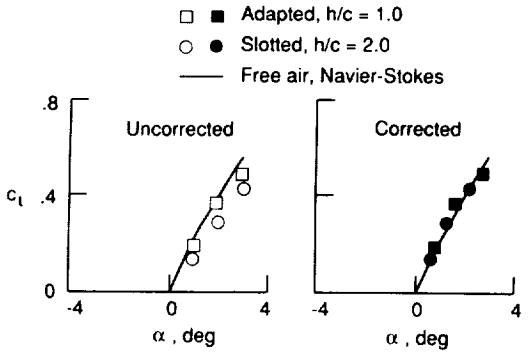

Figure 5. Section lift coefficient with and without WIAC angle-of-attack corrections for both slotted and adaptive-wall test sections. 0.3-m TCT data, NACA 0012 airfoil, M_T = 0.76, Re_c = 9 x 10^6.

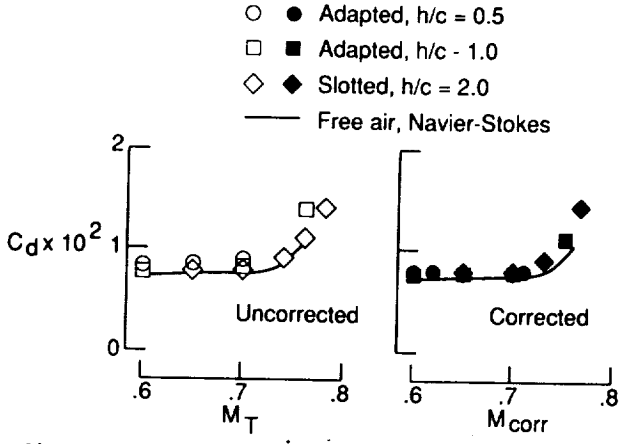

Figure 6. Section drag coefficient with and without Mach number corrections for both slotted and adaptive-wall test sections. 0.3-m TCT data, NACA 0012 airfoil, c_l = 0.2, M_T = 0.76, Re_c = 9 x 10^6.

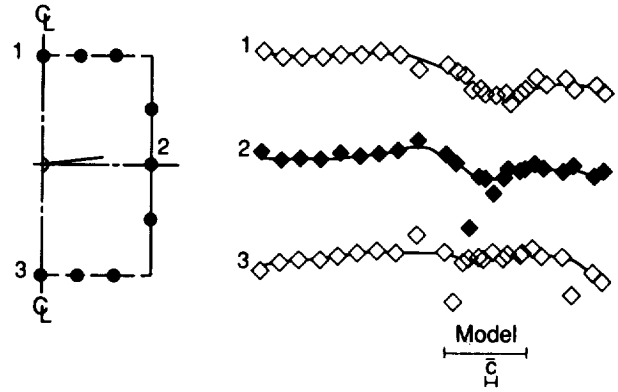

Figure 7. Location of longitudinal rows of tunnel wall pressure taps in the NTF and illustrative pressure variations along three rows with Pathfinder Transport model installed. M_T = 0.8, α_T = 2.2°, $\bar{c}$ = 5.74".

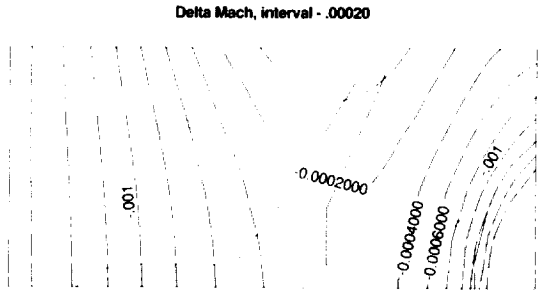

Figure 8.- Contours of equal Mach number corrections for the Pathfinder transport model in the NTF as determined by the linear WIAC code LINCOR. M = 0.8, C_L = 0.514.

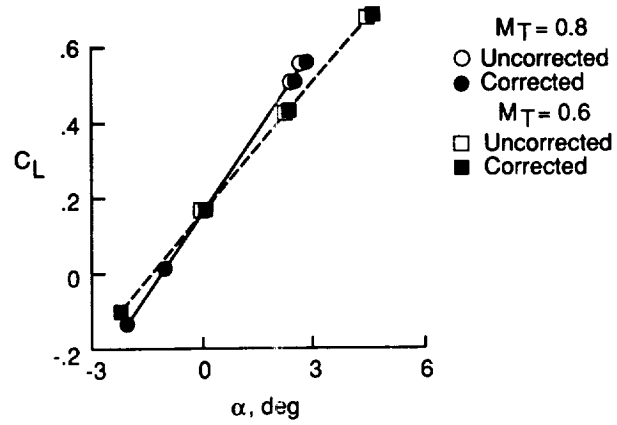

Figure 9. TUNCOR corrections to NTF lift coefficient data for the Pathfinder transport model at two Mach numbers. $Re_{\bar{c}}$ = 2 x 10^6, $\bar{c}$ = 5.74".

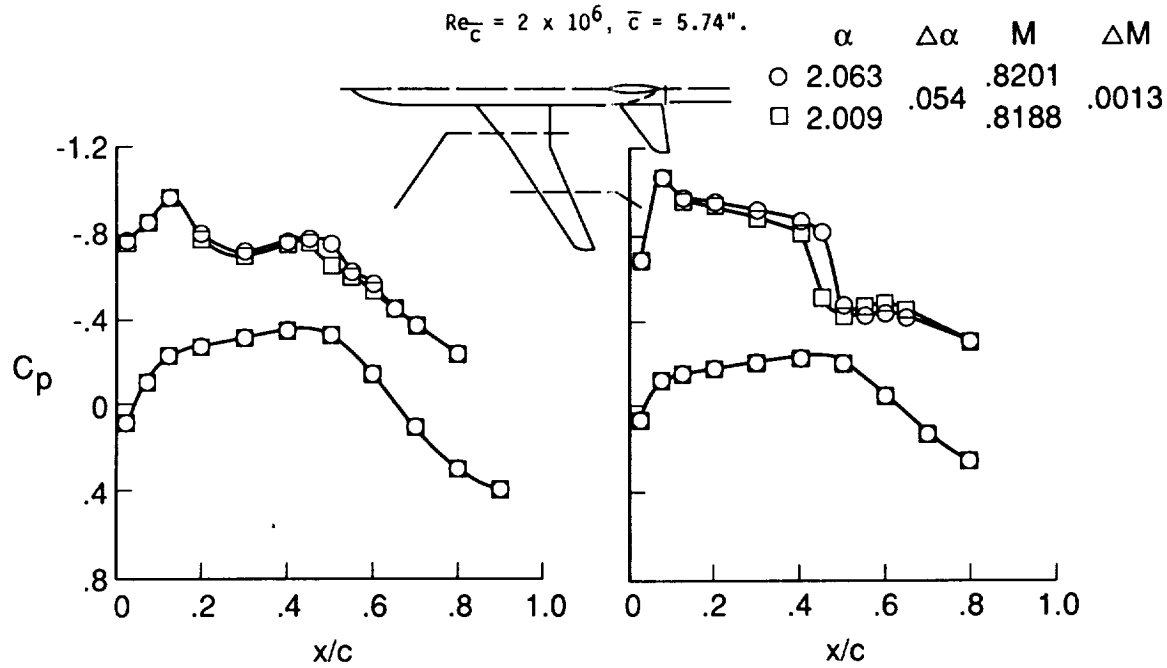

Figure 10. Pressure distributions for two angle-of-attack and Mach number combinations obtained in the NTF on the Pathfinder transport model. $Re_{\bar{c}}$ = 6 x 10^6, $\bar{c}$ = 5.74".

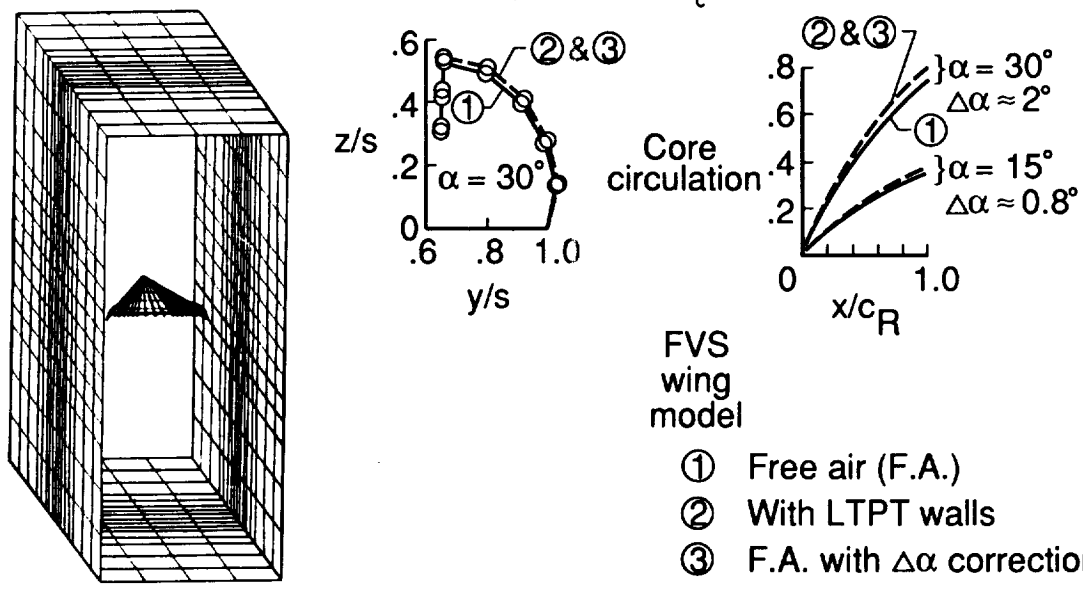

Figure 11. Wind-tunnel-wall effects on the flow around a 65° delta wing as determined by the free vortex sheet (FVS) code. M = 0.22, model/tunnel span = 0.5, vortex sheet plot at x/c_R = 0.5.

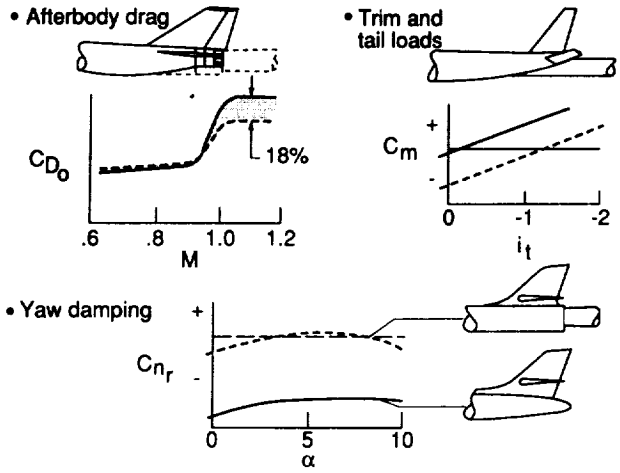

Figure 12. Examples of errors that can arise from model sting supports.

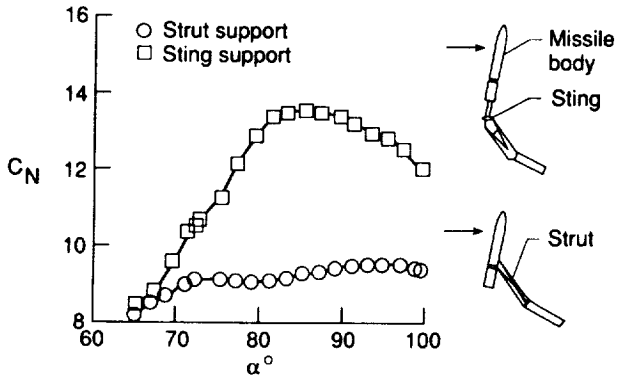

Figure 14. Illustration of the effect of the model support arrangement on C_N for a missile body at high angle of attack.

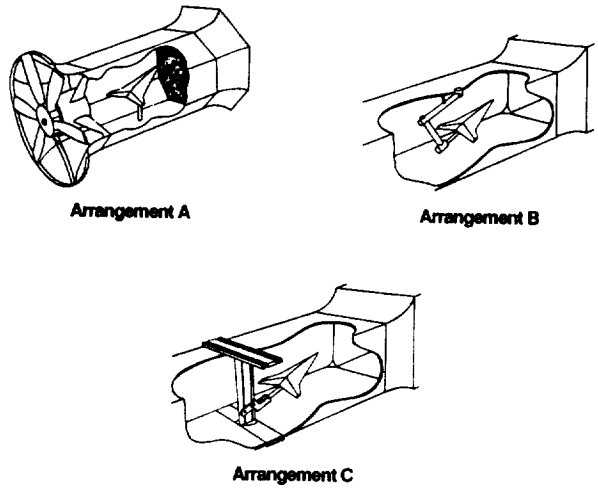

(a) Model support arrangements.

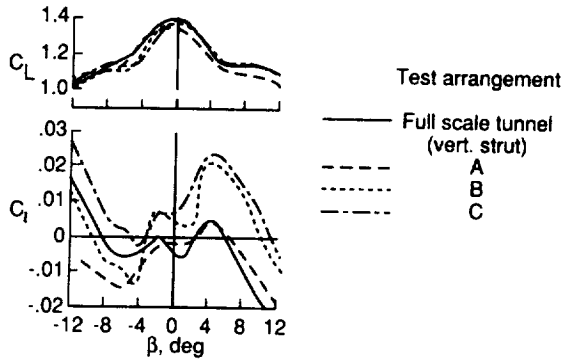

(b) Variation of C_L and C_l with angle of sideslip.

Figure 13.- Sketches of several model support schemes used in an investigation of the effect of angle of sideslip on lift and rolling moment characteristics of a 70° arrow wing. α = 35°.

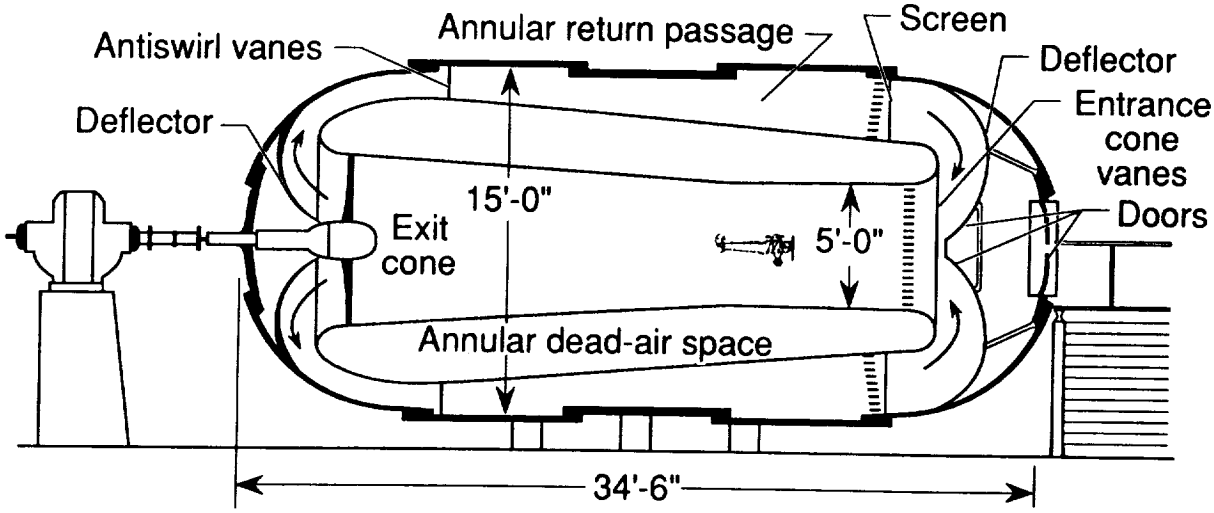

Figure 15. Cross section of the Variable Density Tunnel (VDT) showing the annular flow of returning air.

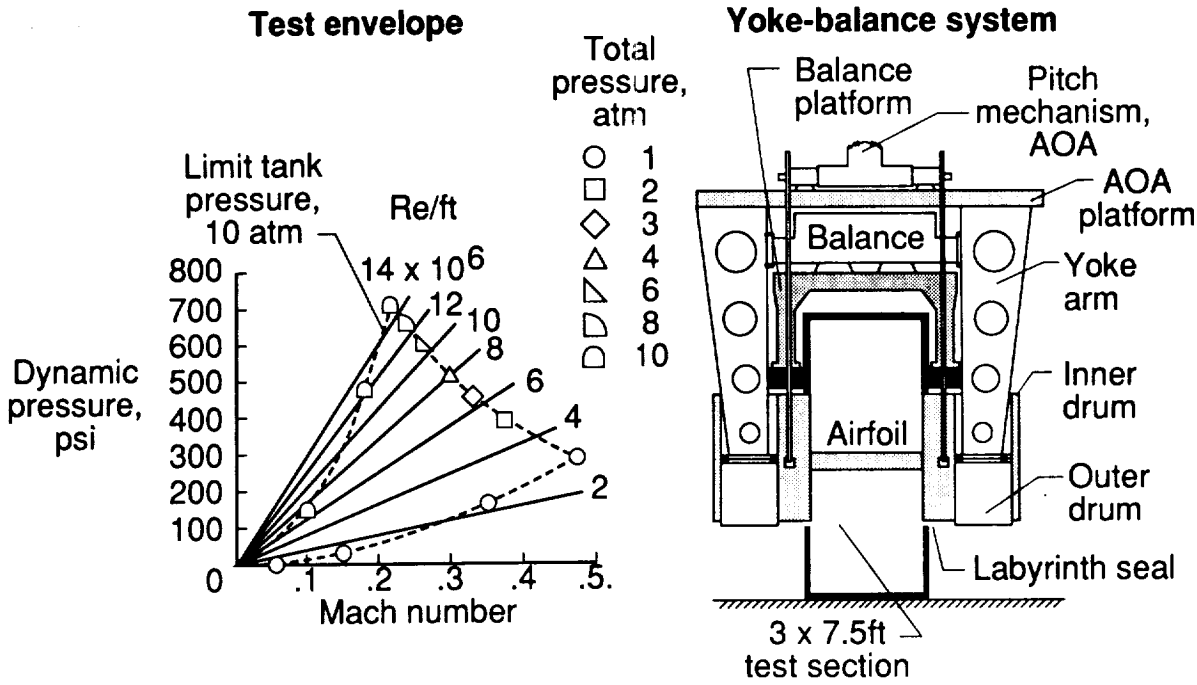

Figure 16. LTPT test envelope and yoke-balance system for high-lift-system testing.

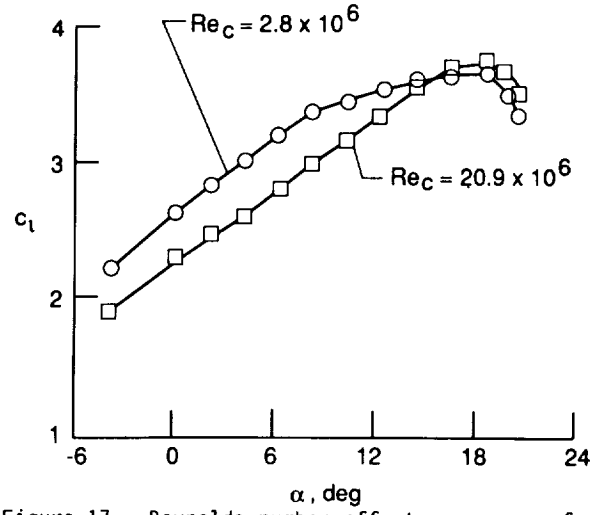

Figure 17. Reynolds number effects on c_l vs α for a four-element high lift system.

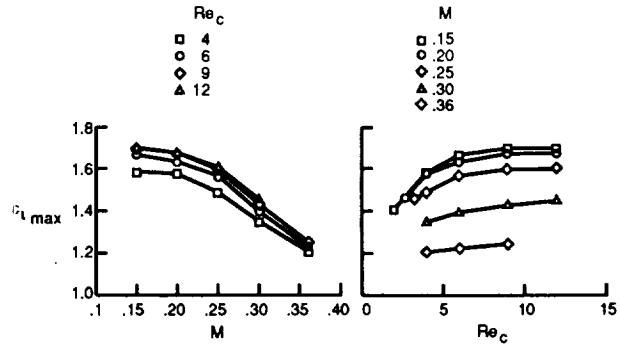

Figure 18. Effects of Reynolds number and Mach number on $c_{l_{max}}$ for a NACA 0012 airfoil.

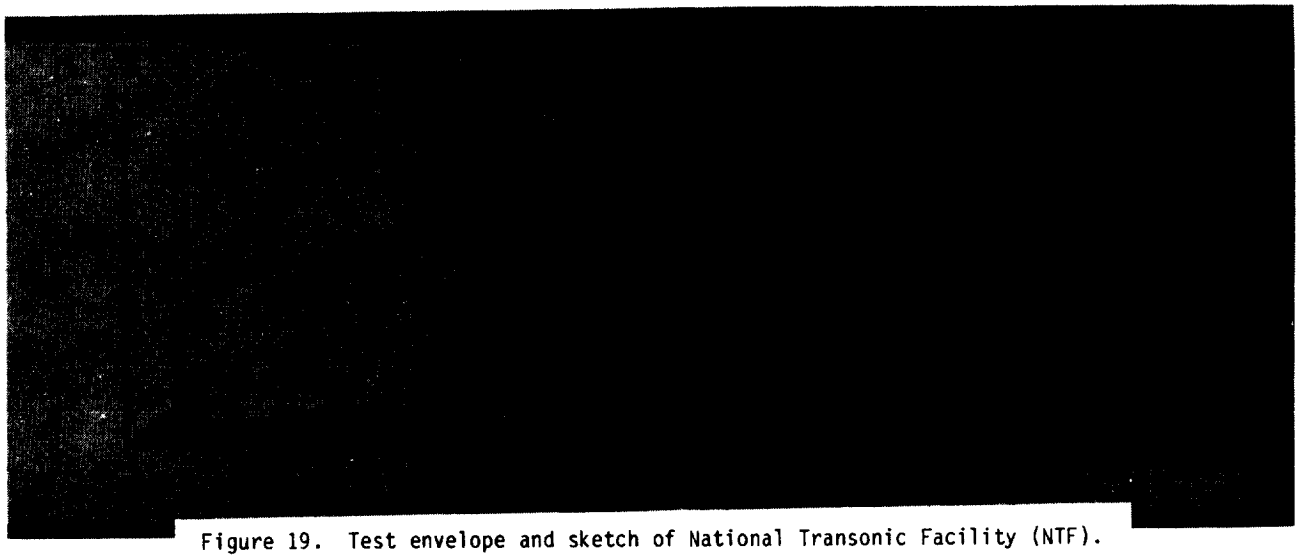

Figure 19. Test envelope and sketch of National Transonic Facility (NTF).

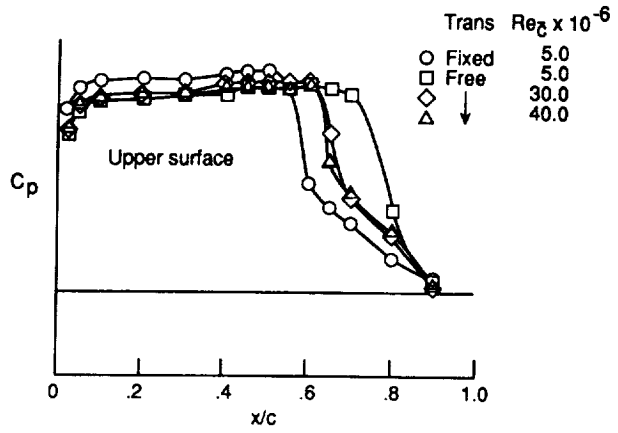

Figure 20. Effect of Reynolds number on C_p distribution for a Lockheed high-wing-transport configuration. M = 0.8; C_N = constant.

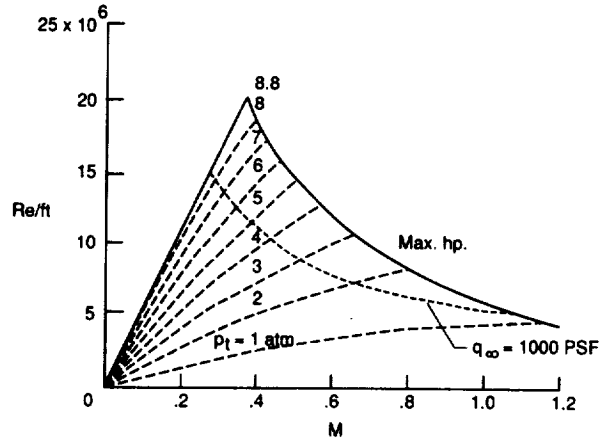

Figure 21. Operating envelope of the NTF in air mode.

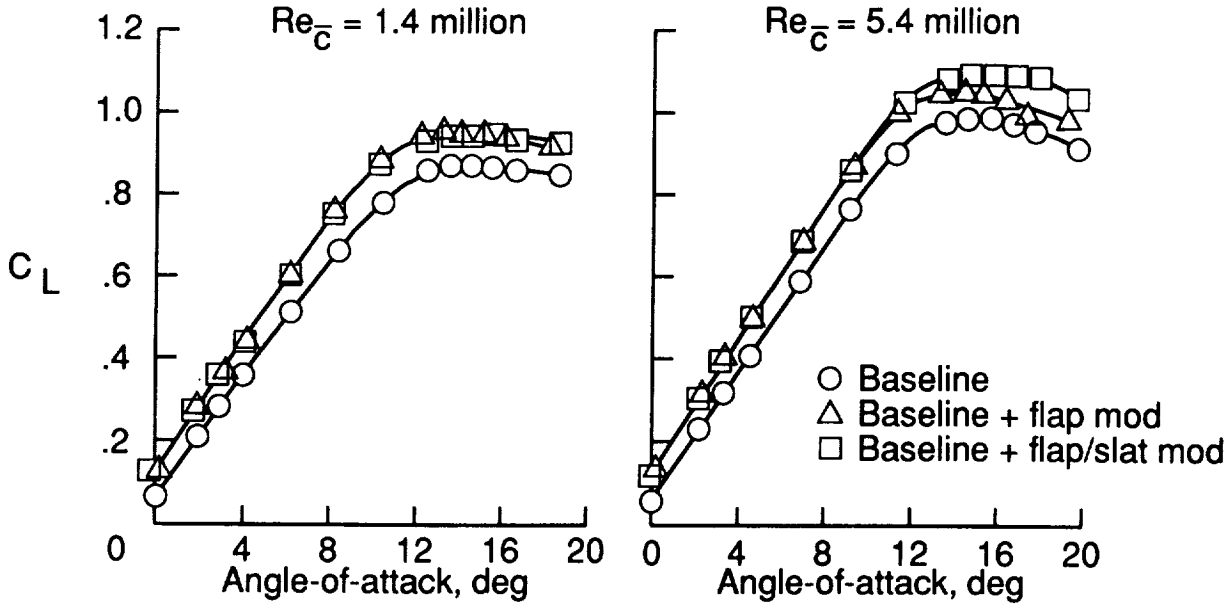

Figure 22.- Effect of flap/slot modifications on low-speed lift characteristics for the EA-6B aircraft at two Reynolds numbers. M = 0.30.

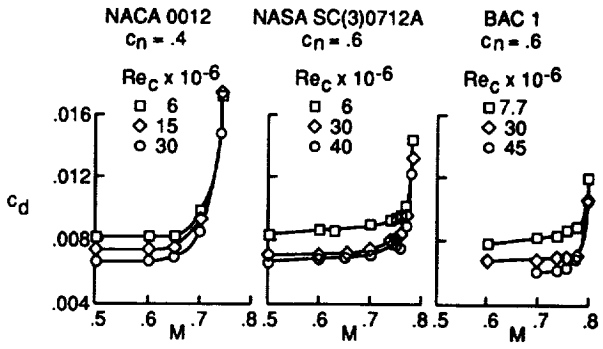

Figure 23. Effects of Reynolds number on drag coefficient for three airfoils tested in the 0.3-m TCT.

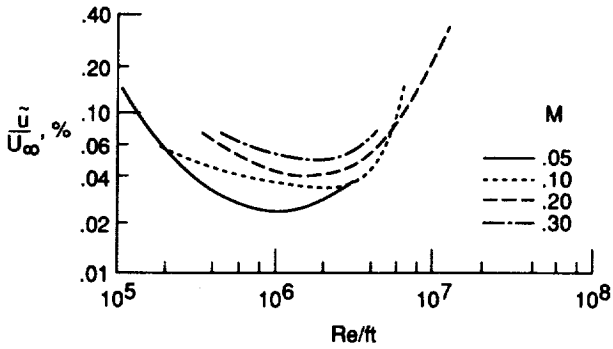

Figure 24. Variation of streamwise velocity fluctuations with unit Reynolds number for a range of Mach numbers in the LTPT.

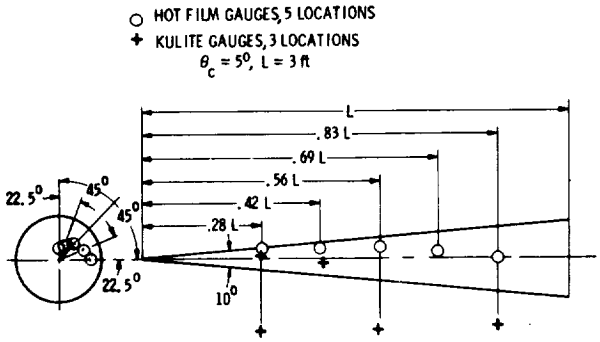

Figure 25. Geometry and instrumentation of "transition" cone.

Figure 26. Photograph of transition cone mounted on nose sting of F-15 aircraft.

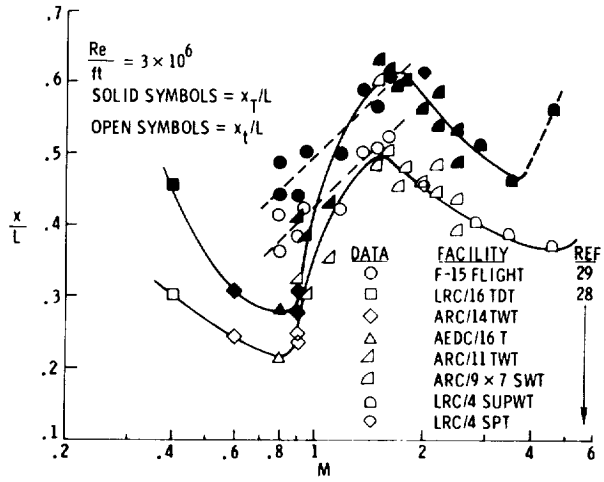

Figure 28. Variation of the onset and end of transition on cone model with Mach number from wind tunnel and flight tests.

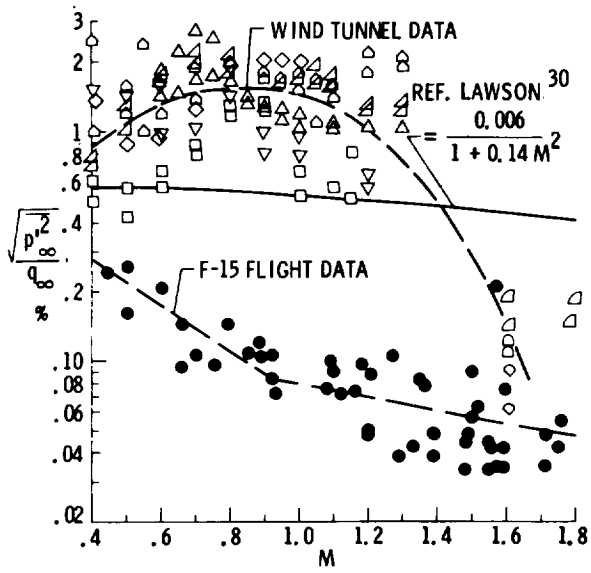

(a) Comparison of wind tunnel and flight data to a Mach number of 1.8.

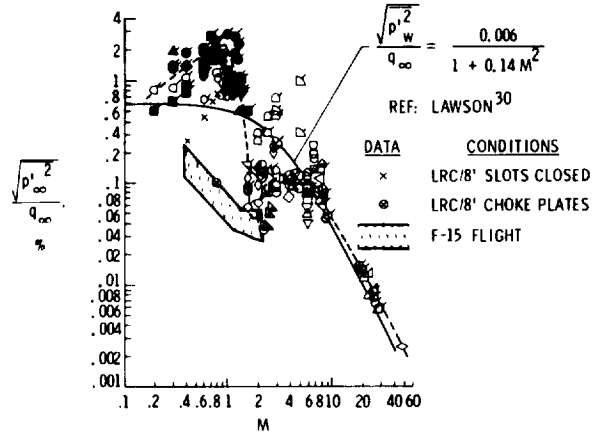

(b) Comparison of wind tunnel and flight data including data from the 8' TPT showing effects of closing slots and using choke plates.

Figure 27. Variation of the normalized unsteady-pressure levels with Mach number obtained from a variety of wind tunnels and F-15 flight tests.

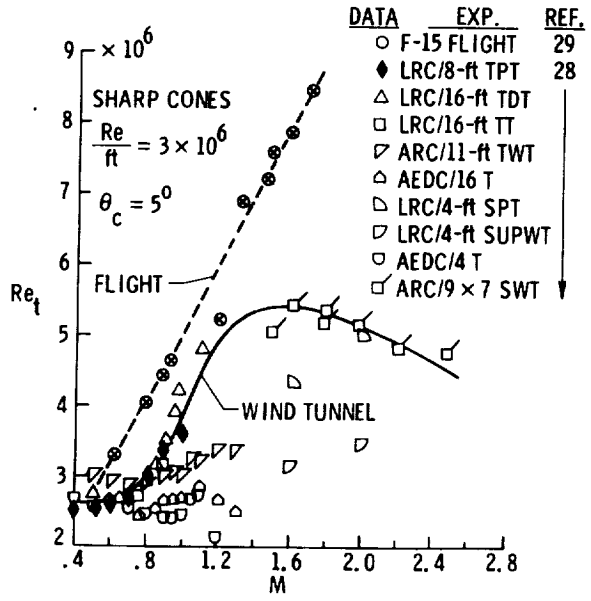

(a) Reynolds number at start of transition vs M.

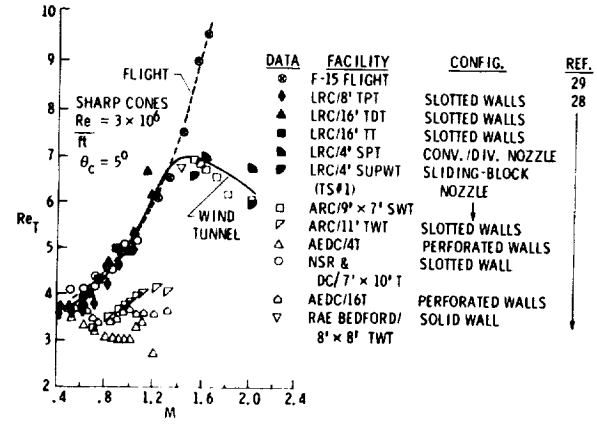

(b) Reynolds number at end of transition vs M.

Figure 29. Comparison of the Reynolds numbers at the start and end of transition from wind tunnel and flight tests for a range of Mach numbers.

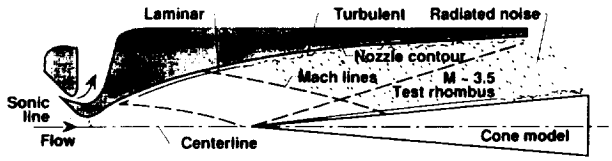

- Blow-down tunnel - high valve and pipe noise
- Settling chamber treatment
- Subsonic boundary-layer removal
- Highly polished walls
- Laminar boundary layer on nozzle walls
- Laminar to turbulent transition on test models same as flight data
- Incident noise can be varied

Figure 30. Features of pilot supersonic low-distrubance tunnel with Mach 3.5 nozzle.

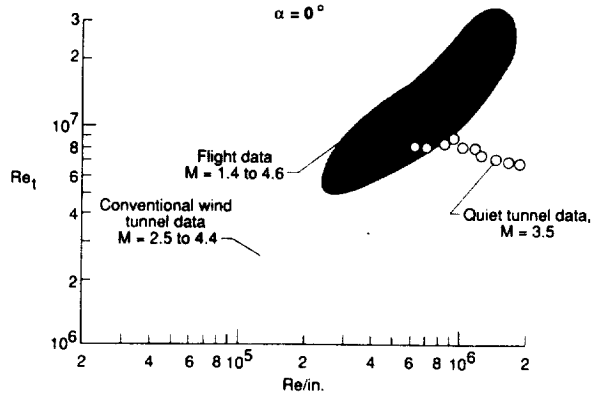

Figure 31. Start-of-transition Reynolds number vs Re/in for transition cone.

- **Strain gage balances**
- **Electronically scanned pressure systems**
- **Hot-film gages**
- **Hot-wire anemometers**
- **Laser velocimeters**
- **Accelerometer and optical systems for angle of attack and yaw**
- **Model deformation**
- **Skin friction gages**
- **Flow angle sensors**
- **Pressure probes**
- **Unsteady pressure sensors (microphones)**

Figure 32. Types of wind tunnel instrumentation.

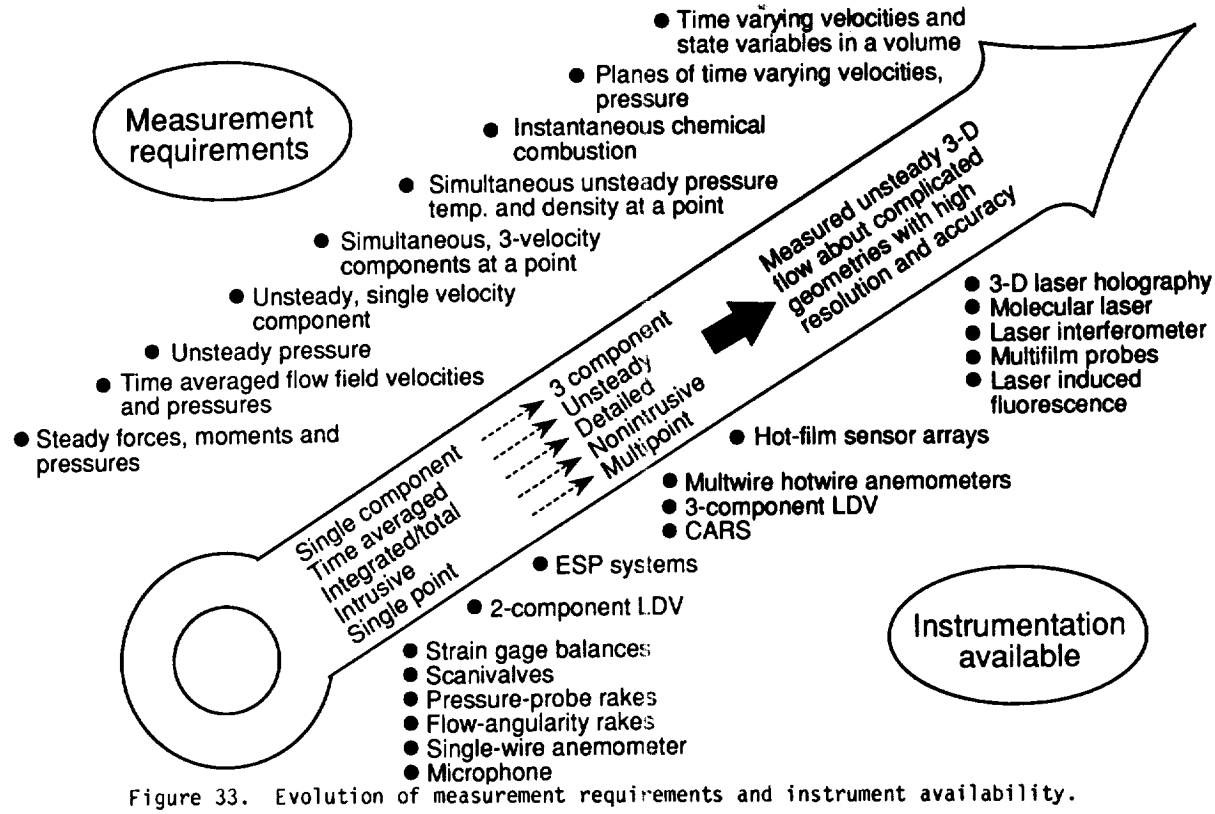

Figure 33. Evolution of measurement requirements and instrument availability.

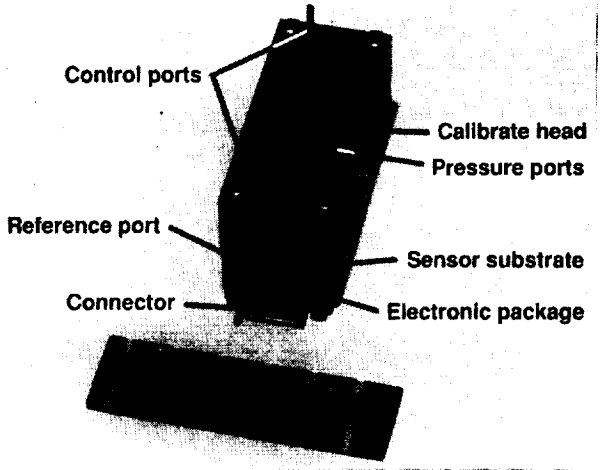

Figure 34. 32-Channel electronically scanned pressure (ESP) sensor module.

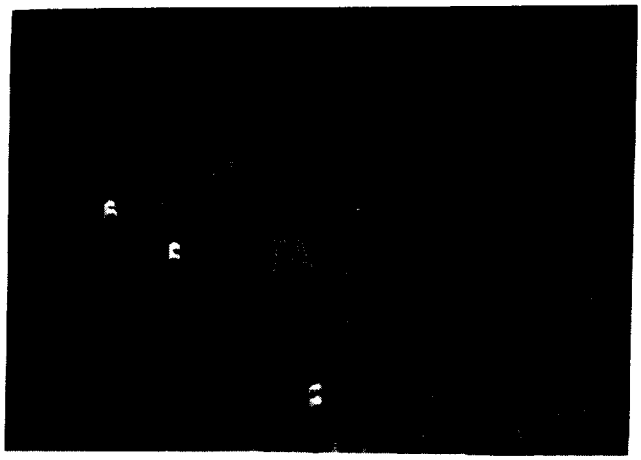

Figure 35. Enlarged photograph of "patch" hot-film gages installed on laminar-flow airfoil model in LTPT.

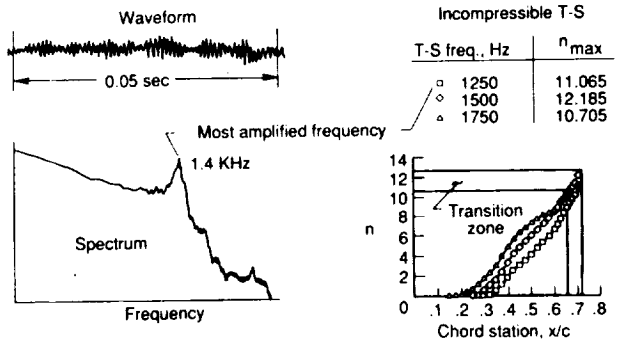

Figure 36. Predicted and measured Tollmien-Schlichting wave characteristics for a laminar-flow-airfoil model.

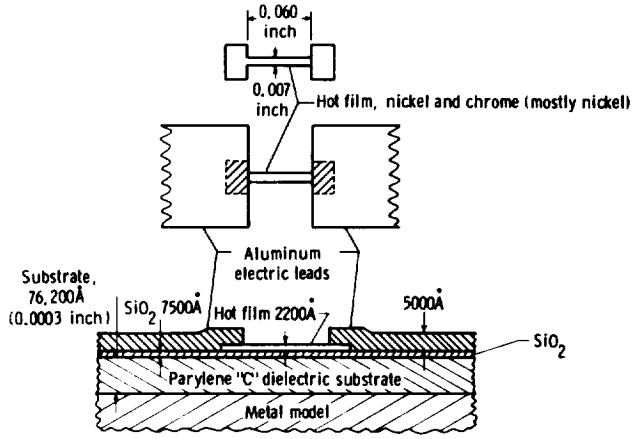

Figure 37. Langley-developed method of hot-film deposition on the surface of a metal model.

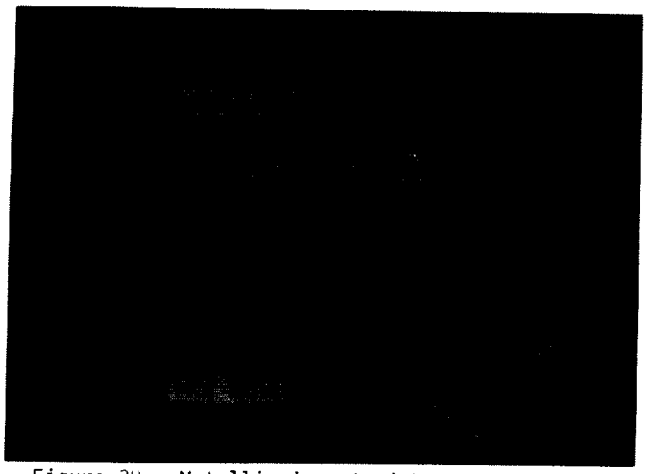

Figure 38. Metallic insert with an array of hot-film sensors used in low speed wind tunnel tests.

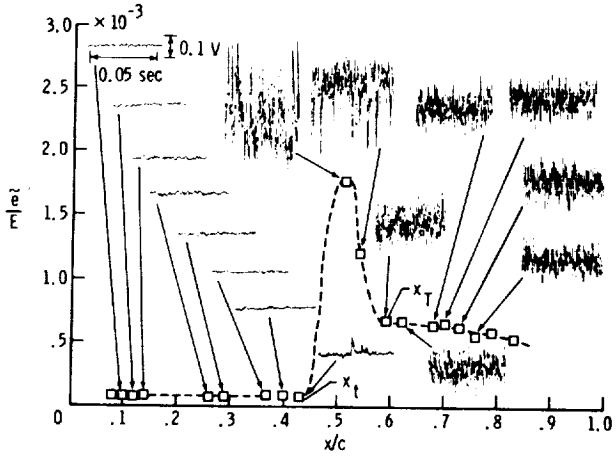

Figure 39. RMS and raw voltage outputs from hot-film sensors at different locations along the chord of the NACA 0012 airfoil. $\alpha = 0°$; $M = 0.122$, $Re_c = 0.86 \times 10^6$.

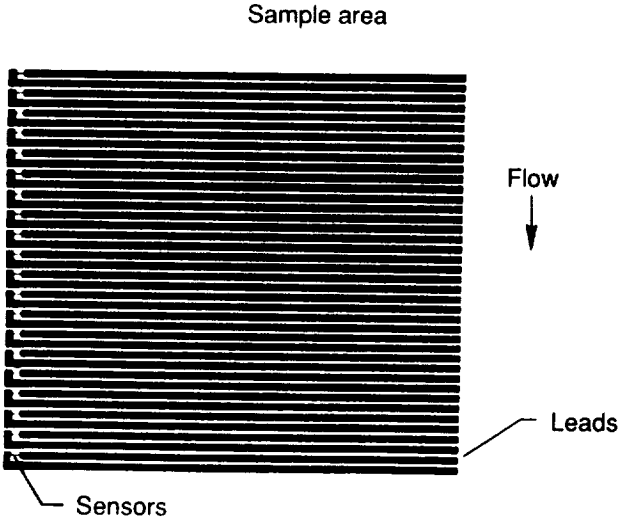

Figure 40. Improved multi-element sensor array with leads that go to the tunnel sidewall.

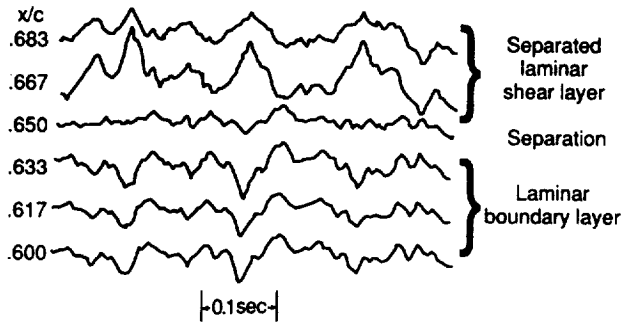

Figure 41. Gage outputs in separation region filtered to 10 Hz.

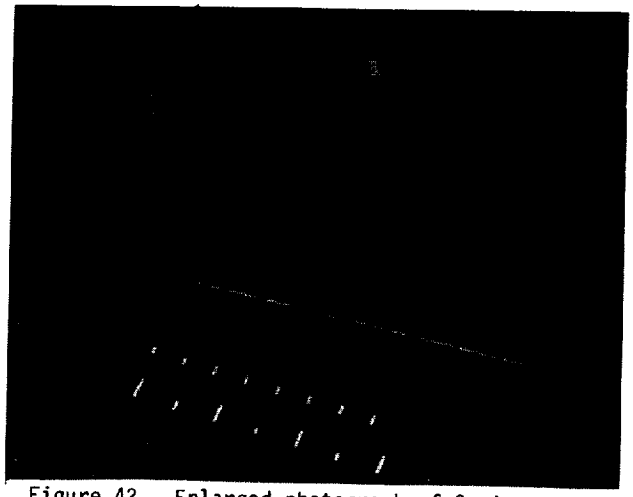

Figure 42. Enlarged photograph of 3-wire probe and probe head.

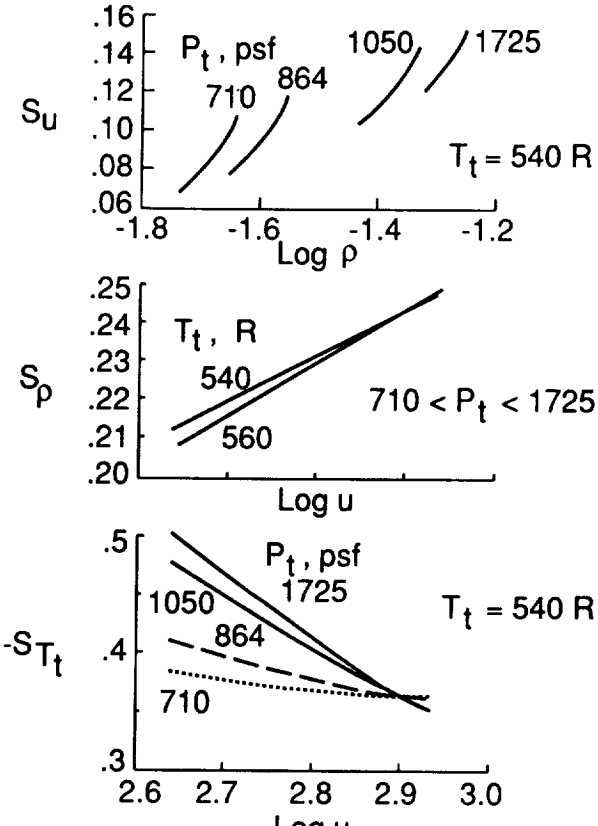

Figure 43. Sample 3-wire hot-wire-probe sensitivity coefficients for velocity, density, and total temperature.

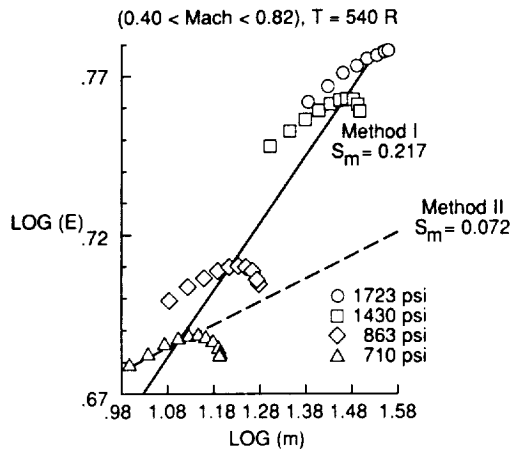

Figure 44. Two methods of obtaining the mass flux sensitivity of a hot wire when single wire techniques are used.

Figure 47. Photographs of an orthogonal 3-component LDV system assembled in the laboratory for checkout.

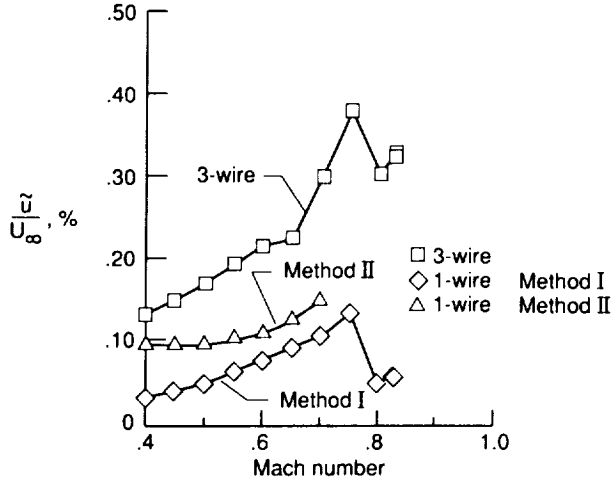

Figure 45. Comparison of the longitudinal fluctuating velocity as a function of Mach number determined by two single-wire methods and with a 3-wire technqiue. p_t = 710 psi.

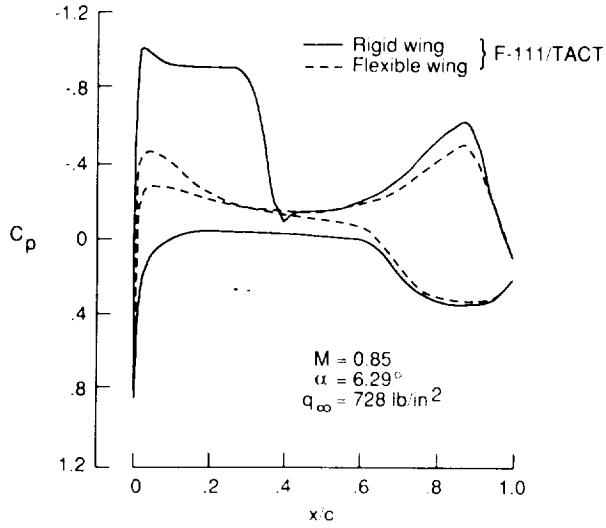

Figure 48. Calculated pressure distributions at 2y/B = 0.92 for a rigid and flexible F-111/TACT wing. M = 0.85, α = 6.29°, q_∞ = 728 lb/in^2.

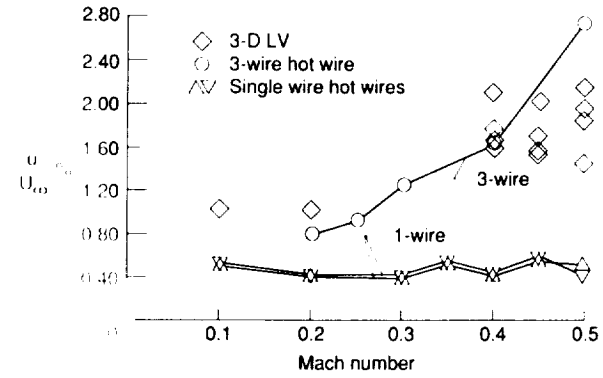

Figure 46. Comparison of the fluctuating longitudinal velocity as determined by single-wire, 3-wire and LDV measurements for a range of subsonic Mach numbers.

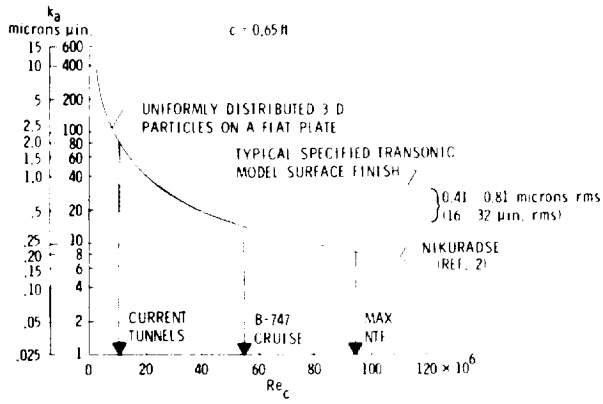

Figure 49. Admissible roughness (k_a) for typical NTF-sized models.

Figure 50. Enlarged photograph of a surface which has been "measured" by a stylus profilometer.

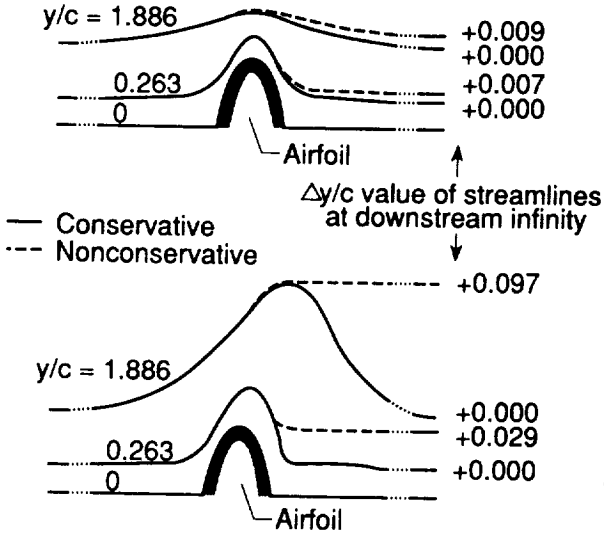

Figure 52. Computed streamline deflections for nonlifting transonic flow past 10%-thick parabolic arc airfoil. Upper figure is for M = 0.84 and lower figure is for M = 0.95.

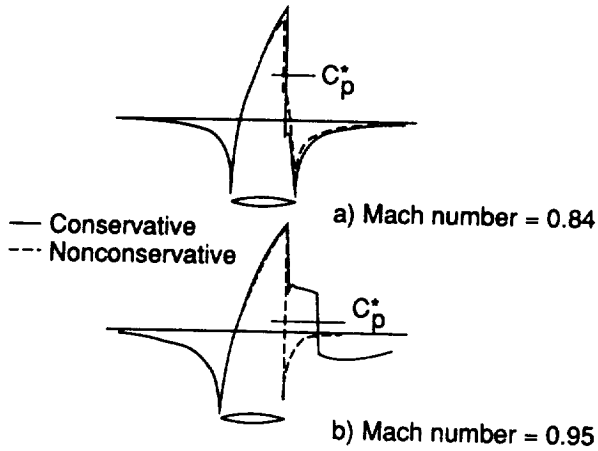

Figure 51. Computed pressure coefficients for nonlifting transonic flow past 10%-thick parabolic arc airfoil.

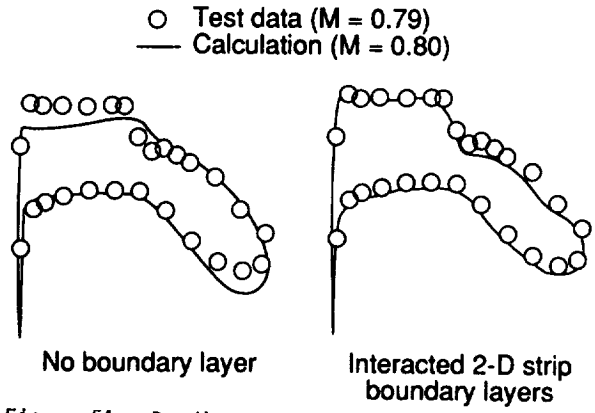

Figure 54. Predicted pressure distributions for a supercritical wing at 45% of the wing span with and without an interacted boundary layer.

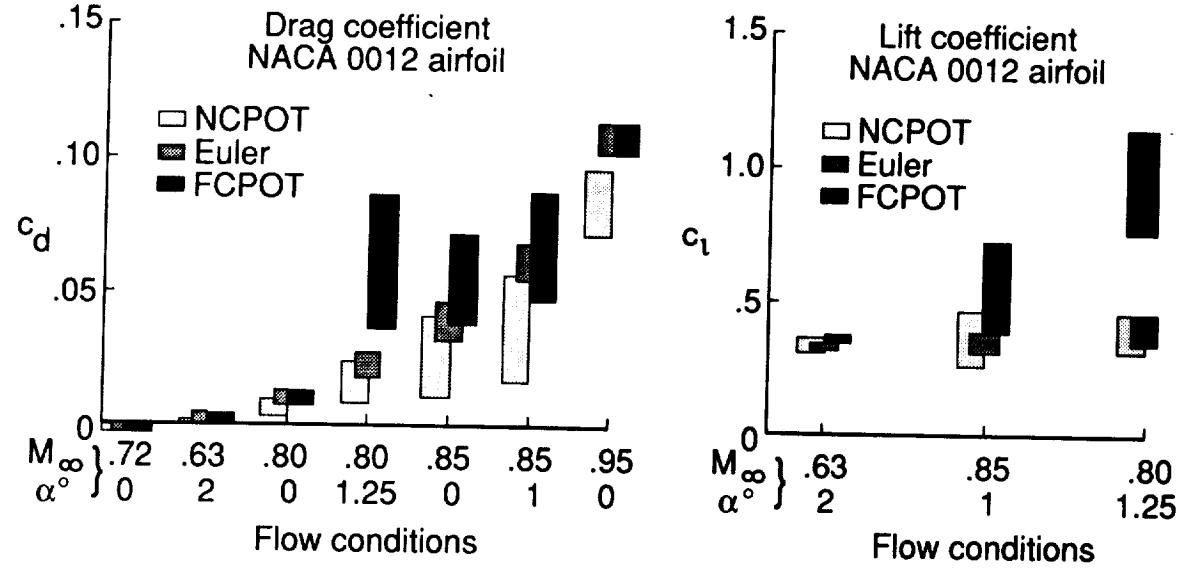

Figure 53. Lift and drag coefficient results from a number of airfoil codes using Euler-equation and nonconservative- and conservative-potential methods.

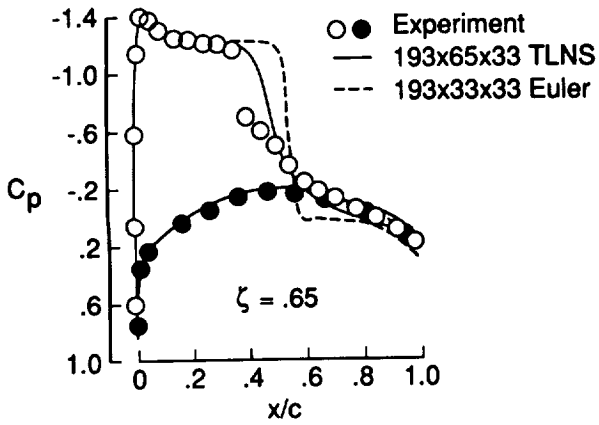

Figure 55. Comparison of viscous (TLNS) and inviscid (Euler) pressure distributions for a shock-separated flow on the ONERA M6 wing. (ζ = 0.65; M = 0.84; α = 6.06 deg.)

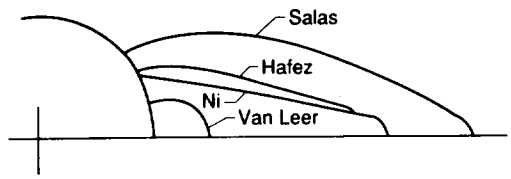

Figure 57. Comparison of recirculation bubble shapes at M = 0.5.

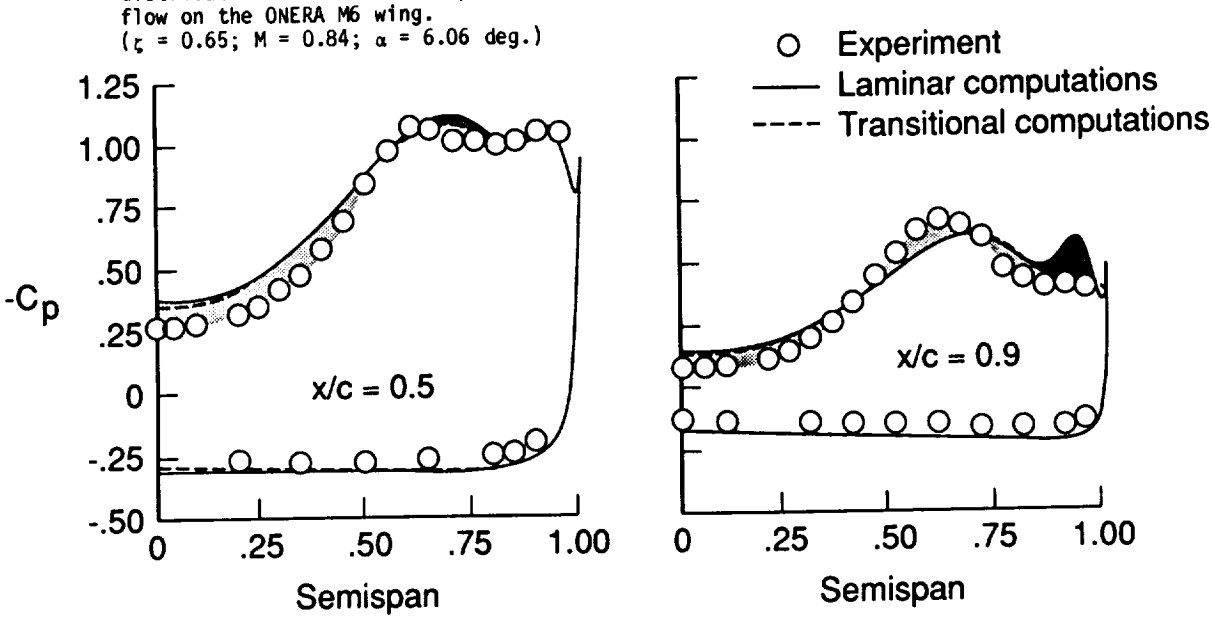

Figure 56. Comparison of experimental spanwise pressure distributions for a sharp-edged delta (AR = 1) wing with calculated laminar and transitional boundary layers. (α = 20.5 deg.; Re_{c_R} = 0.9 x 10^6.)

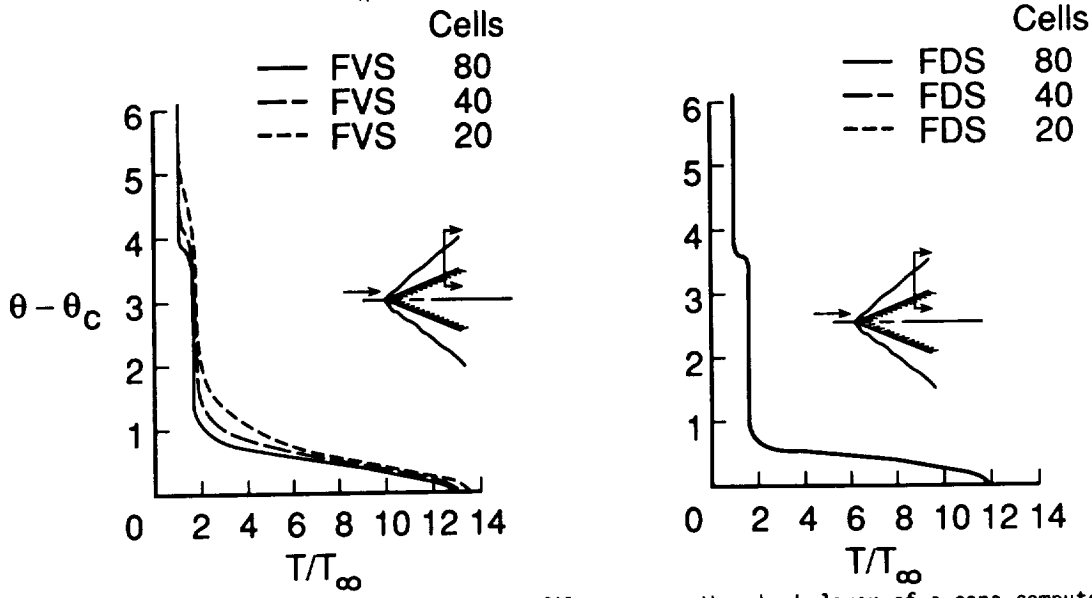

Figure 58. Comparison of the temperature profiles across the shock layer of a cone computed using a TLNS code employing a range of grid cell sizes and FVS or FDS schemes. (Adiabatic wall)

- NACA 0015 airfoil
- M = 0.2
- Re = 45 000, laminar flow computation
- Pitch up about 1/4c from $\alpha = 0°$ to 60°
  - k = 0.2 — ≈ 250°/sec for 10ft chord at STP
  - k = 0.6 — ≈ 750°/sec for 10ft chord at STP

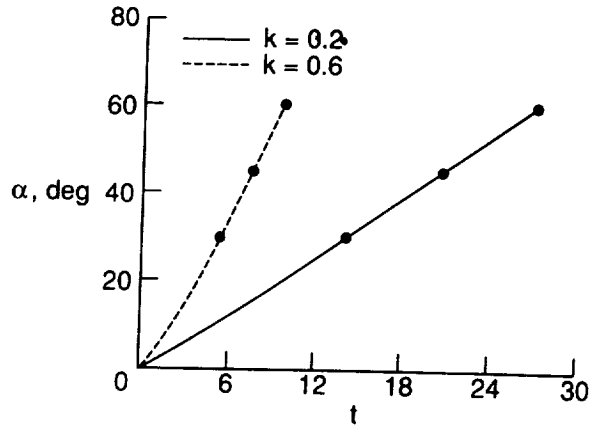

Figure 59. Description of the features of an unsteady NACA 0015 airfoil calculation.

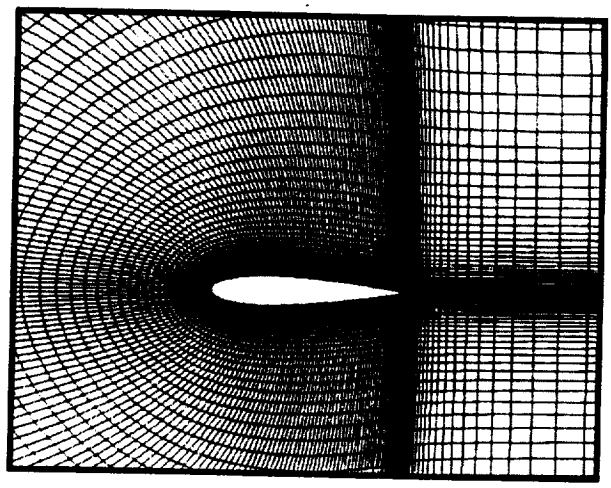

Figure 60. Grid system used in unsteady NACA 0015 airfoil calculation. (257 x 97 c-mesh)

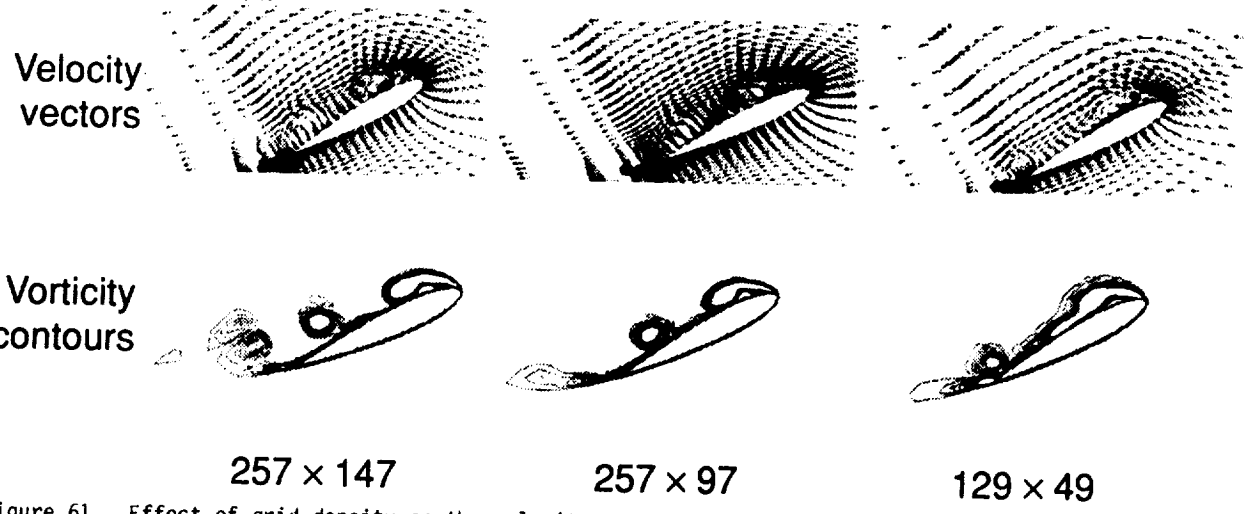

Figure 61. Effect of grid density on the velocity vectors and vorticity contours for the unsteady NACA 0015 calculation employing the FDS scheme. k = 0.2; α = 30°.

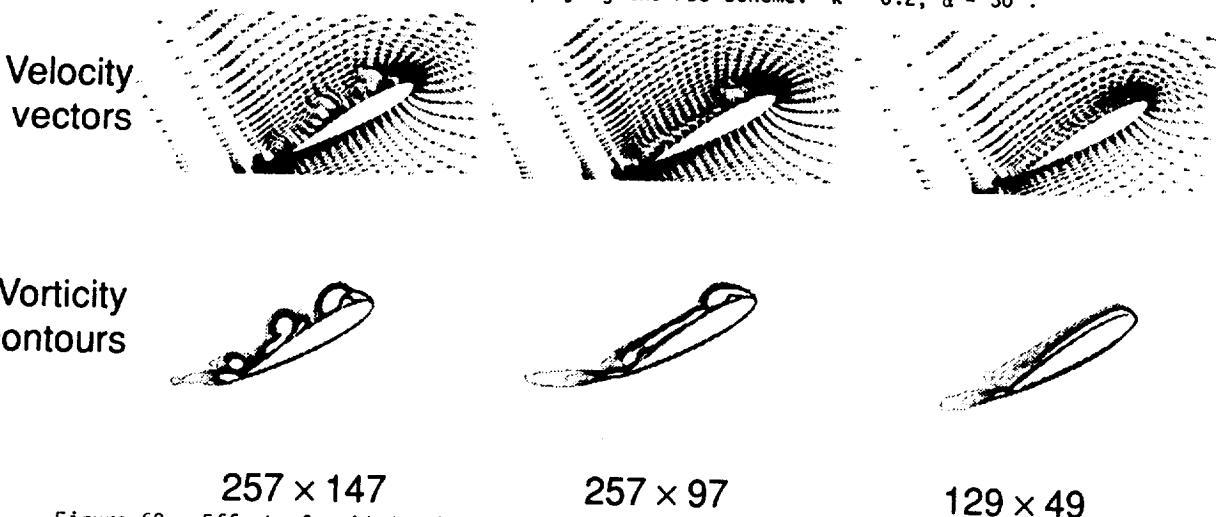

Figure 62. Effect of grid density on the velocity vectors and vorticity contours for the unsteady NACA 0015 calculation employing the FVS scheme. k = 0.2; α = 30°.

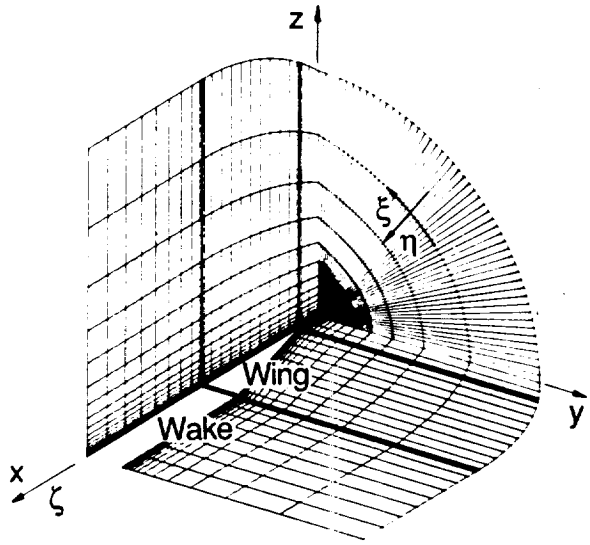

Figure 63. Partial view of the three-dimensional grid used in delta wing calculations.

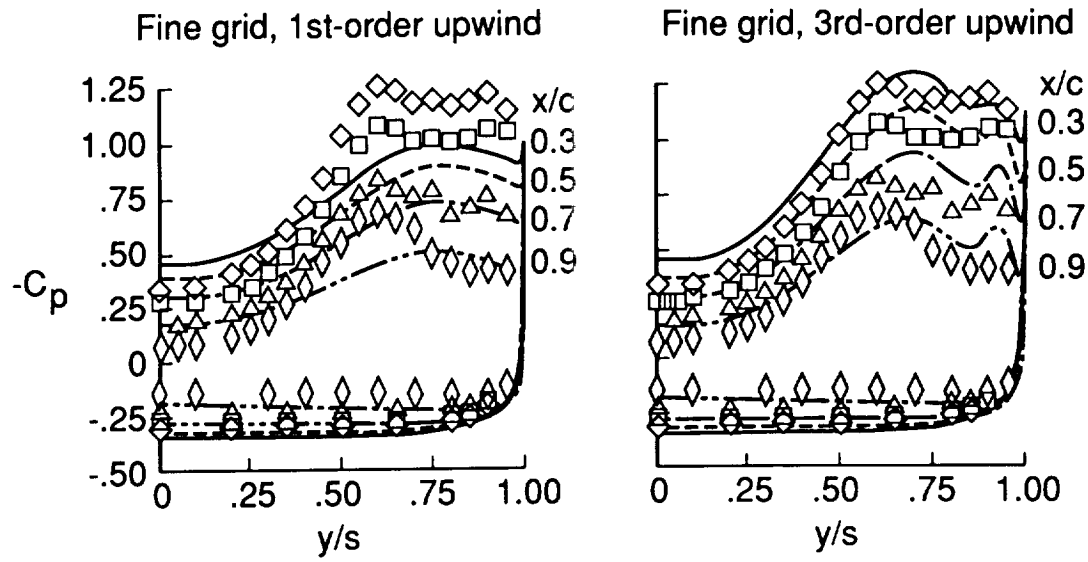

Figure 64. Theoretical and experimental spanwise distributions of pressure coefficient for a delta wing using first-order and third-order upwind differences. (AR = 1.0; α = 20.5 deg.; Re_{c_R} = 0.9 x 10^6.)

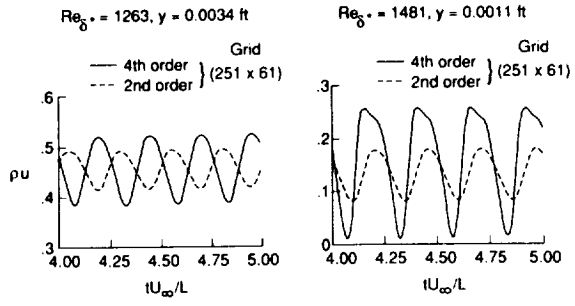

Figure 65. ρu vs time using second- and fourth-order schemes for two downstream locations.

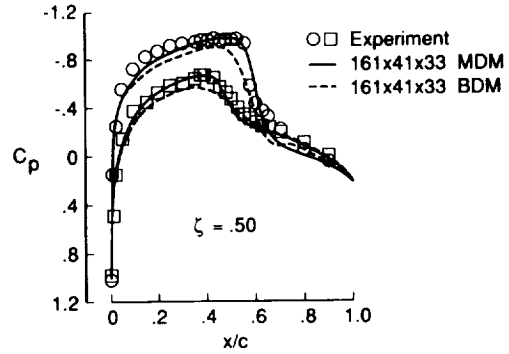

Figure 66. Wing pressure-distribution comparisons for 161 x 41 x 33 grid with basic (BDM) and modified (MDM) dissiptation models. NACA 0012 untapered semispan wing. 20° sweep, M = 0.826; $Re_{\bar{c}}$ = 8 x 10^6.

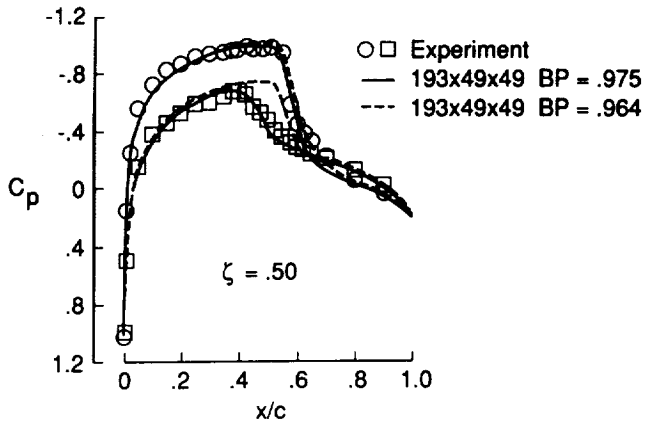

Figure 67. Wing pressure distribution comparison for free-air and in-tunnel solutions.

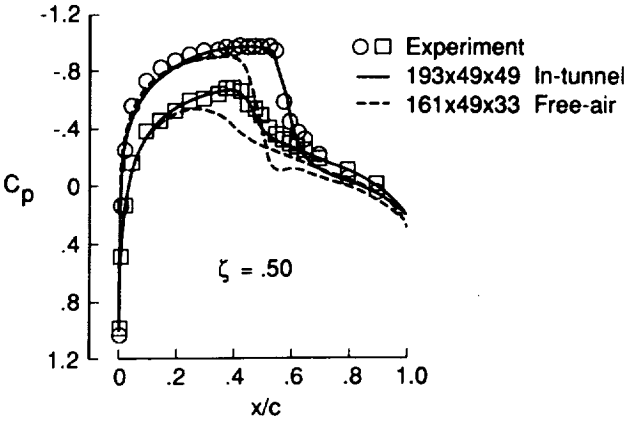

Figure 68. Wing pressure distribution comparisons for low and high values of back pressure ratio at the 50% span location.

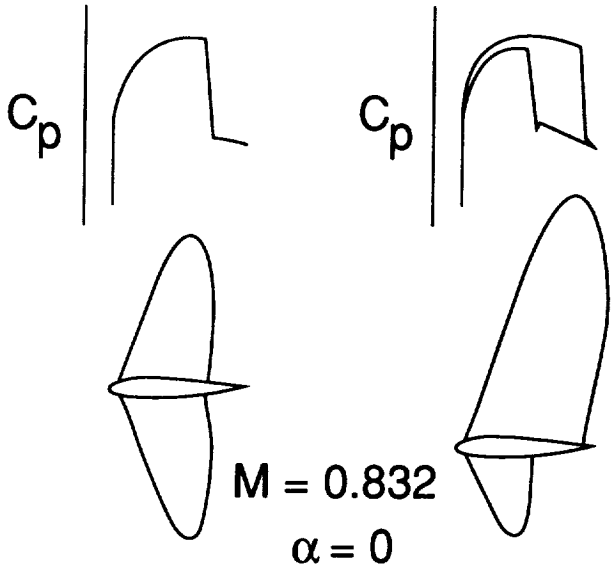

Figure 69.- Multiple solutions for an 11.8% thick symmetric Joukowski airfoil at a Mach number of 0.832 and zero angle of attack.

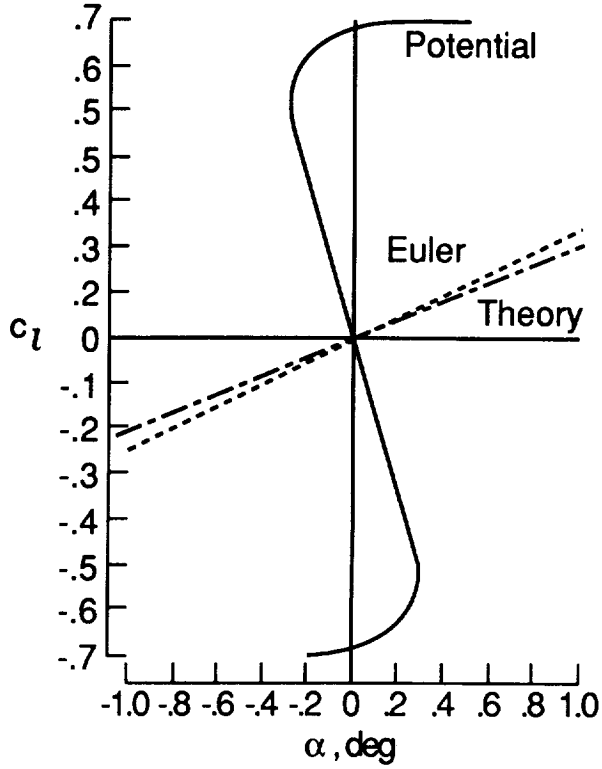

Figure 70. Lift coefficient as a function of angle of attack computed for a NACA 0012 airfoil at M = 0.83 using FL036-2, TAIR and an Euler code. The prediction of Prandtl-Glauert theory is labeled "Theory".

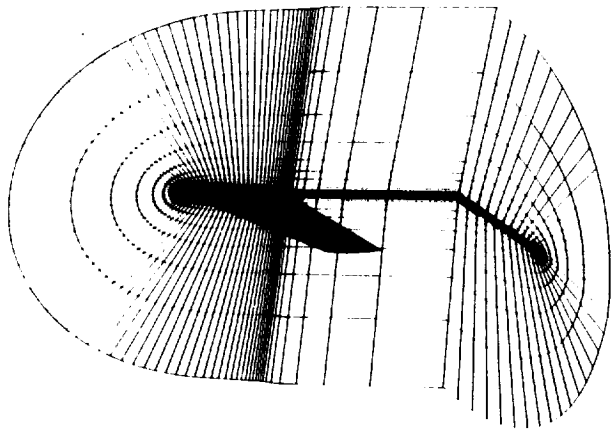

Figure 71. Partial view of C-O grid for ONERA M6 wing calculation.

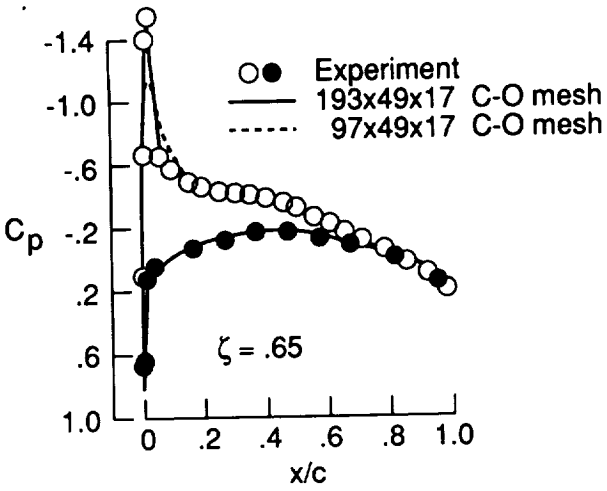

Figure 72. Effect of streamwise grid refinement on chordwise pressure distribution for the ONERA M6 wing. (ζ = 0.65; M = 0.699; α = 3.06 deg)

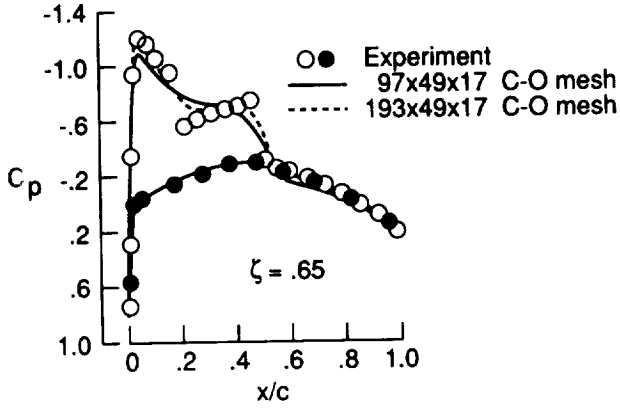

Figure 73. Effect of streamwise grid refinement on the chordwise pressure distribution for the ONERA M6 wing. (ζ = 0.65; M = 0.84; α = 3.06 deg)

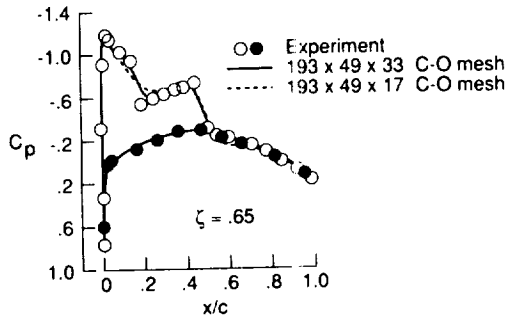

Figure 74. Effect of spanwise grid refinement on the chordwise pressure distribution for the ONERA M6 wing. (ζ = 0.65; M = 0.84; α = 3.06 deg)

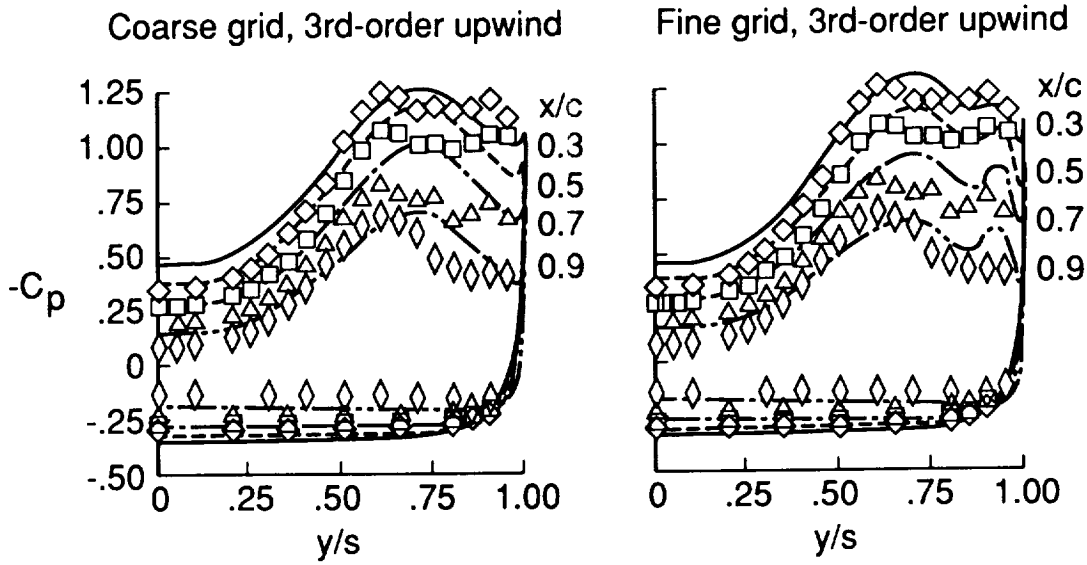

Figure 75. Comparison of theoretical spanwise pressure distributions on a delta wing using fine and coarse grids with experiment. (AR = 1; α = 20.5 deg; $Rec_R = 0.9 \times 10^6$)

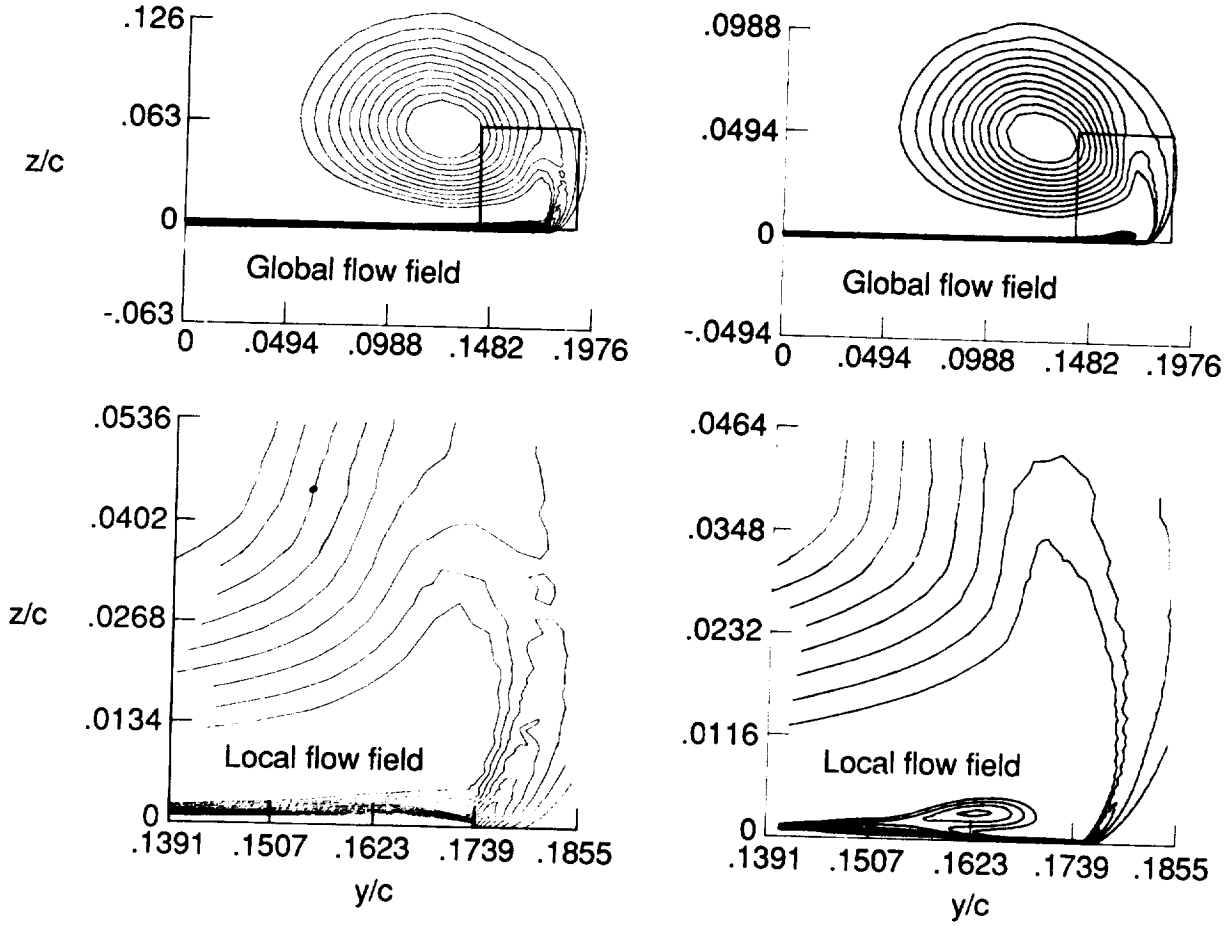

Figure 76. Coarse and fine grid (left and right hand plots, respectively) calculations of total-pressure-coefficient contours in the crossplane at x/c = 0.7. (AR = 1, α = 20.5 deg, $Rec_R = 0.9 \times 10^6$)

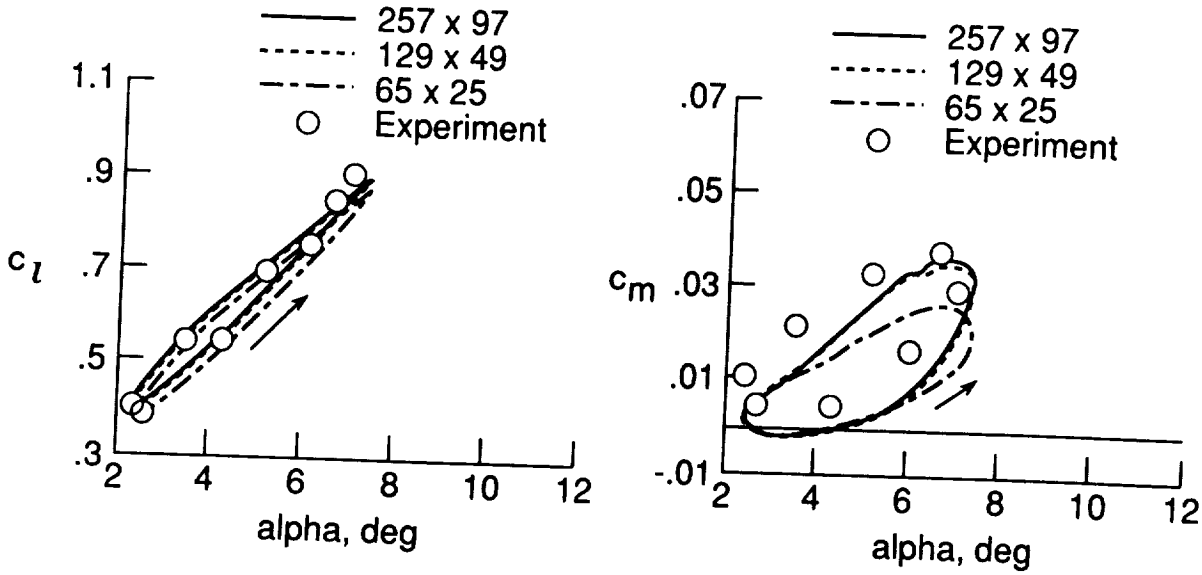

Figure 77. Effect of grid density on c_l and c_m with angle of attack for an NACA 0012 airfoil undergoing a sinusoidal variation in angle of attack. (M = 0.6, α_0 = 4.86 deg, α_1 = 2.44 deg, $Re_c = 4.8 \times 10^6$, k = 0.162)

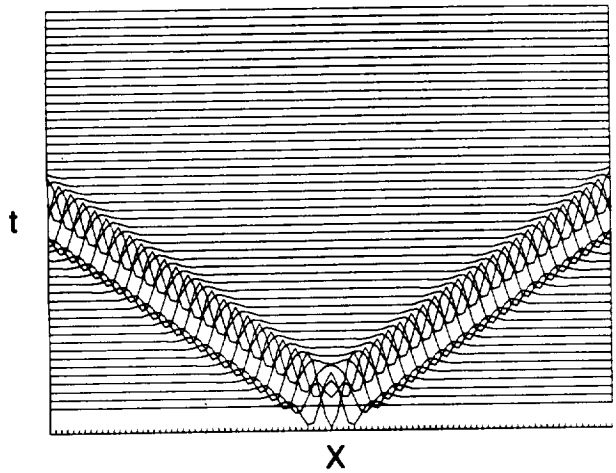

Figure 78. Exact solution of wave equation for wave pocket propagation in x-t space.

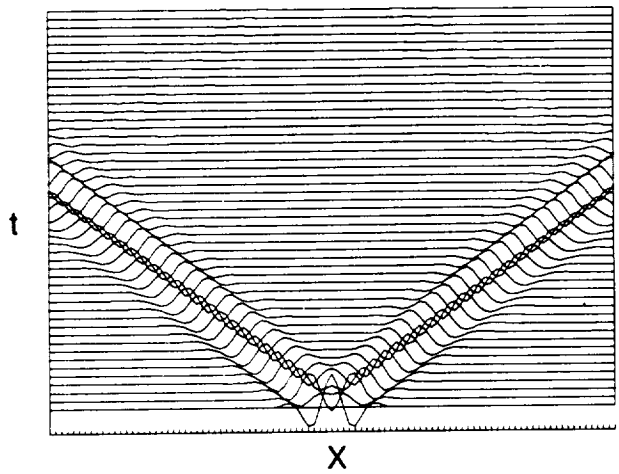

Figure 79. Finite difference solution on uniform fine grid of wave equation for wave pocket propagation in x-t space.

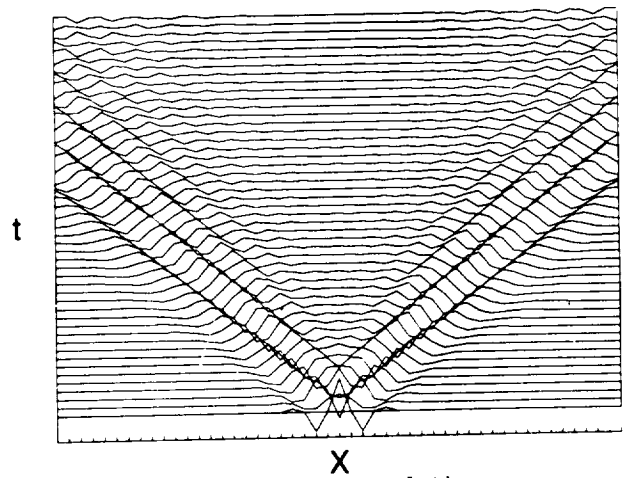

Figure 80. Finite difference solution on stretched grid of wave equation for wave pocket propagation in x-t space.

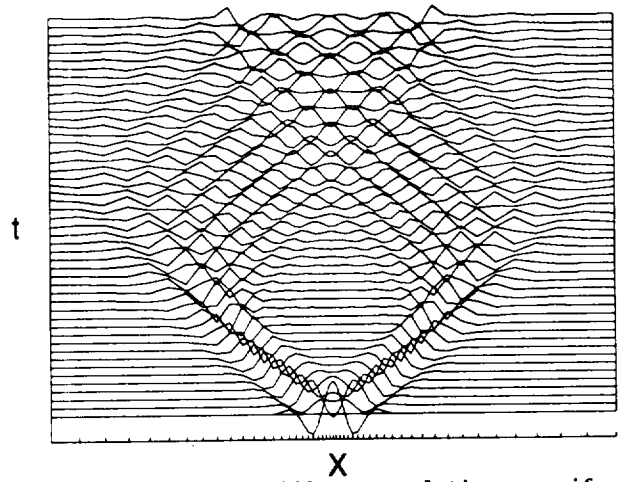

Figure 81. Finite difference solution on uniform coarse grid of wave equation for wave pocket propagation in x-t space.

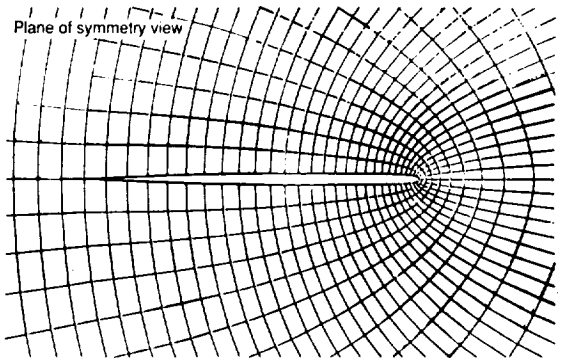

Figure 82. Parabolic C-H mesh generated by conformal transformation technique. (96 x 16 x 16 grid)

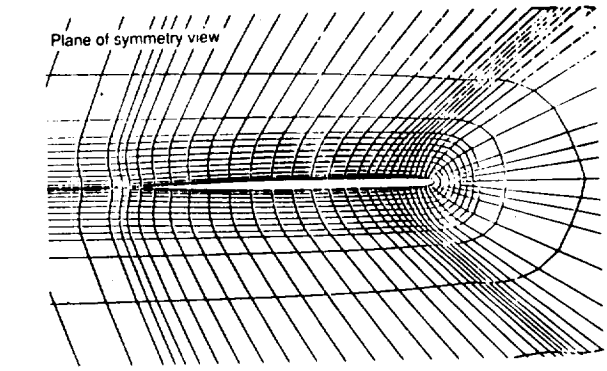

Figure 83. Algebraic C-H grid generated by parametric interpolation procedure. (96 x 16 x 16 grid)

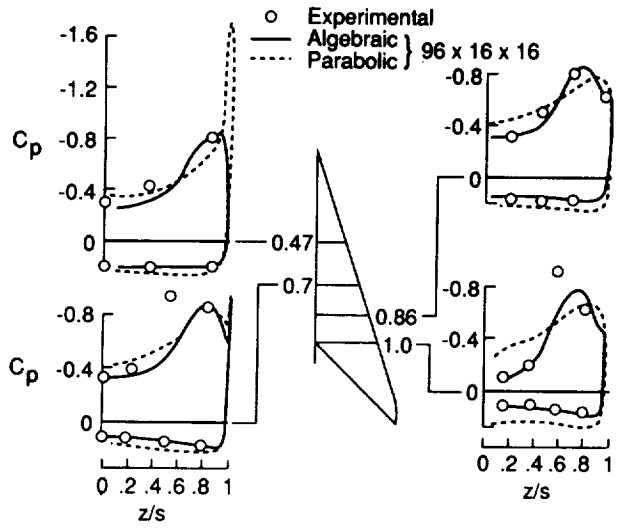

Figure 84. Comparison of computational and experimental cross-plane pressure distributions for an arrow wing. M = 0.85, α = 15.8 deg.

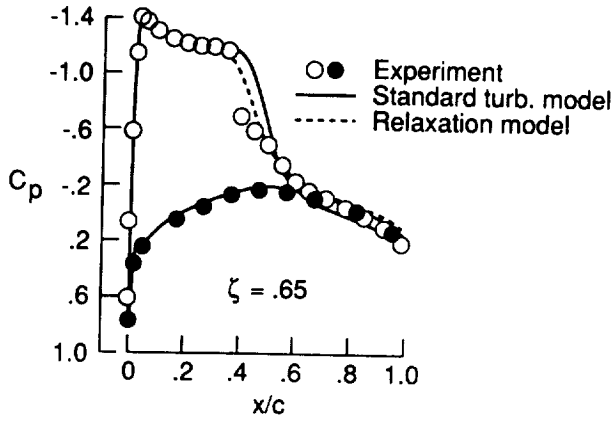

Figure 85. Effect of relaxation turbulence model on computed pressure distributions on ONERA M6 wing at α = 6.06 deg. and M = 0.84.

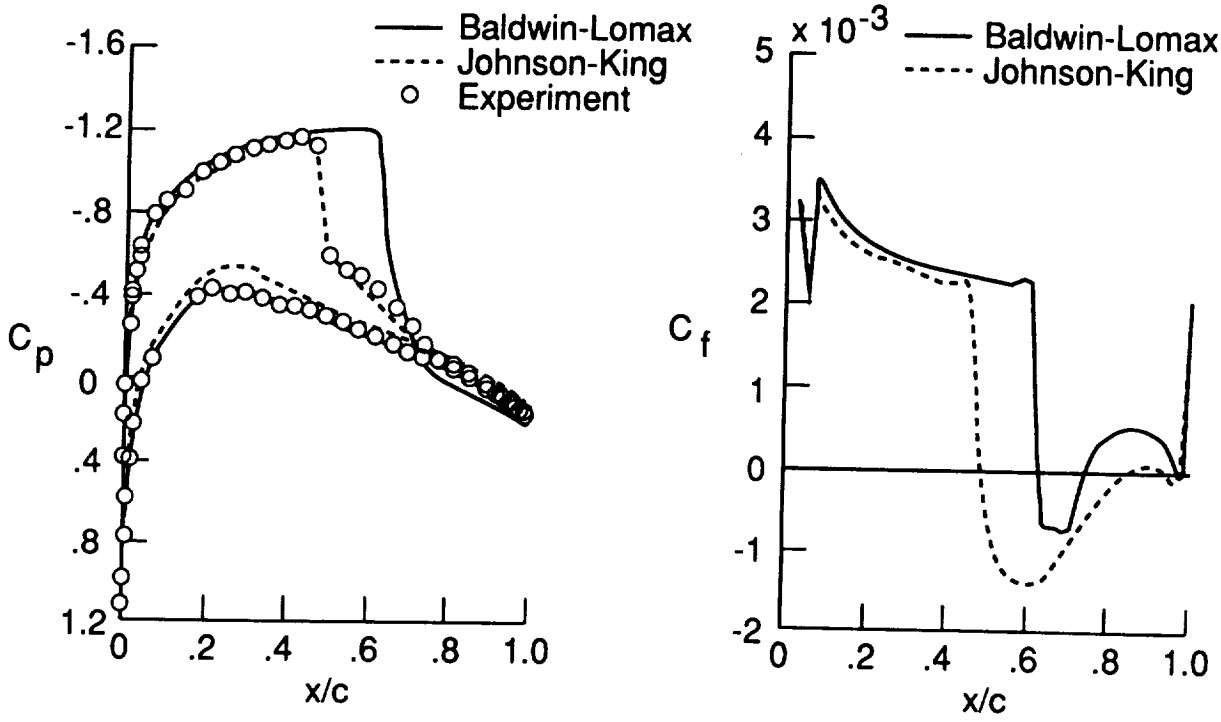

Figure 86. Effect of two different turbulence models on the chordwise pressure- and skin-friction-coefficient distributions on a NACA 0012 airfoil. (M = 0.799, α = 2.26 deg, $Re_c = 9 \times 10^6$)

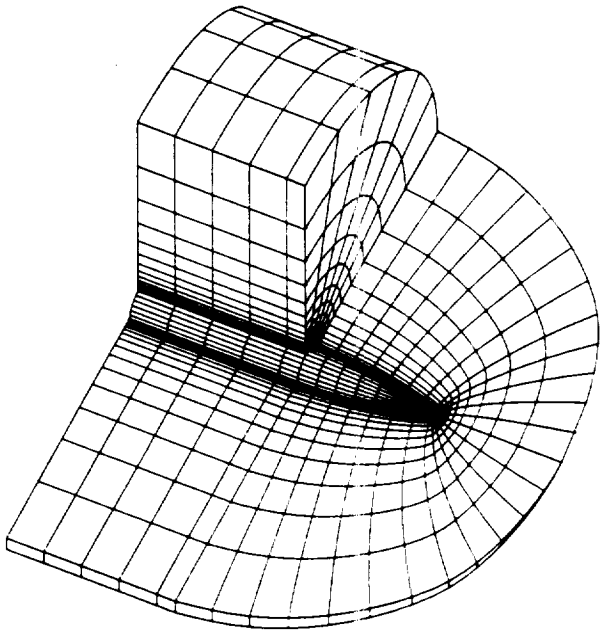

Figure 87. C-O grid used in TLNS calculation of flow about an ogive cylinder.

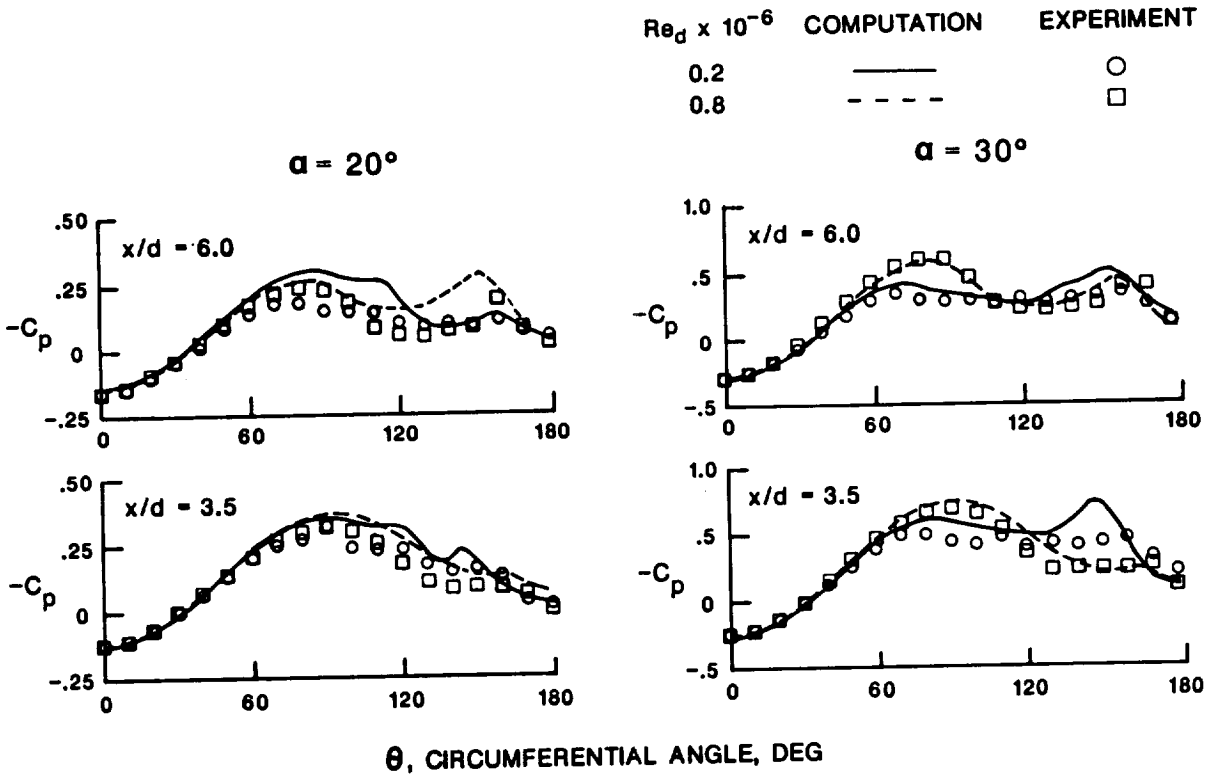

Figure 88. Circumferential surface pressure distributions for a 3.5 caliber tangent ogive at two longitudinal locations, two Reynolds number, and two angles of attack.

NASA National Aeronautics and Space Administration

Report Documentation Page

1. Report No.	2. Government Accession No.	3. Recipient's Catalog No.
NASA TM-100657		

4. Title and Subtitle

The Pros and Cons of Code Validation

5. Report Date

July 1988

6. Performing Organization Code

7. Author(s)

Percy J. Bobbitt

8. Performing Organization Report No.

10. Work Unit No.

505-61-01-01

9. Performing Organization Name and Address

Langley Research Center
Hampton, Virginia 23665-5225

11. Contract or Grant No.

12. Sponsoring Agency Name and Address

National Aeronautics and Space Administration
Washington, DC 20546-0001

13. Type of Report and Period Covered

Technical Memorandum

14. Sponsoring Agency Code

15. Supplementary Notes

Invited Paper Presented at the AIAA 6th Applied Aerodynamic Conference, June 6-8, 1988, Williamsburg, Virginia, AIAA Paper 88-2535.

16. Abstract

The correlation of theory with experimental data has been going on as long as we have had theoretical methods and experimental facilities. Up until the 1970's the primary objective of this activity in the aeronautical sciences was to determine if the theoretical methods were valid. Approximations and assumptions made to reduce the governing equations and boundary conditions to a solvable form insured that the experimental results would be more accurate. Today, however, with our ability to solve the most complicated, nonlinear fluid-flow equations with high precision, the accuracy of computed results may, in some situations, exceed that obtained in the wind tunnel. Consequently, to determine which of the two results are the most reliable one must assess in detail the cumulative result of the various error sources in each. The purpose of the present paper is to examine a number of these error sources and quantify them with the aid of specific calculations or experimental data. In many cases suggestions and examples will be given to indicate how the error source can be minimized.

17. Key Words (Suggested by Author(s))	18. Distribution Statement
Code Validation Experimental Errors Computational Errors Test Techniques Instrumentation Errors	Unclassified - Unlimited Subject Category 02

19. Security Classif. (of this report)	20. Security Classif. (of this page)	21. No. of pages	22. Price
Unclassified	Unclassified	48	A03